Electronic and Atomic Structure, and Magnetism of Transition-Metal Clusters

J. A. Alonso

Departamento de Física Teórica, Universidad de Valladolid, 47011 Valladolid, Spain

Received March 29, 1999

Contents

Julio A. Alonso has been Professor of Physics since 1988 at the University of Valladolid in Spain. He was born in Valladolid in 1948. He received his Lic. degree in 1971 and Ph.D. degree in 1975 from the University of Valladolid. He was a postdoctoral fellow and research associate from 1975 to 1980 in the Department of Materials Science and the Laboratory for Research of the Structure of Matter, University of Pennsylvania, Philadelphia, working with Professor L. A. Girifalco on the theory of the chemical binding in metallic alloys and also on nonlocal approximations to exchange and correlation in density functional theory. From 1980 to 1988 he was Associate Professor at the University of Valladolid. He has been a visiting scientist at Imperial College (London), Max-Planck Institut (Stuttgart), University of Osnabruck, University of Oxford, International Center for Theoretical Physics (Trieste), University of East Anglia, and Queen's University (Kingston). His research interests include density functional theory, crystalline and amorphous metallic materials, atomic clusters, and fullerenes.

I. Introduction

The free atoms of the transition metals have an incomplete d shell in the ground state or in excited states of small energy. The d electrons are responsible for the most interesting properties of these elements as free atoms or in the metallic bulk phase. In the same way, most properties of clusters of transition elements reflect the rather localized behavior of the d electrons, in contrast with clusters or solids of simple sp metals whose properties are dominated by the delocalized behavior of the external sp electrons.[1,2] This delocalized character leads to one of the main characteristics of sp clusters: the formation of electronic shells and the occurrence of shell-closing effects[3] similar to those in free atoms or in nuclei. Those electronic shell effects are also present in clusters of coinage metals (Cu, Ag, Au) since the d electrons form full d^{10} shells in these atoms. For this reason, noble-metal clusters are first reviewed in section II. Clusters of typical transition elements do not have shell effects because, as said above, the unfilled d shells dominate their properties. Still, transition-metal clusters have a wealth of other properties that make their study extremely interesting.

Here, the electronic properties of transition-metal clusters will be reviewed by presenting the results of experimental measurements and discussing those results in light of theoretical calculations in sections

10.1021/cr980391o CCC: $35.00
Published on Web 01/20/2000

III, IV, V, and VI. An usual output of the calculations is the geometrical structure of the cluster, which is a crucial ingredient in any attempt of interpreting the experimental measurements of the electronic properties. For small clusters, ab initio methods can be used to determine their structure and reviews have been published for the limiting case of transition-metal dimers.[4,5] Here we are mainly interested in clusters larger than the dimers. In this case, there are often several low-lying structural isomers with energies only slightly above the ground state. However, the close interplay between atomic and electronic structure means that the ordering and the nature of the electronic energy levels, especially those near the highest-occupied orbital, are different for different isomers, and a comparison of the calculated density of electronic states with the spectrum measured in photoelectron experiments allows one to discriminate between the different possible isomers contributing to the measured spectrum. On the other hand, the structure of a large cluster cannot be determined by ab initio calculations because of the enormous computational work involved. The reactivity toward certain molecules provides an indirect way to determine the structure since the number of molecules adsorbed on the cluster surface gives information on the number of available adsorption sites and consequently on the shape of the cluster. The link with these experiments is mostly done by calculations that employ semiempirical many-body interatomic potentials. A difficulty in this context is the extent of modification of the original free cluster structure by the adsorbed molecules. Evidently the kind of adsorbed molecules should be such as to leave the geometry of the cluster unaffected. Another promising probe of cluster structure is provided by mobility experiments[6] in which the clusters accelerated by an electric field traverse a chamber that contains an inert gas. Collisions with the inert gas atoms retard the passing clusters, and the travelling time depends on the collision cross section σ which itself is sensitive to the cluster shape; that is, compact clusters have a lower collision cross section than those with a more open structure. To our knowledge, however, this technique has not been yet applied to transition-metal clusters. All the techniques applied, experimental and theoretical ones, lead to the conclusion that the clusters of d elements prefer compact structures as a way to maximize the interaction between the rather localized d orbitals. This rough statement has to be qualified in practice, and by looking at the details, one realizes that there is a high richness in the structure and properties of transition-metal clusters. The description of the experimental results on molecule adsorption and their interpretation in the light of semiempirical many-atom potentials is provided in section VII.

The other topic treated in detail in sections VIII−XII is the magnetism. A number of experimental measurements of magnetic moments (μ) have been performed, and as for bulk metals, substantial differences are found between different elements. For the typical magnetic metals, the evolution from the large moments of the free atoms to the lower moments in the bulk is not smooth. Instead, oscillations of μ with cluster size have been observed and, up to now, these are only partially understood. The most extended view is to ascribe the oscillation to atomic layering occurring during the growth of the clusters. Some of the metals that are nonmagnetic in the bulk phase also have interesting magnetic properties for small enough clusters. The prospects for technological application of the magnetic properties of clusters is enormous.[7−9] Some of the most interesting measurements of the magnetic properties involve large clusters. As stressed above, ab initio methods are difficult to apply in this case and a common practice is to use the tight binding method[10] to calculate the electronic structure with model cluster geometries: often a fragment of the bulk lattice and other times geometries derived from semiempirical interatomic potentials. There is a wealth of evidence that the tight binding method is well adapted for describing the interactions between the localized d electrons. To be fully realistic those calculations also have to take into account the additional effect of the sp electrons.

One of the typical questions in clusters is the size for which the properties have already converged to a stable value, and the cluster can be considered as a small piece of bulk material. The convergence is in general slow. But more important than the convergence to the bulk is the fact that the properties vary a great deal in the regime of small or medium sizes because this provides the potential for novel applications.

II. Noble Metal Clusters

A. Electronic Shell Effects in Clusters of Simple sp Metals

Cu, Ag, and Au atoms lie at the end of the 3d, 4d, and 5d periods, respectively. The d shell is filled with 10 electrons, and the valence shell contains a single s electron. In the bulk, the d band is well buried below the Fermi level. This leads one to expect some similarities between small clusters of the noble metals and the clusters of the alkali elements (Li, Na, K, Rb, Cs). For this reason it is convenient to begin by briefly reviewing the most remarkable characteristic of the alkali clusters. This consists of some properties, like the population abundance in cluster beams obtained by the usual gas aggregation techniques,[11] or the ionization potential,[3] that show a nonmonotonic variation as a function of cluster size, with maxima at some particular cluster sizes and sharp drops after those "magic" sizes. It was immediately realized that the magic numbers reflect electronic shell-closing effects.[11] The valence electrons of alkali clusters behave like independent electrons moving in an effective potential well that, in first approximation, has spherical symmetry around the cluster center. The spherical symmetry of the effective potential can be justified by treating the small alkali cluster as a liquid droplet. The alkali metals have low melting points, and these are known to be even lower in small particles.[12] In those circumstances the electrons fill shells 1S, 1P, 1D, 2S, ...

characterized by a principal quantum number (n = 1, 2, ...) and another quantum number giving the orbital angular momentum (l = 0(S), 1(P), ...). The degeneracy of each shell, that is the maximum number of electrons that the shell can accommodate, is $2(2l + 1)$. These electronic shells are separated by energy gaps, so clusters with the precise number of electrons required to fill the shells are more stable than clusters of neighbor sizes, just like the inert gas atoms in the periodic table. The observed magic sizes correspond to N = 2, 8, 18, 20, 40, 58, ... electrons, which are explained by a shell filling sequence $(1S)^2(1P)^6(1D)^{10}(2S)^2(1F)^{14}(2P)^6(1G)^{18}$... (capital letters are used to indicate the angular momentum of cluster orbitals to avoid confusion with orbitals of s, p, d, ... symmetry around individual atoms that will be used extensively in the paper).

The simple, approximately spherical, effective potential in which the electrons move arises from a sum of contributions

$$V_{\mathrm{eff}}(r) = V_{\mathrm{i}}(r) + V_{\mathrm{e}}(r) + V_{\mathrm{xc}}(r) \tag{1}$$

Here V_{i} is the external potential due to the ionic background. The weak pseudopotential of the alkali atoms allows for a simple modeling of V_{i} using the well-known jellium model of metal physics:[1] the ionic background is simulated as a continuous positive charge distribution (spherical in our case) of constant density, that is

$$\rho_+(\mathbf{r}) = \begin{cases} \bar{\rho}_+, & r < R \\ 0, & r > R \end{cases} \tag{2}$$

where R is the radius of the spherical cluster. This charge distribution produces an electrostatic potential

$$V_{\mathrm{i}}(r) = -\int_{\Omega} \frac{\rho_+(\mathbf{r}')}{|\mathbf{r} - \mathbf{r}'|} d^3r' \tag{3}$$

where the integral is extended over the volume Ω of the sphere. Since $\rho_+(\boldsymbol{r})$ is constant inside Ω, the integral gives

$$V_{\mathrm{i}}(r \le R) = \frac{2\pi}{3}\bar{\rho}_+ r^2 - 2\pi\bar{\rho}_+ R^2$$

$$V_{\mathrm{i}}(r \ge R) = \frac{-4\pi}{3} R\bar{\rho}_+ \cdot \frac{1}{r} \tag{4}$$

This potential is harmonic inside R and Coulombic outside, but the important message from eq 4 is the spherical symmetry of V_{i} around the cluster center. The second contribution in eq 1, V_{e}, is the classical electrostatic potential of the electronic cloud $\rho(\boldsymbol{r})$

$$V_{\mathrm{e}}(\mathbf{r}) = -\int \frac{\rho(\mathbf{r}')}{|\mathbf{r} - \mathbf{r}'|} d^3r' \tag{5}$$

Strictly speaking, this potential is not spherically symmetric for unfilled shells, but the assumption made for $\rho_+(\boldsymbol{r})$ suggests replacement of $V_{\mathrm{e}}(\boldsymbol{r})$ by its spherical average about the cluster center, $\bar{V}_{\mathrm{e}}(r)$. Finally, $V_{\mathrm{xc}}(\boldsymbol{r})$ is the nonclassical potential due to exchange and correlation effects between the electrons. Working within the framework of density functional theory (DFT)[13,14] and using the well-known local density approximation (LDA)

$$V_{\mathrm{xc}}^{\mathrm{LDA}}(\mathbf{r}) = [\epsilon_{\mathrm{xc}}(\rho) + \rho\epsilon'_{\mathrm{xc}}(\rho)]_{\rho=\rho(\mathbf{r})} \tag{6}$$

where $\epsilon_{\mathrm{xc}}(\rho)$ is the exchange-correlation energy per particle in a homogeneous system of density ρ and $\epsilon_{\mathrm{xc}}'(\rho)$ its first derivative with respect to ρ. Consistent with the above approximations, we can evaluate $V_{\mathrm{xc}}(\boldsymbol{r})$ using a spherically symmetric density distribution $\rho(r)$.

In summary, the approximations introduced above serve to justify the existence of an effective potential that is approximately spherical in which the electrons move, this potential giving rise to highly degenerate electronic shells. The approximations made are better in the neighborhood of closed shells. Clusters with open electronic shells are more complex: the electron cloud is not spherical and this induces a deviation of the cluster geometry from a sphere. These deformations have been taken into account by allowing for spheroidal (nonspherical) deformations of the continuous positive background.[15−17] The Jahn−Teller-type deformations of the positive background lift the degeneracies of the electronic shells. The shape deformations can be understood as a way to optimize local charge neutrality (cancellation between positive and negative charge densities), which is taken as an extreme assumption in the ultimate jellium model.[18] Despite the nonspherical deformations of the clusters, the fact that large stability is achieved at shell closing (that is, for the truly spherical clusters) is preserved in the improved spheroidal models, although the magnitude of the shell closing effect is somewhat reduced. This is good indeed, since the "purely spherical" models overestimate the magnitude of shell closing effects. A consequence of the shape deformations for small clusters is the occurrence of even−odd effects in the abundance, ionization potential, and other properties.[3,15,16] This is due to the almost complete lifting of the orbital degeneracy: thus clusters with a doubly occupied HOMO level are more stable and have a larger ionization potential than clusters with a singly occupied HOMO. This even−odd effect has been observed in the relevant measured quantities,[3] although its magnitude is weaker than the magnitude of the shell closing effect.

B. Shell Effects in Noble-Metal Clusters

Experiments for noble-metal clusters (Cu_N, Ag_N, Au_N)[19,20] indicate the existence of shell effects similar to those observed in alkali clusters. For instance, the mass spectrum of Ag_N^+ clusters obtained by bombarding the metal with inert-gas ions shows two types of anomalies. The first one, observed only for small clusters, is an odd−even alternation of the cluster intensities, such that the intensity (population) of odd-N clusters is greater than the population of even-N clusters. Its explanation is the same as that for alkali-metal clusters. The other anomaly, more relevant for our present discussion, is that a steep drop of the cluster intensities occurs after the sizes

$N = 3$, 9, 21, 35, 41, and 59. By focusing on the 5s electrons of the Ag atoms, the experimental results can be explained by using a model similar to that for alkali clusters, that is, assuming that the valence electrons are confined in a smooth spherically symmetric potential well. In the bombardment experiments the Ag_N^+ clusters are born ionized, so the mass spectrum reflects the relative stabilities of charged clusters in which the number of electrons is $N - 1$. From the list given above, we find $N - 1 = 2$, 8, 20, 34, 40, 58, ..., which reproduce the same shell closing numbers of alkali clusters. Mass spectra of Cu_N^+ and Au_N^+ also show the same magic numbers. Furthermore, negatively charged clusters (Cu_N^-, Ag_N^-, Au_N^-) are produced by the same technique, and their magic numbers are $N = 7$, 19, 33, 39, 57, ..., but we can notice that those clusters again contain $N + 1 = 8$, 18, 34, 40, ... electrons. Measurements of the ionization potential of Cu clusters by Knickelbein[21] show the expected drops after the electronic shell closings.

Photoelectron spectroscopy (PES) studies of cluster anions (Cu_N^-, Ag_N^-, Au_N^-) give direct information on the structure of the spectrum of electronic energy levels. In these experiments a cluster anion is irradiated with laser light of fixed photon energy $\hbar w$. The photon removes an electron from the least bound molecular orbital or from a deeper orbital. The difference $\hbar w - E_{kin}$, where E_{kin} is the kinetic energy of the detached electron, gives a direct measurement of the binding energy of the orbital. The structure of the spectrum is very rich and every cluster species has its own fingerprint. The individual peaks arise from photodetachment transitions between the ground state of the anion and the ground and excited states of the neutral cluster. The photoelectron "threshold" (or energy to remove an electron from the least bound orbital of the X_N^- cluster) can be taken as an estimate of the electron affinity EA. This quantity is the difference

$$\mathrm{EA} = E(X_N) - E(X_N^-) \qquad (7)$$

between the energies of neutral and the anionic clusters. If the corresponding neutral cluster X_N has closed shells, the electron is ejected from the lowest unoccupied molecular orbital (LUMO) of X_N. Consequently, the photoelectron threshold should reflect the shell effects. Indeed, measured threshold detachment energies of Ag_N^- [22] and Cu_N^- [23,24] show drops between $N = 7$ and 8 and between $N = 19$ and 20, which again indicate major shell closings $(1S)^2(1P)^6$ and $(1S)^2(1P)^6(1D)^{10}(2S)^2$, respectively. Encouraged by these features, Penzar and Ekardt[16] have applied the spheroidal jellium model to Cu clusters. Over a wide range of cluster sizes, the trend in the calculated electron affinities agrees with experiment.

Since PES also probes deeper orbitals, a comparison with PES data allows for a more stringent test of the validity of the jellium model. Cha et al.[25] have analyzed the region of the spectrum of Cu_N^- clusters (with $N = 1-18$) that is predominantly of s-like character (4s derived orbitals). Nearly all observed peaks can be qualitatively assigned to the electronic shells of the ellipsoidal jellium model if one takes into account additional effects such as shake up processes (simultaneous excitation of bound electrons accompanying the photoemission process), multiplet splittings (caused by the spin−spin interaction of the electrons in the cluster), and s−d hybridization (for orbitals located close to the 3d band).

Chemical probes also point to electronic structure that can be understood in terms of the spherical jellium model. Winter et al.[26] have recorded the mass spectrum of Cu clusters generated by laser vaporization of copper after these have passed through a flow tube reactor with O_2 added to the gas flow. The observed result is that clusters Cu_{20}, Cu_{34}, Cu_{40}, Cu_{58}, and Cu_{92} are unreactive toward O_2, as well as several others. The lack of reactivity is ascribed to the closed shell electronic structure of these clusters that in a sense reminds us the inert character of noble gases.

Despite the successful description of some features of noble metal clusters by a jellium model that neglects the d cores, the d electrons are required to explain a large number of properties of noble-metal clusters. The d electrons contribute to the bonding in a crucial way. Calculations[27] for doubly charge silver clusters, Ag_N^{2+}, using the simple jellium model indicate that the model underestimates the binding energy of these clusters in comparison to experiment,[28,29] as a consequence of neglecting the d electrons. The contribution of the d band to the cohesive energy of noble metals is also well documented.[1,30,31]

C. d Electrons in Noble-Metal Clusters

The analysis in section II.B provides information on the electronic structure near the top of the occupied molecular states of the cluster. The next question is how much deeper one can probe into the structure of electronic levels of noble-metal clusters. Smalley and workers[24,32] have used ultraviolet electron spectroscopy (UPS) to probe the 3d electrons of Cu cluster anions, Cu_N^-, with N up to 410. Probing the d electrons requires high photon energies. They found a large peak, roughly 2 eV higher than the weak initial threshold, and this large peak moves smoothly with cluster size. For the small clusters its position merges with the position of the d levels of the copper atom. For the large clusters, the peak matches well with the sharp onset of the 3d band in the UPS of bulk Cu. For all those clusters, it seems safe to attribute this feature to the photodetachment of primarily 3d-type electrons. Unlike the large size-dependent variations of the UPS threshold, which is associated to the 4s electrons (and gives the electron affinity), the 3d feature shifts monotonically with the cluster size: the 3d electrons are more core-like and should be only mildly influenced by the details of the cluster surface. The onset of the 3d band sharpens as N increases, and this was interpreted as an indication that the larger clusters may already be crystalline.[32]

In the band picture of solid noble metals, the valence band contains the localized d electrons as well as the extended s electrons and s−d mixing is substantial.[1] The picture of valence electrons is then far from that of the free electrons in alkali metals. It

is, therefore, intriguing how well the shell model also works in noble metals. Fujima and Yamaguchi[33] have performed DFT calculations for Cu_N clusters with sizes up to $N = 19$ and a variety of model structures: Cu_6-octahedron, Cu_8-cube, Cu_{12}-icosahedron, Cu_{13}-icosahedron, Cu_{13}-cuboctahedron, Cu_{15}-rhombic dodecahedron, Cu_{19}-combination of cuboctahedron and octahedron. An analysis of the molecular orbitals (MO) shows that these can be classified into two types. The first type is formed by MOs built from atomic 3d orbitals. These span a narrow energy range of a width comparable to that of the d band of the solid and do not mix much with the second type of MOs, which are derived from atomic 4s−4p orbitals. The 3d charge is localized around atoms, whereas the sp charge is extended over the whole cluster. Fujima and Yamaguchi related their results to the shell model. Disregarding the MOs with d character on the atoms, the sequence of the remaining MOs can be reproduced rather well by considering a spherical model potential with a small anharmonic term (this is essentially the form of the effective potential one obtains in the spherical jellium model). However, when the cluster lacks a central atom, as is the case of the icosahedral structure of Cu_{12}, a 3-dimensional Gaussian potential barrier had to be added to simulate the missing atom. The good one-to-one correspondence between the energy levels of the full ab initio calculation and those of the simple model potential leads to the explanation of why the shell model is applicable to Cu clusters. The d band is located in energy between the 1S and the 1P levels of the shell model for $3 \leq N < 8$ (more precisely, between the MOs with overall symmetries comparable to those of the 1S and 1P jellium orbitals), between the 1P and 1D levels for $9 \leq N < 18$, between the 1D and 2S levels for $19 \leq N < 20$, and so on. The d levels are always filled. Massobrio et al.[34] have performed more accurate DFT calculations for Cu_N clusters, although only for $N \leq 10$. The equilibrium geometries were obtained by minimization of the energy with respect to all the nuclear coordinates using the Car−Parrinello ab initio molecular dynamics method.[35] The structures obtained for Cu_6 (pentagonal pyramid; C_{5v} symmetry) and Cu_8 (D_{2d} symmetry) are less symmetric than the model structures assumed by Fujima and Yamaguchi. Massobrio et al. obtain, in general, ground-state and local minimum structures similar to those of Na_N, although Cu_N clusters tend to prefer more compact arrangements. The angular decomposition of the electronic wave functions shows that these bear some relation to the shell model, although this character is significantly less pronounced than in Na_N clusters. The degree of s−d hybridization observed in the calculations of Massobrio et al. appears to be larger compared to Fujima and Yamaguchi. A likely reason is the more symmetric geometries assumed by the later authors. This view of the interplay between s and d electrons in noble-metal clusters will be very useful later on when discussing some features observed in the magnetism of Ni clusters.

Massobrio et al.[36,37] have extended their first principles calculations to interpret the photoelectron spectra of Cu_N^- clusters measured by Cha et al.[25] Two factors were found crucial to bring theory in close agreement with experiment. The first is the accurate determination of the equilibrium atomic geometries of the anionic clusters. A linear chain was obtained for Cu_3^-, a planar trapezoidal configuration (C_{2v}) for Cu_5^-, two nearly degenerate isomers with C_{3v} (capped octahedron) and D_{5h} (pentagonal bipyramid) symmetries, respectively, for Cu_7^-, and a bicapped pentagonal bipyramid (C_2 symmetry) for Cu_9^-. Simple consideration of the electronic density of states obtained from the calculated single-particle eigenvalues was found inadequate to interpret the photoelectron spectrum because the one-electron picture neglects the interaction between the hole created by the removal of one electron and the rest of the system. So the second key factor is the inclusion of final state effects. To account for these, vertical one-electron excitation energies were calculated as a difference of self-consistent total energies (ΔSCF) in the context of DFT, that is $\Delta E_{\mathrm{exc}}^{\mathrm{SCF}}(k) = E_{\mathrm{fin}}^{\mathrm{SCF}}(k) - E_{\mathrm{init}}$. Here E_{init} is the total energy of the initial state of Cu_N^-, characterized by occupations $(n_1...n_k...n_M)$ of the M cluster eigenstates and $E_{\mathrm{fin}}^{\mathrm{SCF}}(k)$ is the total energy when an electron has been removed from a given state k. This energy is obtained in a constrained calculation for the configuration $(n_1...n_k-1...n_M)$ in which the wave function of the kth eigenstate is kept frozen whereas the other wave functions are allowed to relax. In this way the screening effect is included (although the relaxation of the hole is not). With this ΔSCF procedure a consistent interpretation of the photoelectron spectra of Cu_3^-, Cu_5^-, Cu_7^-, and Cu_9^- was achieved. The early interpretation by Cha et al.[25] in terms of the ellipsoidal jellium model remains valid to a large extent, although the cluster states display increased hybridization. The comparison with experiment supports the C_{3v} geometry for Cu_7^-. With an additional simplification in the treatment of final state effects, Massobrio et al.[37] were also able to account for finite temperature effects. They ran molecular dynamics simulations for Cu_7^- at $T =$ 300−400 K and took temporal averages of the density of states and of the excitation energies. Thermal broadening led to a splitting of the first peak in the calculated photoelectron spectrum of this cluster, whose magnitude agrees well with the experimental splitting of 0.12 eV.

Although only DFT calculations have been reviewed above, work has also been performed for clusters of coinage metals using quantum chemical methods. Bauschlicher and co-workers have studied dimers, trimers, tetramers, and pentamers, neutral and negatively charged, with the purpose of calculating electron affinities.[38−41] For the Cu clusters they performed all electron calculations, but the relativistic effective core potential (RECP) developed by Hay and Wadt[42] was used for Ag and Au. Electronic correlation was accounted for by performing modified coupled pair functional (MCPF) calculations[43,44] based on a SCF reference configuration and SCF molecular orbitals. All the neutral homonuclear triatomics have ground-state structures that are a slight Jahn−Teller distortion away from an equilateral triangle. A linear

isomer lies higher in energy, for instance, 0.28 eV in Cu_3. However, the corresponding negative-ion trimers have a linear structure, formed by attaching the extra electron into the singly occupied σ_u orbital of the neutral linear isomer. This orbital has bonding character. Hence, the linear structure becomes favored over the triangular structure that involves attaching the extra electron into a nonbonding e' orbital. The neutral tetramers have a planar rhombus structure, and the pentamer is a planar trapezoid,[41] in analogy with simple alkali clusters.[45] The optimized structures of the negative tetramer ions are very similar to those of the neutrals. The case of the pentamer is controversial. Electron spin resonance (ESR) experiments for Cu_5 and Ag_5 were first interpreted as suggesting that the ground-state geometry is a distorted trigonal bipyramid.[46−48] This structure is consistent with the observation that there are three kinds of atoms and that one of the pairs has a much larger spin density than the other atoms. Bauschlicher and co-workers[41] then noticed that the spacial distributions of the open-shell densities in planar trapezoidal Ag_5 and Cu_5 are consistent as well with the spin densities from the ESR experiment. The observed odd−even oscillation of the electron affinity of Cu and Ag clusters with cluster size[22,25] was interpreted in terms of the bonding character of the molecular orbital occupied by the additional electron: that electron occupies an antibonding orbital in Cu_2^- and Cu_4^- while for Cu_3^- and Cu_5^- it goes to a bonding orbital. The calculated values of the electron affinities underestimate the measured ones, but excellent agreement can be obtained by scaling the theoretical values by a factor of 1.3. A lower scaling factor of 1.09 also brings agreement for the ionization potentials.

Heteronuclear dimers and trimers were also studied.[41] The optimal structures of the neutral trimers are triangular, as for the homonuclear ones. For the only negative trimer studied in detail, Ag_2Au^-, the structure was linear so a linear structure is expected for all other heteronuclear trimers, again in agreement with the homonuclear case. To a good approximation the electron affinities of the heteronuclear trimers can be predicted from a weighted average of the corresponding homonuclear systems.

Akeby et al.[49] have studied Cu_N^- cluster anions with N up to 10. Cu was treated as a one-electron atom, and the core, including the 3d electrons, was described by an effective core potential.[50] The calculations were performed at the CI (configuration interaction) level. Core−valence correlation effects, which were found to be crucial for obtaining quantitative results and also in the search for geometries, were included through a core-polarization potential.[51] Further approximations were that nearest-neighbor distances were fixed at the bulk metal value, and fine optimization of the different isomeric geometries was not allowed. The assignment of ground-state geometries was made by taking into consideration not only the calculated binding energies, but also a comparison of the vertical affinities and HOMO−LUMO gaps with the experimental values.[23,24] In most clusters, but not always, the assigned ground-state isomer coincides with that having the highest binding energy. Unsurprisingly the structures are often qualitatively similar to those of anionic lithium clusters.[52] The calculated binding energy of Cu_2^- is 0.99 eV. This is substantially smaller than the experimental binding energy of 1.57 ± 0.06 eV,[23] and the binding energies of the larger clusters are also expected to be underestimated as a consequence of neglecting d bonding, already discussed at the end of section II.B in the context of the jellium model. This missing d-bonding contribution is evident from a comparison of the binding energy of Cu_2^- with that obtained in an all-electron calculation.[39] The all-electron result is 1.31 eV. For the assigned ground-state geometries, the vertical EAs follow the experimental trend precisely as a function of N, with an overall shift to smaller values.

Ag_N clusters ($N = 2-9$) and their positive and negative ions have been studied by Bonacic-Koutecky and co-workers,[53,54] who give extensive reference to previous work. An effective core potential that accounts for relativistic effects and core−valence correlation was used for Ag, which was treated as a one-valence-electron atom. Cluster geometries were optimized at the Hartree−Fock level and sometimes using the complete active space SCF method. For the different isomers obtained in this way, explicit correlation treatments for the 5s electrons were carried out using a multireference SCF procedure to recalculate energies. The CI calculations allow one to draw conclusions about the influence of the net charge on the geometry. Concerning trimers, only the anionic one, Ag_3^-, is linear whereas the neutral and cationic trimers are planar. All cationic clusters larger than tetramers assume three-dimensional (3D) geometries, starting with Ag_5^+, which is a trigonal bipyramid. However, the competition between 2D and 3D structures is more pronounced for neutral and anionic clusters. Ag_5 and Ag_5^- are still planar (trapezoidal), and Ag_6, which marks the transition to 3D structures in the neutral case, is a "flat" pentagonal pyramid. 3D structures of anion clusters also begin with Ag_6^-, which is a bicapped deformed tetrahedron. The net charge also influences the precise 3D geometries adopted for $N \geq 7$. As seen, the predictions for small clusters agree with the work of Bauschlicher.[41] Binding energies per atom increase with cluster size and indicate a slight higher stability of systems with eight valence electrons. This becomes confirmed by a local maximum of IP at Ag_8 and a large drop between Ag_8 and Ag_9 and also by the pronounced minimum of EA at Ag_8. The measured photodetachment spectra[55,22] of Ag_N^- anions were compared with the calculated vertical detachment energies and with the energies of the excited states of the neutral species at the geometries of the anions. This allowed, in all cases, an unambiguous assignment of the anionic cluster geometries, which confirmed the results of the total energy optimizations. In particular, an outstanding agreement between theory and experiment was achieved for the vertical detachment energies.

The theoretical works described above, studying the detailed structure of noble-metal clusters by DFT

and quantum chemical methods, are restricted to small clusters. Recent work points to a controversial situation concerning the structure of medium size and large gold clusters. X-ray powder diffraction studies of Au_N nanoclusters of sizes $N = 38$, 75, 101, 146, 200, 225, and 459 grown with passivating organic molecules have been interpreted as revealing ordered structures with an underlying fcc lattice: truncated octahedra for $N = 38$, 225, and 459 and truncated decahedra for the rest.[56] But Garzon and co-workers[57] have performed calculations using semiempirical many-atom potentials whose results, corroborated by DFT calculations,[58] indicate instead that the structures for many sizes between $N = 38$ and 75 are disordered. For two cases studied in detail, Au_{38} and Au_{75}, calculated structure factors for those disordered structures agree as well with experiment as the structure factors from the fcc-ordered ones.

III. General Bonding Properties in Clusters of Transition Metals

One of the recurrent themes in the physics and chemistry of clusters is the study of similarities and differences between the properties of clusters and those of the corresponding bulk material. The beauty of clusters comes from the fact that their properties are not only size dependent but that this size variation is nonmonotonic. This size-specificity has enormous potential interest for technological applications. On the other hand, one should also recognize that some trends along groups or across periods of the periodic table are already imprinted in clusters with only a few atoms. This is the case for crystal cohesive properties of 3d and 4d metals. Painter[59] has performed DFT calculations for small clusters of 3d elements. To remove specific variations due to symmetry and size effects, Painter constrained the clusters to have six atoms in fixed symmetry. This was selected to be octahedral since it defines a lattice fragment component of the fcc, bcc, and hcp transition-metal lattices. Interatomic bond lengths were allowed to relax. The 3d metals exhibit a broad spectrum of mechanical properties.[1] The experimental cohesive energy E_c of Sc is 3.90 eV/atom.[60] This quantity increases for Ti and has a maximum for V. After this maximum it decreases, showing a minimum for Mn (2.92 eV/atom). E_c increases again to the right of Mn, having a broad maximum for Fe, Co, and Ni, and finally it decreases again for Cu. The trend of the Wigner-Seitz radius R_{WS} is simpler. R_{WS} has a roughly parabolic behavior (lower values in the middle of the series) with Mn deviating, although rather weakly, having a value of R_{WS} slightly larger than the interpolated value. This small deviation reflects the minimum of E_c. These trends have been reproduced by DFT band calculations for the bulk metals performed by Moruzzi et al.,[61] except for some weak deviations from the trend to be discussed below. Painter demonstrated that the trends in the binding energy and interatomic distance of the octahedral clusters reproduce the experimental trends for the solid metals well, with small deviations that are, precisely, the same as those found for the DFT bulk calculations: the first maximum of E_c occurs for Ti (instead of V), the second maximum for Co (instead of Ni), and nearly equal values occur for Cr and Mn (instead of a clear minimum for Mn). Those differences with respect to the experimental trend, since they occur for both bulk and cluster calculations, are ascribed to the LDA approximation used for exchange and correlation. Of course, although the trend is well reproduced, the binding strength is lower for clusters. Interatomic distances are also smaller. The conclusion is that the trend in the cohesive energy originates largely on the localized near-neighbor interactions present within the primitive cluster itself.

Table 1. Calculated Binding Energy Per Atom E_b, Distance D from the Atoms to the Center of the Cluster and Average Magnetic Moment Per Atom $\bar{\mu}$ for Octahedral (X_6) Clusters[62]

cluster	E_b (eV)	D (au)	$\bar{\mu}$ (μ_B)
Y	3.53	4.40	0.00
Zr	5.23	3.96	0.33
Nb	5.07	3.64	0.67
Mo	4.05	3.40	0.33
Tc	4.91	3.36	0.33
Ru	4.70	3.40	1.00
Rh	4.03	3.48	0.99
Pd	3.14	3.50	0.00
Ag	1.56	3.76	0.33
Cd	0.39	4.48	0.00

A similar study was done by Zhang et al.[62] for clusters of 4d elements. Again, a model of a regular octahedral cluster with six atoms was employed, and the clusters were allowed to relax radially. The calculated binding energies per atom and the distance d from the atoms to the cluster center are given in Table 1. Going across the 4d period, the binding energy E_b presents two maxima, at Zr and Tc, respectively, separated by a minimum at Mo. Furthermore, E_b drops to rather small values near the end of the period, for Ag and Cd. This is also the general behavior of the experimental cohesive energy of the bulk metals.[60] The only small differences are that the first maximum for the bulk metals occurs for Nb (instead of Zr) and the second maximum for Ru. It is convenient to stress that the metals Tc and Ru have very similar cohesive energies and Tc_6 and Ru_6 have very similar binding energies, so the discrepancies are very minor and one can conclude that a good qualitative correspondence exists between clusters and bulk concerning the variation of binding energy across the 4d period. The measured Wigner−Seitz radii also have a simple parabolic variation with a minimum around the middle of the period, and the calculated interatomic distances and distance D of Table 1 roughly agree to this behavior. The nearly parabolic behavior of E_b is a consequence of the change from bonding to antibonding character of the d orbitals as the d-band filling increases. Also, in the same way as for the 3d clusters, binding energies and interatomic distances are smaller than in the bulk. There is also a striking correlation between the width of the occupied valence band in clusters and bulk metals.[62] Although the width of the band of the clusters is smaller, a parabolic variation between Y and Pd is calculated in both cases, whereas Ag and Cd follow a completely different trend because the

4d band is filled in those two cases and the 5s-derived band of nearly free electrons is very broad.

IV. Electronic Structure of Clusters of Transition Metals

For very small clusters, diffraction techniques are not useful to elucidate their structure but theoretical calculations can be performed with some confidence because a complete minimization of the total energy with respect to all the atomic positions can be performed using methods based on the DFT formalism. A few representative examples are now discussed.

A. Nickel Clusters

Reuse and Khanna[63] have employed an LCAO molecular-orbital approach within the DFT formalism to study Ni_N ($N = 2-6$, 8, 13). The local spin-density approximation (LSDA)[14] was used for exchange and correlation effects, and the inner cores were replaced by nonlocal pseudopotentials. Their main results are that the binding energy varies with size in a nonmonotonic way and that all the clusters have nonzero spin in their ground state (magnetic properties will be discussed in more detail later). Up to five atoms, Reuse and Khanna tried several starting geometries and performed structural relaxations, allowing the cluster to distort in order to minimize the energy. The ground-state structures are plotted in Figure 1. For Ni_2 they found the ground state to have a total spin $S = 1$ with a bond length of 3.78 au and binding energy E_b of 3.32 eV (or 1.61 eV/atom). The spin $S = 1$ is consistent with early measurements on matrix isolated clusters.[64] The experimental bond length is between 4.07 and 4.16 au, and the estimated binding energy is 2.1 eV.[65,66] The errors are typical of the LDA: an overestimation of the binding energy and a contraction of the bond length. The geometry of Ni_3 in a solid argon matrix is C_{2v} with an apex angle estimated between 90° and 120°.[67] Some previous calculations had given instead a linear ground state.[68] Reuse and Khanna obtain a C_{2v} ground state with $S = 1$ (the same as in the experiment) but with an apex angle of only 61°. The calculated binding energy is 1.96 eV/atom. They also found C_{2v} ($S = 2$) and linear ($S = 2$) isomers, higher in energy (0.03 and 0.05 eV/atom, respectively) than the ground state. Two degenerate structures (binding energy of 2.34 eV/atom) form the ground state of Ni_4: one is a compact D_{2d} geometry and the other is a square and both have $S = 3$. For Ni_5, the ground state is a triangular bipyramid with $S = 4$ and $E_b = 2.83$ eV/atom. This triangular bipyramid is 0.2 eV/atom more stable than a square pyramid. For larger clusters, the structural study was restricted. An octahedron, which is a fragment of the fcc lattice, was initially assumed for Ni_6, although this was allowed to distort by permitting different Ni−Ni bond lengths in the central square and between apex and central atoms. The octahedron showed only minor distortions, and the ground state has $S = 3$ and $E_b = 3.27$ eV/atom. This was exactly the binding energy obtained for Ni_8, for which only a perfect cube geometry was studied ($S = 4$). Finally, for an icosahedral structure of Ni_{13} (only structure studied), $S = 4$ and $E_b = 4.26$ eV/atom were obtained. States with $S = 5$ and 6 were marginally above this state. The geometries up to Ni_6 have been confirmed by other DFT calculations.[69,70] An extensive study of the low-lying electronic states of Ni_2 has been performed by Michelini et al.[71] These authors also studied different conformational isomers in Ni_3 and Ni_4, taking care in distinguishing between true local minima and saddle points through a vibrational analysis.

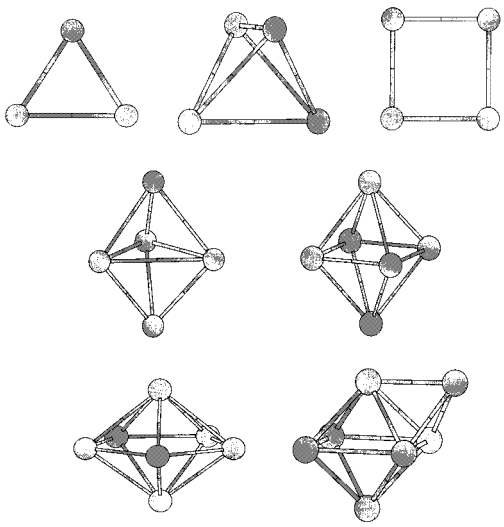

Figure 1. Ground-state structure of small nickel clusters (Ni_3-Ni_7) obtained by DFT.[63,73] Two nearly degenerate isomers are shown for Ni_4 and Ni_7.

These results reveal the complexity of clusters of transition metals: there are normally several low-lying states with very close energies. One of the reasons is the competition between (i) compact structures maximizing the number of bonds and (ii) directional bonding compatible with the orientation and filling of the d orbitals. Let us consider two illustrative examples. The triangular C_{2v} configuration of Ni_3 optimizes the number of bonds but forces d orbitals into a symmetry which is not optimal for their bonding (the d orbitals in an atom have a square symmetry). In contrast, the linear geometry of Ni_3 permits undistorted d-orbital combinations to form but it has fewer bonds. The ab initio calculations show that the linear isomer is only marginally less stable. The second example is Ni_4, for which a similar competition exists between a compact D_{2d} structure (a rhombus bent into a butterfly structure) and a planar square. Again, both structures are equally stable.

Using the binding energies, Reuse and Khanna have calculated fragmentation channels, that is, the energy required to break the Ni_N cluster into two fragments

$$Ni_N \rightarrow Ni_M + Ni_{N-M} \quad (8)$$

of sizes M and $N-M$. The channel requiring less energy is always the loss of a single atom ($M = 1$), except for Ni_4, which prefers to dissociate into two Ni_2 clusters. The fragmentation energies amount to

3.21, 2.68, 2.92, 4.81, and 5.47 eV for Ni_2, Ni_3, Ni_4, Ni_5, and Ni_6, respectively, so Ni_3 has the lowest fragmentation energy. These results agree with collision-induced fragmentation experiments.[72]

Ni_7 was studied in detail by Nayak et al.[73] Experiments analyzing the reactivity with N_2 suggest that the structure of this cluster is an octahedron with an atom capping one of its faces,[74] while early ab initio calculations had predicted a pentagonal bipyramid.[75] Nayak et al. first noticed that the pentagonal bipyramid is also consistent with a part of the reactivity results, so those experiments do not completely rule out the pentagonal isomer. Nayak et al. then optimized both structures using DFT and found that these are nearly degenerate within the precision of their calculation (total binding energies of 3.70 eV/atom for the capped octahedron and 3.65 eV/atom for the bipyramid). Surprisingly the magnetic moment was the same for both isomers, 1.14 μ_B/atom (μ_B = Bohr magneton), in fair agreement with the experimental result of 1.53 μ_B/atom.[76] To get further insight into the stability of those two isomers, they performed molecular dynamics simulations using the many-body interatomic potential of Finnis and Sinclair.[77] This potential has the form

$$V = \epsilon \sum_i \left[\frac{1}{2} \sum_{j \neq i} \left(\frac{a}{r_{ij}} \right)^n - c \rho_i^{1/2} \right] \quad (9)$$

where

$$\rho_i = \sum_{j \neq i} \left(\frac{a}{r_{ij}} \right)^m \quad (10)$$

and r_{ij} is the distance between atoms i and j. The constant a is the bulk lattice constant, c is a dimensionless parameter, ϵ is a parameter with dimensions of energy, and the exponents m and n are integers. The square root term in the attractive part of the potential accounts for the many-body character of the interaction. For Ni, the parameters have been obtained by fitting to bulk and repulsive and attractive interactions are governed by the values $n = 9$ and $m = 6$, respectively. The Finnis−Sinclair potential predicts that the two structures of Ni_7 are nearly degenerate within the accuracy of the calculation, but the MD simulations show that the catchment area for the capped octahedron is much higher than that for the pentagonal bipyramid. In summary, neither the chemical reactivity nor the magnetic experiments are inconsistent with the presence of the two isomers in a molecular beam. The results were confirmed by Desmarais et al.,[78] who performed a more complete study of Ni_7 (and Ni_8 also). A number of different geometries were investigated within the DFT formalism, and the possible Jahn−Teller distortions were examined. The ground state of Ni_7 was a capped octahedron, and a pentagonal bipyramid (Jahn−Teller distorted) was found as the first low-lying isomer, 0.07 eV/atom above the capped octahedron. The ground state of Ni_8 was a distorted bisdisphenoid structure with D_2 symmetry (it can be seen as a rectangular Ni_4 cluster with a dimer above the first diagonal of the rectangle and another dimer below the second diagonal), and several isomers (capped pentagonal bipyramid, bicapped trigonal prism, star, cube, and square antiprism) lie close to each other within a range of only 0.07 eV/atom above the ground state.

Ni_{13} was subsequently studied in more detail by Reuse, Khanna, and Bernel.[79] Clusters with perfect icosahedral (I_h) and cuboctahedral (O_h) shapes (the cuboctahedron is a piece of an fcc crystal) were first optimized with respect to their radial size for several possible spin configurations. The lowest energy is obtained for the icosahedral geometry and $S = 4$ (E_b = 4.23 eV/atom). The HOMO has a degeneracy of five and is occupied by only three electrons. The cluster, therefore, prefers a Jahn−Teller distortion, and by allowing all the interatomic distances to vary independently, the cluster distorts to a D_{3d} symmetry, producing an increase in the binding energy of 0.16 eV. The distortion is nevertheless very small, and the total spin does not change. $S = 4$ corresponds to a magnetic moment $\bar{\mu} = 0.61\ \mu_B$ per atom.

The isomerism that occurs in small Ni clusters may have a role on the interpretation of the photodetachment spectra of cluster anions. In the photodetachment process, a transition occurs from the cluster anion in its ground electronic state to a state of the neutral cluster with the same geometry of the anion. According to the ab initio calculations,[80] Ni_2^- has two isomers with slightly different bond lengths (d = 2.19 and 2.21 Å, respectively). The binding energies are very close (2.38 and 2.35 eV, respectively), and the spin multiplicities (2 and 4, respectively) are different. The study of neutral Ni_2 clusters with the same bond lengths as the anions gave triplet and singlet states for d = 2.19 Å and triplet and quintet states for d = 2.21 Å. The photodetachment spectrum of Ni_2^- measured by Ho et al.[66] identified four groups of electronic transitions: band *X* (0.9 eV), band *I* (1.7−2.1 eV), band *II* (2.1−2.9 eV), and band *III* (≥2.9 eV). The spectrum was interpreted by Weber and Jena[80] as having contributions from those two nearly degenerate anionic states. Band *I* was assigned to transitions from Ni_2^- (doublet) to neutral Ni_2 (triplet) and also from Ni_2^- (quartet) to neutral Ni_2 (triplet). Band *II* was assigned to transitions from Ni_2^- (quartet) to Ni_2 (quintet), and band *III* was assigned to transitions from Ni_2^- (doublet) to Ni_2 (singlet). The origin of band *I* was left unassigned.

Ni_3^- also has two structures, linear and triangular, nearly degenerate (atomization energies of 5.04 and 5.01 eV, respectively) and with the same spin multiplicity (both are quartets), although a barrier of 0.8 eV separates those two structures. Consideration of the two Ni_3^- isomers and of different spin states of the corresponding neutrals helps to interpret the photodetachment experiments for this cluster.[81]

Reuse and Khanna[82] have calculated the photoabsorption spectrum of Ni_N clusters with $N = 2-6$ and 13 in the context of DFT. The clusters geometries were taken from their earlier work.[63] Using first-order perturbation theory in the framework of quantum electrodynamics, the total photoabsorption cross

section $\sigma(\Omega)$ can be expressed

$$\sigma(\omega) = \frac{3}{4}\pi^2\alpha\sum_{i\neq j}\delta(\hbar\omega - E_{\mathrm{fi}})E_{\mathrm{fi}}|\mathbf{P}_{\mathrm{fi}}|^2 \qquad (11)$$

taking into account the dipolar electric approximation for the interaction between photons and the electrons in the cluster. In this equation, $\hbar\omega$ represents the energy of the incident photon, α is the fine structure constant, $E_{\mathrm{fi}} = E_{\mathrm{f}} - E_{\mathrm{i}}$ is the energy of the transition between the initial $|i\rangle$ and final $|f\rangle$ electronic states of the cluster. $\boldsymbol{P}_{\mathrm{fi}}$ is the matrix element of the dipole operator $\boldsymbol{P}$ between the initial and final states. This equation is already averaged with respect to all orientations of the cluster and then with respect to polarization of the incident photon. The ground state $|i\rangle$ and the excited state $|f\rangle$ were described by Slater determinants built from Kohn−Sham orbitals: the Slater determinant of the ground state is built from occupied orbitals and that of the excited state is constructed by moving an electron from an occupied orbital to an initially unoccupied orbital with the same spin. The results for $\sigma(\omega)$ reveal several interesting features. (1) The spectrum becomes richer as N increases. (2) The positions of the main peak (most intense transition) and secondary peaks in the spectrum change with size. (3) Two isomers were considered for Ni_4. The square isomer has a main peak at 3.09 eV and the D_{2d} isomer at 3.36 eV. This indicates that the photoabsorption spectrum can provide a fingerprint for the geometry, as also pointed out for alkali clusters and semiconductor clusters.[83]

B. Iron Clusters

Ballone and Jones[84] have studied small Fe clusters using ab initio DFT molecular dynamics. It is interesting to compare their results, given in Figure 2, with those for Ni_N discussed above. The ground state of Fe_3 is an equilateral triangle (C_{3v} symmetry) with $S = 4$, bond length d = 4.04 au, and binding energy $E_b = 3.04$ eV/atom. For comparison, we recall that the triangle is not equilateral for Ni_3 and its total spin is lower, $S = 1$. Low-lying isomers, with the same geometrical structure and different spins, $S = 3$ and 5, respectively, were also found, as well as a high-lying C_{3v} isomer with $S = 0$ and a linear, asymmetric form (the two bond lengths different). So, similar to the case of Ni_3, a variety of isomers are found. Although earlier DFT calculations[85,86] predicted for Fe_4 a tetrahedral (T_d) structure, the ground state found by Ballone and Jones can be viewed as a distorted tetrahedron opened up into a butterfly (C_{2v} symmetry), with $S = 6$ and $E_b = 3.55$ eV/atom. Two low-lying isomers were found with $S = 7$ (more open) and 5 (more compact) and also a square isomer lying 0.74 eV/atom above the most stable C_{2v} structure. The C_{2v} structure of Fe_4 is rather similar to the D_{2d} structure of Ni_4, but the planar isomer is less stable in the Fe case. There is agreement between the predictions of the structure of Fe_5 by Castro[86] and Ballone:[84] the lowest energy structure is a trigonal bipyramid, with $E_b = 3.90$ eV/atom and $S = 7$. There are several low-lying isomers with the same structure, although with different spin and interatomic distances. Square pyramid and planar pentagon isomers have smaller cohesive energies. Notice that the ground state of Ni_5 is also a trigonal bipyramid. The ground state of Fe_6 results from capping the trigonal bipyramid. It has a binding energy $E_b = 4.01$ eV/atom and spin $S = 10$. An octahedron with the two apex atoms compressed toward the midplane, also with $S = 10$, is only 0.02 eV/atom higher in energy. Another isomer is a pentagonal pyramid with $E_b = 3.90$ eV/atom. These results suggest that the capped trigonal bipyramid should be investigated for Ni_6. The lowest energy structure of Fe_7 is a pentagonal bipyramid with $S = 11$ and $E_b = 4.37$ eV/atom. Two isomers with $S = 11$ and large binding energies also exist: one is a tetrahedron capped on three of its four faces (incomplete stellated tetrahedron), with $E_b = 4.26$ eV/atom, and the other is a bicapped trigonal bipyramid ($E_b = 4.23$ eV/atom). A capped octahedron lies 0.25 eV/atom above the ground state. The multitude of isomers with energies close to that of the ground state means that those isomers could be present together with the ground state in experiments probing the reactivity or the magnetism of those clusters. A conclusion from the DFT calculations for small Ni and Fe clusters is that compact structures are more stable than open structures. This is good news for methods modeling transition-metal clusters using pairwise or semiempirical many-body interatomic potentials. Spin plays a role in determining the most stable structures. Spin-restricted calculations (neglecting the spin dependence of exchange and correlation) lead to shorter bond lengths. The large spin energies that result from unpaired spins in transition elements often compensate for the lowered occupancy of bonding orbitals that this requires.

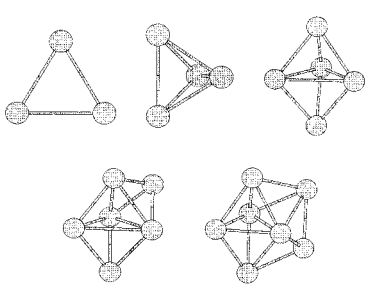

Figure 2. Ground-state structure of small iron clusters predicted by DFT:[84] Fe_3 (C_{3v}), Fe_4 (C_{2v}), Fe_5 (D_{3h}), Fe_6 (C_1), Fe_7 (D_{5h}). Compare with Figure 1 for Ni.

The ground-state structures of small Ni_N and Fe_N clusters of the same size are remarkably similar. The only significant difference occurs for $N = 7$. The pentagonal bipyramid and the capped octahedron are nearly degenerate for Ni_7, while the first structure is significantly more bound than the second one for Fe_7.

C. Niobium Clusters

Nb is a nonmagnetic metal, and Nb clusters are expected to be simpler than Ni or Fe clusters, so it is interesting to compare their geometries. Goodwin and Salahub[87] have performed spin-polarized DFT calculations for clusters containing up to seven atoms

using model core potentials[88] and both LDA and nonlocal GGA (generalized gradient approximation)[89] exchange-correlation functionals. The dimer had a triplet ground state with spectroscopic constants in excellent agreement with other theoretical calculations and in reasonable agreement with the scarce experimental data. The bond dissociation energies are 5.8 (local) and 5.4 eV (nonlocal), and the last one is in better agreement with experiment (5.2 eV). Bond lengths are very similar: 2.08 (local) and 2.10 Å (nonlocal). At the LDA level, Nb_3 is an isosceles triangle, like Ni_3. The symmetry increases by ionization since Nb_3^+ is an equilateral triangle. Nb_4 is compact, a perfect tetrahedron whose bond length simply expands upon ionization. Nb_5 is a trigonal bipyramid, like Ni_5 and Fe_5. Ionization again expands the cluster volume and breaks the symmetry such that only two bonds of the equatorial plane of the bipyramid have the same length. Nb_6 has the form of a planar rhombus with two atoms above the basal plane, aligned along the long diagonal. Finally, Nb_7 is a distorted pentagonal bipyramid. In summary, similarities with the structures of Fe and Ni clusters are found. When the structures of Nb_3-Nb_5 were reoptimized by performing GGA calculations, small changes occurred that changed the bond lengths by several hundredths of an angstrom and lowered the cluster symmetries. The ground-state spin multiplicities were not affected, and the binding energies were reduced by some tenths of an electronvolt, bringing these closer to the experimental values. A break in the slope of the binding energies versus N indicates that Nb_4 is particularly stable, and the same conclusion is obtained from the energy to remove one atom from Nb_N, which has a maximum for Nb_4. The stability of Nb_4 is displayed both by calculated and experimental quantities.

The low energy differences between structural isomers obtained in ab initio calculations introduces small uncertainties in the prediction of the ground-state geometry of small clusters. A reliable determination of cluster structure can be made by comparing the photoelectron spectra, which are structure sensitive, to theoretical predictions for different isomers. In the case of Nb_N^- anions, the measured photoelectron spectra have been compared[90] to calculated spectra for $N = 3-8$ using the LSDA approximation. The binding energies of the electrons in the cluster were calculated in two steps. First these binding energies were approximated by a generalized transition-state theory[91]

$$D_i^{\mathrm{GTS}} = -[\epsilon_i(1) + 3\epsilon_i(1/3)]/4 \qquad (12)$$

where $\epsilon_i(\nu)$ is the energy eigenvalue of orbital ϕ_i obtained in a self-consistent calculation with the occupation number n_i fixed equal to ν. This formula can be viewed as an approximation to the ΔSCF method, which evaluates the energy difference between the anion ground state and an excited electronic configuration of the neutral. For the particular case of the lowest bound electron, the binding energy, which is the electron affinity, can be obtained rigorously in a different way, namely, by subtracting the ground-state energy of the neutral cluster at the anion equilibrium geometry from that of the anion. Denoting this result D_a^{SCF}, then all the binding energies from eq 12 were shifted by

$$\Delta = D_a^{\mathrm{SCF}} - D_a^{\mathrm{GTS}} \qquad (13)$$

with typical values of this shift being $\Delta = 1.25$ eV. A number of isomers were obtained by starting with many trial geometries, and the ground state had a structure almost identical to that for neutral Nb_N, $N = 3-7$. Then, for the ground state and all other isomers, the excitation spectra were calculated according to eqs 12 and 13 and compared to the measured spectra. In general, the calculated lowest energy structure produces an excitation spectrum in substantially better agreement with experiment than the spectra from other isomers, although the agreement is far from perfect since the treatment of excited states embodied in eqs 12 and 13 is too simple. Only in two cases was the experimental spectrum assigned to a low-lying isomer: for Nb_3^- to an isosceles triangle (instead of the equilateral triangle) and for Nb_5^- to a distorted trigonal bipyramid (instead of an ideal one). But in both cases the energy difference between those isomers and the ground state is small. Evidence was also found for the coexistence of two isomers of Nb_8^- under some experimental conditions. Fournier et al.[92] have made a more exhaustive study by testing other simple methods to take into account final state effects in the calculation of the electron binding energies.

The ionization potentials[93] and the measured photoelectron spectra of Nb_N^- have also been employed to establish a correlation between electronic structure and reactivity.[94] The reactivities of neutral Nb_N clusters with H_2 show a simple pattern: Nb_8, Nb_{10}, and Nb_{16} are relatively unreactive while the other clusters readily chemisorb hydrogen. From the measured photoelectron spectra of Nb_N^-, Kietzmann et al.[94] determined the vertical detachment energies (VDE), approximately equal to the electron affinities of the neutrals. An even−odd alternation was observed for sizes $N = 6-17$, with high VDEs for odd N and low VDEs for even N, and especially pronounced minima for $N = 8$ and 10. For $N > 16$, the VDEs increase steeply with no even−odd alternation. Even−odd alternation is usually observed in clusters of simple metals with an odd number of electrons per atom, and it means that the highest single-particle level is nondegenerate and occupied by one or two electrons. The free Nb atom has five valence electrons in the electronic configuration $4d^45s^1$. The even−odd alternation indicates that the even numbered neutral clusters (Nb_8, Nb_{10}, Nb_{12}, Nb_{14}, Nb_{16}) have a closed HOMO level and that the additional electron occupies the LUMO, giving rise to a small peak at low binding energy in the experimental PES spectrum. Instead, when the HOMO is half-occupied (odd N), the extra electron fills the HOMO and results in a high VDE for the corresponding Nb_N^- clusters.

If the neutral cluster has closed electronic levels, the HOMO−LUMO gap can be measured directly in the photoelectron spectrum. Large HOMO−LUMO

gaps were found for $N = 8$, 10, 16, consistent with the pronounced local minima in the affinities. All the features discussed above correlate precisely with the measured reactivities with H_2: the clusters with the largest gaps ($N = 8$, 10, 16) have the lowest reactivities. The reactivity of Nb_{10} with CO is also abnormally small compared to other Nb clusters.[95] In fact, the relation of large gaps to low reactivities can be achieved through the chemical index "hardness":[96] a "hard" cluster or molecule should be unreactive. A measure of the hardness of a cluster is given by[97]

$$\eta = \mathrm{I} - \mathrm{EA} \tag{14}$$

the difference between the ionization potential I and the electron affinity EA, and this difference is the HOMO−LUMO gap. Nb_{15}^- has a peculiar photoelectron spectrum, very different from neighbor sizes. This, plus the fact that the VDE increases steadily and without odd−even oscillations for $N > 16$, was interpreted by Kietzmann et al. as a possible indication of geometrical shell closing at $N = 15$ (perhaps a piece of bcc bulk formed by two coordination shells around a central Nb atom). The evidence for this early transition to the bulk structure is not too strong, and theoretical calculations should be performed to test this interpretation.

D. Titanium and Vanadium Clusters

The electronic structure of titanium clusters has been studied using photoelectron spectroscopy of size-selected cluster anions[98] at photon energies of 3.49 and 4.66 eV. The outer electrons of the free Ti atom are in a configuration $3d^2\ 4s^2$. With only two d electrons, the electronic structure of the clusters is expected to be simpler than that for elements in the middle or in the second half of the 3d series. Discrete spectral features are only observed for Ti_N^- with $N \leq 8$. In this range of very small cluster sizes, the photoelectron spectrum changes from N to $N + 1$, reflecting their molecular nature. Starting with Ti_8^-, the spectrum becomes simple. No sharp features appear beyond this size; instead, a prominent feature appears near the detachment threshold whose width increases with N. The width is about 1 eV in the range Ti_{20}^-−Ti_{50}^-. This broad feature is similar to the single broad feature in the valence photoemission spectrum of the bulk metal, which has a width of about 2 eV and is due to the 3d band.[99,100] The detachment threshold, which gives the electron affinity of the neutral cluster, displays an even−odd oscillation below Ti_8^- and a monotonic increase for N larger than 8. For N larger than ~30, the affinities are fitted well by the relation

$$\mathrm{EA} = \mathrm{WF} - \frac{5e^2}{8R} \tag{15}$$

where WF is the bulk work function and R is the cluster radius. R was estimated as $R = r_c N^{1/3}$ with $r_c = 2.49$ au. This value of r_c is smaller than the usual metallic radius in the bulk and can simulate the contraction of interatomic distances in small clusters. The relation of eq 15 itself shows that the convergence of EA to the bulk is not fast; for instance WF = 4.33 eV, whereas $EA(Ti_{64}) = 2.6$ eV. The evolution of the shape of the photoelectron spectrum was interpreted by Wu et al.[98] as an early metallization of the clusters, perhaps due to close-packed structures. A pronounced narrowing of the PES feature occurs for Ti_{55}^-. This and the results for the dissociation energies of small Ti_N^+ clusters[101] suggest that some of those clusters could be icosahedral.

The electronic configuration of atomic vanadium is $3d^3 4s^2$, with one d electron more than Ti. The PES spectra, measured by Wu et al.[102] for V_N^-, $N \leq 65$, at a photon energy of 4.66 eV, are more interesting compared to Ti_N^-. The clusters can be separated in four size regions. Up to V_{12}^- the spectrum is molecular-like, with a number of discrete well-resolved features. V_{13}^-−V_{16}^- form a transition region from discrete spectra to a two-band spectra. For V_{17}^- the first of those two features is narrow and peaks at 2 eV (near threshold) and the second band is broad and centered at a binding energy of about 3.2 eV. Between V_{17}^- and V_{60}^- the two features converge to a single broad feature, and finally, for $N > 60$ the PES changes very little with N. PES spectra were also recorded at a higher photon energy of 6.42 eV, and a new broad peak appears for V_{17}^- and larger clusters at a binding energy of 5.2 eV, of course inaccessible to the previous photon energy of 4.66 eV. Wu et al.[102] have correlated this feature and the other broad feature near 3.2 eV with similar broad features observed in the PES spectra of bulk vanadium.[103] Wu et al.[102] proposed that these bulklike effects have their origin in the inner region of the clusters, suggesting that the clusters may already have structures similar to the bulk crystal lattice. Consequently, they interpret the sharper peak that emerges from V_{13}^- and gradually merges with the broad peak as due to the cluster surface. This interpretation suggests that starting from V_{13} the cluster already has surface and inner parts and starting from V_{17} the inner region has some similarity with the bulk. The sharp peak is most likely due to states derived from the s atomic orbitals and the broad feature due to the d states. As the cluster size grows, the d band widens and the two features merge: the density of states of bulk vanadium near the Fermi level is mostly of d character.[61] In contrast to titanium, the EAs of very small vanadium clusters do not show odd−even effects. EA has local minima for V_5 and V_{12} and maxima for V_4 and V_{10}. The affinities become smooth for $N \geq 17$ and are fitted extremely well by the metallic drop model of eq 15. Iseda et al.[104] extended the photoelectron measurements for vanadium cluster anions up to $N = 100$.

Minemoto et al.[105] have studied the electronic structure of V_4^+ by optical absorption spectroscopy. Using a technique developed by Knickelbein[106] and Collings et al.,[107] the experiment measures the intensity depletion of the complex V_4^+ Ar against the wavelength of the irradiation laser. The spectrum thus obtained is treated as the optical absorption spectrum of the underlying cluster V_4^+ because the rare gas atom is weakly attached and does not significantly affect the geometry and the electronic structure of V_4^+. The measured spectrum was simu-

lated by calculations based on DFT with the LSDA approximation. The transition energies between the ground state and the excited states concerned were computed by the transition-state method of Slater.[108] The intensity of a given absorption transition was obtained from its oscillator strength, calculated from the transition-dipole matrix element between the initial and final one-electron wave functions. Finally, the absorption spectrum was constructed by superimposing all the transitions widened with a Lorentzian profile. Several plausible geometrical structures were examined: a distorted tetrahedral structure with C_{2v} symmetry, a tetrahedron (T_d), a rhombus (D_{4h}), and a parallelogram (D_{2h}) of varying bond lengths, and only the first one is able to reproduce the experimental spectrum reasonably, although not perfectly. An extensive check for the lowest energy structure of V_4^+ with the ADF code[109] (this is a DFT code) confirmed that the C_{2v} structure is the ground-state isomer. The relatively broad widths (0.2 eV) of the measured absorption peaks were assigned to vibrations related to a specific deformation coordinate that connects the C_{2v} and T_d structures.

E. Chromium Clusters

Small chromium clusters show peculiarities that make them special compared to other 3d clusters. The free atom has the electronic structure $3d^5 4s^1$ with six unpaired valence electrons. This half-filled electronic configuration leads to strong d−d bonding in Cr_2 with an unusually short bond length: 1.68 Å,[110−112] compared to 2.50 Å in the bcc solid.[60] Such a short bond length was first measured in a flash photolysis experiment.[110] DFT calculations by Cheng and Wang[113] show that this dimer is a closed-shell system with a strong sextuple bond. The strong bonding arises from the filling up of the 3d-bonding molecular orbitals: $\sigma_{3d}^2\pi_{3d}^4\delta_{3d}^4\sigma_{4s}^2\ {}^1\Sigma_g^+$. This electronic structure is very robust and controls the growth of small Cr_N clusters, as concluded by Cheng and Wang who have performed calculations for clusters up to $N = 15$. The geometries were fully optimized from Cr_3 to Cr_{12}, and for reasons given below, the structures of Cr_{13}−Cr_{15} were restricted to be fragments of a bcc lattice. The structures up to Cr_{11} are given in the insets in Figure 3. Cr_3 is composed of a dimer plus an atom: the electronic structure of the dimer is virtually unchanged and the third atom surprisingly remains in its atomic electronic state leaving six unpaired electrons in the cluster. This view is confirmed by the charge density plots. An additional atom pairs up with the third one, and Cr_4 is formed by two dimers with strong internal bonds and weak interdimer bonding. The dimerization effect controls the growth of Cr_N up to $N = 11$: all those clusters are formed by Cr_2 dimers with a short bond length and one (in Cr_5, Cr_7, Cr_9) or two (in Cr_{10}) isolated atoms bonded to adjacent dimers. The strong bonds in the dimers are indicated by the heavy lines in Figure 3. Cr_{11} has a structure similar to that of Cr_{10} with a third isolated atom at the cluster center. The presence of this inner atom increases the interdimer distances while the dimer bond length in fact decreases. Charge density plots again substantiate the

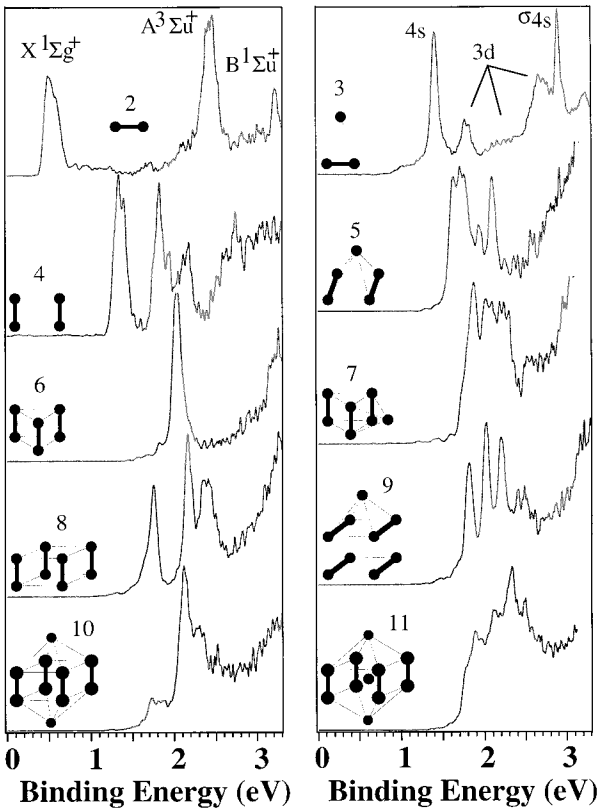

Figure 3. Photoelectron spectra of Cr_N^-, $N = 2$−11 at 3.49 eV photon energy. The structure of each cluster is included.[115] (Reprinted with permission from ref 115. Copyright 1997 American Institute of Physics).

picture of a dimer route of growth. This growth route stops precisely at Cr_{12}. The structure of Cr_{12} is superficially similar to that of Cr_{11}: just an additional atom caps one of the lateral faces of Cr_{11}. However, the Cr−Cr distances in the dimers suddenly become large and the dimerization effect vanishes, that is, dimer-like bonds cannot be identified any more in clusters with $N > 11$. Cr_{12} remains a small fragment of a bcc solid (Cr_{11} with its inner atom also does, but dimerization is still active in this cluster), and for this reason the structures studied by Cheng and Wang for $N \geq 13$ were bcc fragments obtained by capping additional lateral faces of Cr_{11}. In summary, the structures are controlled by intradimer and interdimer interactions. For the smaller clusters the intradimer interaction dominates. The interdimer interaction becomes stronger as the cluster size increases, leading to the transition from dimer growth to bcc-like structures.

The dimer growth route implies an odd−even effect in the properties of Cr_N clusters. Indeed, an even−odd alternation in the magnitude of the dissociation energies has been observed for $N < 10$.[114] Odd−even effects have also been observed by Wang et al.[115] in the photoelectron spectrum of Cr_N^- clusters. The measured PES are reproduced in Figure 3 for $N = 3$−11. These spectra are characterized for having several discrete features: clusters with even N have fewer features near the threshold and a distinct gap, and clusters with odd N show more complex spectra with congested features near the threshold, in particular for $N = 5, 7, 11$. The even−odd alternation

disappears above Cr_{12}^- (see Figure 2 of Wang[115]): a sharp threshold feature is observed in that size range that evolves toward high binding energies and overlaps with other higher binding energy features as the cluster size increases. The odd−even alternation for small N is clearly seen in the measured electron affinity.[115]

The closed-shell electronic structure of Cr_2 produces a large gap between the HOMO−σ_{4s} and LUMO−σ_{4s}*, as seen in the spectrum of Cr_2^- in Figure 3: the two prominent peaks, labeled X and A in this figure, correspond to the removal of one electron from the σ_{4s}* and σ_{4s} levels, respectively. A vibrationally resolved PES spectrum of Cr_2^- has been obtained for the X and A states.[116] As indicated above the electronic structure of Cr_3 can be described as $(\sigma_{3d}^2\pi_{3d}^4\delta_{3d}^4\sigma_{4s}^2)3d^54s^1$, that is with the third atom in its atomic configuration having all its six electrons unpaired. The orbital degeneracy is lifted under the C_{2v} symmetry of Cr_3, so the 3d orbitals of the odd atom are split into five nondegenerate orbitals. The 4s orbital of the odd atom (weakly mixed with the σ_{4s} orbital of the dimer) becomes the HOMO of Cr_3 and the extra electron in Cr_3^- fills this level. The first feature in the PES spectrum of Cr_3^- at 1.4 eV (see Figure 3) corresponds to the removal of an electron from the atomic 4s orbital. The prominent peak at 2.9 eV arises from the removal of an electron from the σ_{4s} orbital of the dimer. This orbital has a larger binding energy than the corresponding σ_{4s} orbital in Cr_2 because of its interaction with the 4s orbital of the odd atom. All the features between the 4s and σ_{4s} peaks are due to the 3d electrons of the odd atom. For this reason, the PES spectrum of Cr_3^- is more congested than that of Cr_2^-. It should be noticed that all the features ascribed to the odd atom in Cr_3 fall inside the region of the HOMO−LUMO gap of Cr_2. The spectra of Cr_4^- and Cr_8^- show gaps of 0.48 and 0.41 eV, respectively, suggesting that the neutrals have closed shells. The spectrum of Cr_6^- is unusual, with an intense threshold peak and a high electron affinity. All these features are explained by the DFT calculations, confirming that Cr_4 and Cr_8 are closed-shell clusters. On the other hand, Cr_6 has an open-shell configuration and the extra electron in the anion enters into the partially filled HOMO, in contrast to Cr_4^- and Cr_8^-, where the extra electron goes to the LUMO of the neutrals. This results in the high electron affinity of Cr_6 compared to Cr_4 and Cr_8.

The electronic structure of the odd clusters from Cr_5 to Cr_9 can be described, as for Cr_3, as arising from the interaction between the levels of the even cluster $(N - 1)$ and the odd atom: the energy levels of the odd atom are bunched near the HOMO and in the region of the HOMO−LUMO gap of the even cluster. The larger electron affinities of the odd clusters compared to the even ones occur again because the extra electron goes to the open-shell HOMO in the odd clusters. Cr_{10} and Cr_{11} deviate slightly from the dimer growth route since they have four dimers instead of five. Still, their PES spectra resemble those of the even and odd clusters, respectively. Finally, the measured PES spectra of Cr_{12}−Cr_{15} show that the even−odd alternation effects vanish in agreement with the theoretical prediction[113] that the dimer growth effect also terminates. All the PES of large clusters have similarities, with a sharp feature near threshold that smoothly merges with other higher binding energy features as N increases. Beyond Cr_{24} a single broad band is observed near threshold (in experiments at 3.49 and 4.66 eV photon energies). In this size range the PES spectrum already resembles the first bulk feature where a sharp peak near the Fermi level is followed by a broad surface feature.[117,118] Further similarities appear at higher binding energy for experiments performed at 6.42 eV photon energy. To close, we stress that the odd−even alternation effects observed for Cr clusters have a different nature compared to those observed for alkali- and noble-metal clusters and explained by the ellipsoidal jellium model.

For many years the Cr_2 molecule has represented the benchmark test for a proper account of correlation effects in ab initio calculations. The most recent ab initio calculations reproduce the bond distance well, although the binding energy is still difficult to calculate accurately. The DFT calculation of Cheng and Wang,[113] which used the LDA for exchange and correlation, obtained a bond length of 1.69 Å and a binding energy of 2.28 eV, to be compared with experimental values of 1.68 Å and 1.50 eV, respectively. The overestimation of the binding energy reflects the effect of the LDA. A multireference CI calculation including almost 1.3 billion configurations[119] gives a bond length of 1.72 Å and a binding energy of 1.09 eV. The same paper also gives an extensive review of previous calculations for Cr_2. Most recently, an ab initio calculation by J. Persson and P. R. Taylor, referred to in a review by Roos,[120] gives very accurate values for both magnitudes, 1.695 Å and 1.628 eV respectively, so it seems that the quest for a correct description of Cr_2 is coming to an end.

V. Thermionic Emission from Refractory Metal Clusters

The photoelectron spectra of some 3d and 4d cluster anions have been discussed above. The physical process underlying the PES spectra is the following

$$M_N^- + \hbar\omega \rightarrow M_N + e^- \quad (16)$$

$$\rightarrow M_N^* + e^- \quad (17)$$

that is, the absorption by a cluster anion M_N^- of a photon of energy $\hbar\omega$ larger than the electron affinity of the neutral M_N leads to the prompt emission of an electron on a time range of or below femtoseconds, leaving the neutral cluster in its ground state M_N or in an excited state M_N*. The kinetic energy E_{kin} of the electron is different if the final state of the neutral cluster is M_N or M_N*. But this is not the only possible process. The absorbed energy can be rapidly thermalized by the internal degrees of freedom of the cluster anion, which then reaches a superheated state $(M_N^-)_{E_1}$ with internal energy E_1, and subsequently

the hot cluster anion can emit an electron, leaving the neutral cluster in a state with lower internal energy E_2. This process is, schematically

$$M_N^- + \hbar\omega \rightarrow (M_N^-)_{E_1} \rightarrow (M_N)_{E_2} + e^- \quad (18)$$

It takes time to focus the energy back into the electron emission channel, so the emission of the electron by this process is delayed in time compared to the direct photoemission. Another difference between the two processes is that direct photoemission leads to a discrete spectrum while in delayed photoemission, which is related to the well-known thermionic emission of electrons from hot metal surfaces,[121] the emitted electrons exhibit a quasicontinuous energy distribution. The spectrum of kinetic energies is a smooth exponential function corresponding to a "temperature" $T = (E_1/k_B)(3N - 6)$ where E_1 is the excitation energy (energy of the photon), k_B is Boltzmann constant, and $3N - 6$ is the number of vibrational degrees of freedom.

Delayed ionization (lifetimes greater than 10^{-7} s) was first observed in neutral clusters of refractory metals (W, Nb, Ta).[122−124] A detailed study has been performed for W_N^- to analyze the contributions from prompt and delayed ionization.[125] Starting from W_2^-, the PES spectrum shows sharp peaks at low binding energies (between 1.5 and 2.5 eV) assigned to direct photoemission and a smooth thermionic signal that increases monotonically with increasing binding energy. The overlap region between the two components of the spectrum goes from 2.5 to 3 eV. The two components are also observed for larger clusters. The sharp peaks arise from direct photoemission from occupied 5d- and 6s-derived molecular orbitals of the clusters. The smooth signal is fitted very well by a Boltzmann distribution for the intensity

$$I = A \exp(-E_{kin}/k_B T) \quad (19)$$

where the temperature corresponds to a photon energy $\hbar\omega = 4.025$ eV used in the experiments. Evidently, when the time constant of the thermionic emission (TE) is much longer than the time scale of the experiment (usually around 0.1 μs) only direct photoemission would be observed. This is the reason the integrated TE intensity decreases with increasing N for W_N^-: as the number of degrees of freedom increases, the photon energy is distributed over a larger number of vibrational modes and it takes longer to focus the energy back into the electron emission channel.

Before the observation of thermionic emission from hot tungsten clusters, the standard cooling mechanism detected for different types of superheated clusters had been the evaporation of neutral fragments (mostly monomers)

$$M_N^- + \hbar\omega \rightarrow (M_N^-)_{E_1} \rightarrow (M_{N-1}^-)_{E_2} + M_1 \quad (20)$$

The faster of the two cooling mechanisms, delayed ionization or fragmentation, is going to dominate, and the time constants depend on the respective energy thresholds: these are the electron affinity in the case of TE and the binding energy of the atom for the evaporative cooling. For the refractory metal clusters the threshold for evaporation is larger than the electron affinity (3−4 times larger in W_N) and TE dominates, as observed in the experiment. This can already be predicted from the properties of the bulk metals: a small ratio between the work function WF and the cohesive energy per atom E_c and a small value of WF in absolute terms are the conditions for good thermionic emitters, and these conditions are best satisfied by the refractory metals; in particular, the ratio is 0.5 for tungsten. This is, in fact, the reason the cluster experiments focused on these elements. In contrast, when the magnitudes of the electron affinity and the evaporation energy are similar, the two cooling mechanisms are competitive. This is the case for alkali cluster anions: Reiners and Haberland[126] have observed atom and electron emission from Na_{91}^-. For neutral or positively charged clusters of most metals, the cooling mechanism is atom evaporation since in this case the ionization potential (which substitutes the electron affinity) is usually larger than the binding energy of an atom, even for the simple sp metal clusters. By storing the W_N^- anions in a Penning trap, Weidele et al.[127] have observed delayed electron emission on the millisecond time scale.

Delayed ionization attributed to a thermionic emission process is not specific of pure refractory metal clusters and also has been observed for metal carbide clusters,[128] metal oxide Nb_nO_m clusters,[129,130] and metallocarbohedrene clusters Ti_8C_{12} and V_8C_{12} by Castleman and co-workers.[131,132]

VI. Nonmetal–Metal Transition

The theoretical characterization of what is a metallic material is clear in the case of bulk systems, where band theory concepts apply. This concept is more subtle for small clusters. Very small clusters can be considered nonmetallic, having a discrete distribution of electronic states, and a critical size N_c is required before this distribution turns into a quasicontinuous one in the region around the Fermi level.[133] The static electric polarizability α of alkali clusters (or more properly, the $w \rightarrow 0$ limit of the dynamic polarizability) rapidly drops from large values for the free atoms toward much lower values characteristic of a conducting metallic sphere, $\alpha = R^3$, where R is the radius of the sphere. The measured polarizabilities of lithium clusters[134] reveal that the electronic delocalization already appears for sizes as small as Li_4 or Li_5. The polarizabilities of transition-metal clusters have not been measured. Scanning tunneling spectroscopy experiments of deposited clusters measure their conductance and are able to shed light on their electrical character. These experiments have been performed for some transition- and noble-metal clusters[135−137] and essentially probe the density of states at the Fermi level ϵ_F. The tunneling conductance decreases markedly with a decrease of the cluster size, when the cluster diameter is < 1 nm and shows the emergence of an energy gap, suggesting that small clusters are indeed nonmetallic. Kubo[138]

has proposed that a cluster has metallic character when the average level spacing becomes smaller than the thermal energy k_BT, or in terms of the density of states (DOS) $D(\epsilon)$, when

$$D(\epsilon_F) \geq \frac{1}{k_BT} \tag{21}$$

The simple square d-band model introduced by Friedel[139] within a tight-binding framework can be extended to clusters, and the DOS can be expressed (the model neglects sp electrons)

$$D(\epsilon) = \begin{cases} \dfrac{10N}{W(N)} & \text{for } -\dfrac{W(N)}{2} \leq \epsilon - \epsilon_d \leq \dfrac{W(N)}{2} \\ 0, & \text{otherwise} \end{cases} \tag{22}$$

Here the factor 10 is the total number of electrons in a full d shell and ϵ_d is the atomic d level. The bandwidth $W(N)$ can be related to the average atomic coordination $Z(N)$ using a second moment approximation[140]

$$W(N) = W_b(Z(N)/Z_b)^{1/2} \tag{23}$$

where W_b and Z_b are the bandwidth and coordination number in the bulk, respectively. Using the last two equations, relation 21 can be written

$$\frac{10N}{W_b}\left(\frac{Z_b}{Z(N)}\right)^{1/2} \geq \frac{1}{k_BT} \tag{24}$$

This relation shows that for a given metal, the critical size N_c is determined by the variation of the function $Z(N)$. Zhao et al.[141] have used a simple approximation

$$Z(N) = \frac{Z_b(N-1)}{Z_b + (N-1)} \tag{25}$$

that leads, from eq 24, to the approximate solution

$$N_c = [12G(T) + 171]^{1/2} - 6 \tag{26}$$

where $G(T)$ is defined $G(T) = (1/k_BT \cdot W_b/10Z_b)^2$. Taking $Z_b = 12$, the value for an fcc crystal, and using bandwidths from Harrison,[10] the following values are obtained for a temperature $T = 120$ K: $N_c(Fe) = 50$, $N_c(Co) = 39$, $N_c(Ni) = 34$, $N_c(Pd) = 50$.

The approximation for $Z(N)$ in eq 25 depends only on N and takes no account of the cluster geometry. For instance, for an fcc cluster with 55 atoms and a cuboctahedral shape, the average coordination given by eq 25 is 25% too high compared to the exact value 7.85. Furthermore, if the cluster grows by the formation of successive atomic shells, $Z(N)$ should show a nonmonotonic behavior. Aguilera-Granja et al.[142] have evaluated $Z(N)$ exactly for Co, Ni, and Pd clusters with two structural types: (a) particles with an underlying fcc lattice and cuboctahedral (CO) shape and (b) icosahedral particles. In both cases the critical sizes for $T = 110$ *K* are $N_c(Co) = 31$, $N_c(Ni) = 27$, $N_c(Pd) = 43$, a little smaller than the values obtained using eq 25. For Fe clusters with an underlying bcc lattice and (a) spherical or (b) cube shapes, the critical sizes for $T = 110$ K are $N_c(Fe) = 33$ and $N_c(Fe) = 35$, respectively, again smaller than the value from eq 25. Tunneling experiments probing the density of states at the Fermi level have been performed for Fe clusters supported on a GaAs substrate at room temperature.[135] These experiments indicate that the nonmetal−metal transition occurs for $N_c \simeq 35$. The values obtained by Aguilera-Granja et al. are consistent with this value. For Pd clusters, X-ray spectroscopy indicates that the nonmetal−metal transition occurs for cluster radii in the range 7−10 Å,[143] while the theoretical model predicts a size range 5−8 Å (40−120 atoms) depending on the temperature.

N_c can also be estimated from an analysis of the ionization potential. For a metallic droplet electrostatic arguments predict that I varies as

$$I(R) = WF + (3/8)R^{-1} \tag{27}$$

as a function of cluster radius R; or in terms of N

$$I(N) = WF + \alpha N^{-1/3} \tag{28}$$

where α is a material dependent constant. In practice, the ionization potential follows this relation rather well except for small sizes and N_c can be identified with that cluster size when the measurements begin to deviate from expression 28. Using ionization potentials measured by Parks et al.,[144] one obtains $N_c(Fe) \simeq 28$, $N_c(Ni) \simeq 20$, $N_c(Co) \simeq 17$. The estimated cluster temperatures in those measurements are 225 ± 50 K, and for those temperatures Aguilera-Granja et al. obtained from eq 24 $N_c(Fe) \simeq 18-21$, $N_c(Ni) \simeq 14$, $N_c(Co) \simeq 15$. The comparison is satisfactory considering the approximations in the square band model and the errors made in determining N_c from measured ionization potentials.

The theoretical model can be improved if the square d-band model is replaced by a full tight-binding calculation without any assumptions about the shape of the band. Aguilera-Granja et al.[145] have solved self-consistently a tight-binding Hamiltonian for the 3d and 4sp electrons of Ni clusters in a mean-field approximation. The full details of this Hamiltonian will be presented below when discussing magnetic properties (section IX). Here we only give the results of the application to the nonmetal−metal transition of Ni clusters. The density of states $D(\epsilon)$ was calculated for a number of Ni clusters. The geometries of these were obtained by molecular dynamics simulations using an interatomic many-body potential[146] for $N \leq 14$. For larger clusters, the geometries correspond to a model of icosahedral growth (see section VII) and were optimized with the same potential. Using the Kubo criterion of eq 21, the phase diagram of Figure 4 was constructed. The triangles delineate a boundary that separates the regions of nonmetallic and metallic character. The boundary is smooth for $N \geq 14$. However, it becomes steep and irregular for lower sizes. This suggests a possible sensitivity to the cluster geometries used to obtain the DOS. To investigate this point, the figure also contains a number of open squares. These represent results obtained using other geometries. The conclusion is that the phase boundary is not very

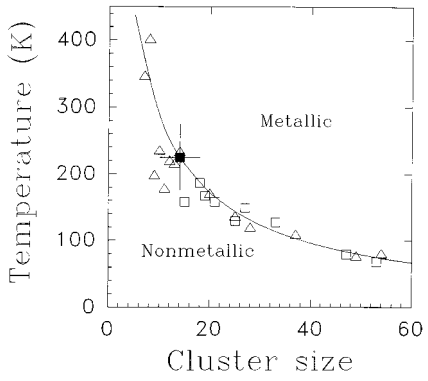

Figure 4. Calculated nonmetal−metal phase diagram of Ni clusters. The continuous line corresponds to a simple rectangular d-band model, while the squares and triangles give the boundary obtained from fully self-consistent tight-binding calculations. The filled square is an experimental point obtained from measurements of the ionization potential.

sensitive to the cluster geometries as long as these are chosen in a reasonable way. The filled square (with error bars) represents an experimental point of the boundary, estimated from the measurement of ionization potentials. This experimental point fits well in the predicted boundary.

The rectangular d-band model leads to a phase boundary, the continuous curve in the figure, that reproduces rather accurately the results of the full TB calculation. This is because the square d-band model gives a remarkably good estimation of $D(\epsilon_F)$ as compared to the full TB-*DOS*. Despite this rather lucky agreement, the full *TB* calculation shows that the shape of the *DOS* deviates strongly from a rectangular shape for small Ni clusters.

VII. Icosahedral Model for Nickel Clusters of Medium Size and Its Relation to Reactivity Experiments

The determination of the geometrical arrangement of the atoms in clusters of medium size, either from theoretical calculations or from experimental methods, becomes a very difficult task. There is some evidence that in a certain range of cluster sizes, icosahedral arrangements compete successfully and become favored over other arrangements based on the underlying lattice of the bulk crystal. The rare-gas clusters were the first to show icosahedral symmetry.[147] Not only perfect icosahedra with complete shells were identified, but also a picture of icosahedral growth was derived.[148] For many metal clusters, the mass spectrum for sizes higher than a critical size (which is very dependent on the particular metal) has been interpreted as reflecting the formation of geometrical (or atomic) shells. That critical size is about 1500 atoms for Na.[149] Thus, between $N_c \simeq 1500-22\,000$ (the largest clusters produced in the experiments), the structure of the mass spectrum is consistent with the formation of icosahedra or fcc-cuboctahedra. For alkaline-earth metals, icosahedral clusters occur for smaller sizes: Ba clusters with N between 13 and 55 atoms[150,151] and Mg clusters with N larger than 147 atoms[152] appear to have icosahedral structure. Information about the development of the icosahedral shells was extracted in the last case and a model of growth was proposed. This growth path, although related to the one accepted for rare-gas clusters, is not identical and does not produce the same magic numbers (the way of covering an icosahedral cluster to obtain a larger icosahedron is not unique).

Pellarin et al.[153] have analyzed the mass spectrum of Ni and Co clusters containing between 100 and 800 atoms. The spectra were measured by performing near-threshold photoionization and standard time-of-flight mass spectrometry. Highly stable clusters of size N_m have larger ionization potentials compared to neighbor clusters of sizes $N_m + 1$, $N_m + 2$, ... When the photon energy $\hbar\omega$ is lowered just below the ionization potential $I(N_m)$ of the cluster of size N_m, only the clusters of sizes $N_m + 1$, $N_m + 2$, ... in the molecular beam will be detected in the mass spectrum, but not the size N_m. This provides a very efficient method of analyzing the variations in stability of clusters as a function of size.[154] For nickel clusters, a sharp increase in the abundance was observed at some particular cluster sizes. The strongest effects occur after $N_m = 55$, 147, 309, and 561. These highly stable clusters could, in principle, correspond to complete icosahedra or cuboctahedra. Additional evidence for icosahedra instead of cuboctahedra comes from the fact that above $N = 200$, enhanced stability was observed every time a face of an icosahedron was covered in the process of building the next icosahedron. Chemical probe experiments by Riley and co-workers[74,155−159] point to icosahedral symmetry of Ni clusters in some size ranges (the results will be discussed below). This conclusion is derived from the measured saturation coverages and adsorption free energies of H_2O, NH_3, and especially N_2 molecules.

The experimental inferences have prompted a detailed study of a growth model based on the formation of icosahedra with an increasing number of shells,[160] and this is the only model that has been confronted in great detail with the reactivity experiments. A perfect icosahedron is formed by 20 triangular faces joined by 30 edges and 12 vertices. The smallest perfect icosahedron can be labeled Ico_{13}. The icosahedral structure of Ni_{13} is supported by ab initio DFT calculations.[79] In this cluster, one atom occupies the central position and the other 12 atoms occupy the 12 vertices. Atoms can be added on top of this icosahedral core in two ways. In the first type of covering (labeled MIC) atoms are added on top of edge (E) and vertex (V) positions. These provide a total of 42 sites (30 + 12) to cover Ico_{13}, and this way Ico_{55} is obtained. Alternatively, instead of the E sites one can cover sites at the center of each triangular face (T sites), a total of 20. In this way the covering of Ico_{13} by 32 atoms (12 + 20) leads to a cluster of 45 atoms. This second type of covering is often labeled TIC. In a similar way, if we start with Ico_{55}, its covering can be performed in the MIC mode, producing Ico_{147}: covering the 12 vertex sites, placing two atoms on top of each edge (sites E_1 and E_2) to give a total of 60 E atoms and one atom (on a T site) above the center of each of the 20 faces. As before, a TIC

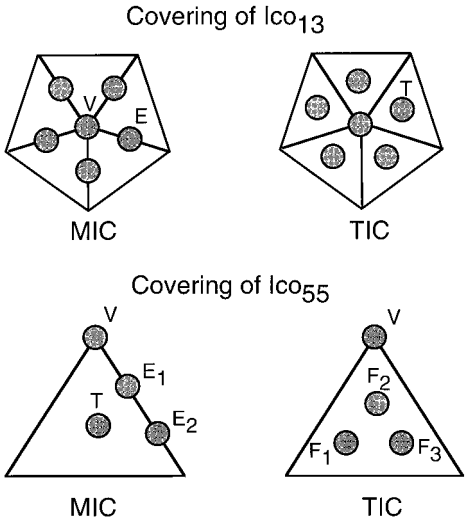

Figure 5. MIC and TIC coverings of icosahedral clusters.

covering can be effected instead: filling the 12 vertex sites and covering each triangular face with three atoms, a cluster with 127 atoms is obtained. Figure 5 shows the two types of covering for Ico_{13} and Ico_{55}. In ideal MIC covering there are two first-neighbor distances of 1.0 and 1.05 (short bonds), in units of the radius of Ico_{13}, and a second-neighbor distances of 1.45. The distance 1.0 corresponds to first neighbors in different shells, and the distance 1.05 to first neighbors in the same shell. For ideal TIC covering, there are more bond lengths of value 1.0 than in MIC but some of the bond lengths of magnitude 1.05 are replaced by larger ones with values 1.13 and 1.21 (the density of surface atoms of the TIC cluster is lower). The TIC growth is favorable at the beginning of a shell up to a point when the MIC growth becomes preferred. This is understandable, because the atoms added give rise to more short bonds in the TIC mode at the initial steps of covering and in the MIC mode beyond a certain size. The crossing point depends on the details of the interatomic interactions so that different systems have different crossing points.[148,161]

The competition between TIC and MIC geometries has been studied[160] by modeling the interatomic interactions by the embedded-atom method (EAM).[162,163] The binding energy of the cluster is given in this method as

$$E_b = \sum_i F_i(\rho_i^h) + \frac{1}{2}\sum_{i\neq j}\phi_{ij}(r_{ij}) \qquad (29)$$

Each contribution $F_i(\rho_i^h)$ represents the embedding energy of atom i in an effective uniform medium whose density ρ_i^h is approximated by the superposition of the atomic density tails of the other atoms around site i. On the other hand, $\phi_{ij}(r_{ij})$ is a residual core−core repulsion between atoms i and j separated by a distance r_{ij} that Foiles et al.[162] parametrized in the form

$$\phi_{ij}(r) = \frac{Z_o^2(1+\beta r^\nu)^2 e^{-2\alpha r}}{r} \qquad (30)$$

where Z_o is the number of outer electrons of the atom

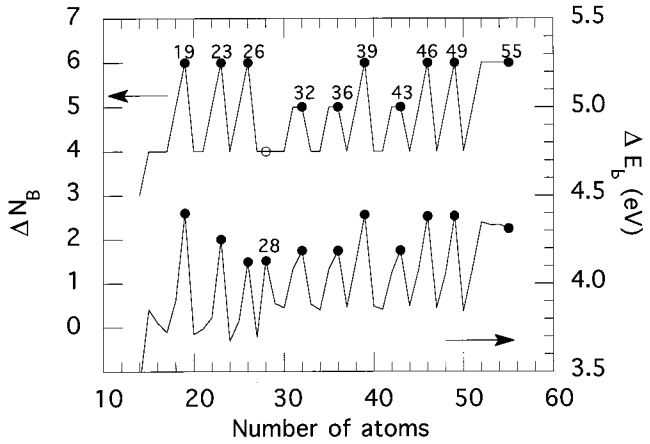

Figure 6. Binding energy difference $\Delta E_b = E_b(N-1) - E_b(N)$ and change ΔN_B in the number of bonds between Ni_{N-1} and Ni_N versus the number of atoms N. The numbers and black circles indicate filled umbrellas. ΔN_B is not given for the transition at $N = 28$. (Reprinted with permission from ref 160. Copyright 1996 AIP.)

(10 for Ni), and α, β and ν are adjustable parameters. The function F_i and the parameters in ϕ_{ij} are obtained empirically from the physical properties of the bulk metal. The data basis used in the fit includes the equation of state of the metal,[164] the elastic constants, the vacancy formation energy, and the heat of solution of alloys. The EAM correctly predicts that the fcc structure is favored over the hcp and bcc structures for bulk nickel[162] and has been applied to clusters.[165−167] The ideal TIC and MIC structures were relaxed up to their respective nearest local energy minima in the energy hypersurface under the EAM forces. The first five atoms added to Ico_{13} prefer T sites over faces sharing a vertex. The next atom prefers that particular vertex site, and this cap of six atoms forms a *TIC* umbrella (see Figure 5), giving a double icosahedron structure to Ni_{19}, with two inner atoms and 17 surface atoms. This structure has also been found in simulations using other many-atom potentials[166,168−170] and the effective medium theory.[171] By adding four more atoms, the next TIC umbrella is completed in Ni_{23}, whose structure can be viewed as three interpenetrating double icosahedra. Another umbrella is completed in Ni_{26}, which is composed of five interpenetrated double-icosahedra. Completion of TIC umbrellas leads to special stability for the polyicosahedral clusters with $N = 19$, 23, 26, 29, and 32, since the binding energy increases sharply between $N-1$ and N. However, the strain accumulated by completing more and more TIC umbrellas makes the polyicosahedral structure eventually less stable compared to MIC covering, and a transition from TIC to MIC occurs after Ni_{26}. The two structures are degenerate for Ni_{27}, and a complete reordering occurs for Ni_{28}: all the atoms on faces change to edge positions and Ni_{28}, which contains three complete adjacent MIC umbrellas, becomes a fragment of Ico_{55}. Then, from $N = 28$ to 55, the cluster follows MIC covering. New umbrellas are completed for $N = 32$, 36, 39, 43, 46, and 49, and the cluster again becomes very stable when each new umbrella becomes filled. This is appreciated in Figure 6 where the difference

$$\Delta E_b = E_b(N-1) - E_b(N) \quad (31)$$

between the total binding energies of Ni_{N-1} and Ni_N has been plotted. ΔE_b gives the energy required to remove one atom from Ni_N. Peaks in ΔE_b appear when TIC umbrellas are completed for $N < 28$ and when MIC umbrellas are completed for $N \geq 28$. The figure also shows the increase ΔN_B in the number of bonds between Ni_{N-1} and Ni_N. ΔN_B shows a perfect correlation with ΔE_b, both before $N = 28$ (TIC regime) and after $N = 28$ (MIC regime).

Ni_{55} is a perfect icosahedron with two shells of atoms. Clusters with $N = 58$, 61, 64, 67, and 71 fill one, two, three, four, and five faces, respectively, of a TIC umbrella (see Figure 5), and this umbrella is completed with 16 atoms in Ni_{71}. Filling each of those faces enhances the stability of the corresponding clusters. One face of the next TIC umbrella is filled for Ni_{74}. MIC and TIC structures are very close in energy for $N = 72-74$, and the TIC−MIC transition is predicted to occur at Ni_{74}. MIC umbrellas then form at $N = 71$, 83, 92, 101, 110, 116, 125, 131, and 137, and the icosahedron is completed for Ni_{147}. Enhanced stability is predicted by filling those umbrellas and also for other few particular sizes, $N = 77$, 86, 95, 104, and 119. The stability of the last ones can be explained by analyzing in detail the increase in the number of bonds as the cluster grows.[160]

It was stated at the beginning of this section that mass spectra measured by Pellarin et al.[153] have shown the enhanced stability of Ni clusters for sizes consistent with the formation of perfect icosahedra, $N = 55$, 147, 309, 561 and also above $N = 200$, each time a face of the icosahedron is covered, and especially when a MIC umbrella is completed. In support of this view, the theoretical results indicate enhanced stability for filled umbrellas. The interpretation of the chemical probe experiments of Parks and co-workers[74,155−159] is based on the following rules for estimating the number of binding sites for nitrogen: (1) N_2 binds directly to individual nickel atoms in a standing-up configuration; (2) a Ni atom with a coordination number of 4 or less binds two Ni_2 molecules; (3) Ni atoms with a coordination number 5−8 bind one N_2 molecule; (4) Ni atoms with a coordination number of 9 bind N_2 molecules weakly or not at all; and (5) Ni atoms with a coordination number 10 or more do not bind Ni_2 molecules.[157] The adsorption results point to icosahedral symmetry for $N < 29$ and $N > 48$. Those measurements indicate that Ni_{13} and Ni_{55} are both perfect icosahedra and that the growth is polyicosahedral (that is TIC growth) up to $N = 26$, whereas Ni_{28} is a fragment of Ico_{55} with three MIC umbrellas. So, the coincidence with the theoretical calculations is outstanding since these predict the TIC−MIC transition to occur at Ni_{27}−Ni_{28}. Parks et al.[74,159] find the structural characterization of Ni_{27} difficult. The saturation coverages are inconsistent with polyicosahedral structure and consistent with a MIC cluster with an atom removed. However, the last structure would, in their opinion, be in contradiction with the large drop in the H_2O adsorption free energy between Ni_{27} and Ni_{28}, considering that in both clusters the lowest atomic coordination would be five. The contradiction is removed by the calculations. The enhanced binding energy of Ni_{28} (see Figure 6) means that the cluster will bind the adsorbed molecules weakly. So, the structure of Ni_{27} consistent with the experiments may well be, as for Ni_{28}, a fragment of Ico_{55}. The region $28 < N < 48$ has not been studied in great detail, although a preliminary analysis of N_2 uptake shows some evidence for fcc packing for some clusters in this size region.[74,159] However, we note a correlation between a minimum in the experimental adsorption free energy of H_2O on Ni_{32} and the peak of ΔE_b corresponding to the filling of four umbrellas. Additional work is required in this region. The icosahedral structure reappears clearly for Ni_{48}.[157]

Ni_{38} and Ni_{39} are special cases where the adsorption of N_2 has been analyzed in detail. The measured saturation coverages of Ni_{38} with different molecules (N_2, H_2, CO) have been interpreted as indicating that the structure of this cluster is a truncated fcc octahedron. It will be discussed in detail in section IX that theoretical calculations based on many-body potentials agree with this structure. The adsorption of N_2 on the surface of Ni_{39} has also been studied in detail.[172] Two saturation levels are evident in the uptake data at very low temperatures, one at Ni_{39} $(N_2)_{27}$ and one at Ni_{39} $(N_2)_{32}$, and these have been interpreted as representing the saturation of two separate isomers. With a long time for relaxation of the bare clusters before reaction, the second isomer (isomer A) becomes favored over the first one (isomer B), and for this reason isomer A was considered to be the ground state of Ni_{39}. According to the binding rules for N_2 adsorption,[157] this cluster has 32 surface atoms with coordination between 5 and 8. The first conclusion is that the structure of Ni_{39} is not related to that of Ni_{38}, which is an fcc octahedron that binds 24 N_2 molecules at saturation. A candidate with the required property is the icosahedral fragment of Ico_{55} obtained by removing a 16-atom cap. The surface of this cluster has 32 binding sites available for N_2 adsorption: 22 of those atoms have coordination 6 and the remaining 10 atoms have coordination 8. Another candidate is the most stable isomer calculated by Wetzel and De Pristo[173] using the corrected effective medium method: this is composed of two 16-atom "caps" joined together along their symmetry axis, one staggered relative to the other, surrounding a 7-atom pentagonal bipyramid. The caps are formed by one apex atom surrounded by 5 atoms (like an apex of an icosahedron) and 10 additional atoms forming the belt of the cap. The Wetzel−De Pristo ground state also binds 32 N_2 molecules: 12 surface atoms have coordination 6 and 20 surface atoms have coordination 8. A small rotation of one cap with respect to the axis of the internal pentagonal bipyramid leads to the next most stable isomer of Wetzel and De Pristo: this has 27 available sites for N_2 adsorption, 12 of those atoms have coordination 6, 10 have coordination 7, and 5 have coordination 8. Parks et al.[172] have proposed the two lowest energy isomers of Wetzel−De Pristo to be isomers A and B, respectively, in the reactivity experiments. This interpretation is further supported by the fact that

the experiments show conversion of isomer A to isomer B with increasing nitrogen pressure in the flow-tube reactor and retroconversion back to isomer A for even higher pressure. This reveals that the relative stability of isomers A and B changes with the number of adsorbed N_2 molecules, and these changes of relative stability can be also explained by looking at the number of atoms with coordination 6, 7, and 8 and noticing that the binding of N_2 to atoms of coordination 6 is the strongest, and then those atoms will be the first ones to be covered, then atoms of coordination 7 (favoring isomer B), and finally atoms of coordination 8 (favoring conversion back to isomer A). This dependence of isomer stability on the degree of adsorption introduces a warning concerning the interpretation of the cluster geometries inferred from reactivity experiments. Pursuing this point one can notice that the icosahedral structure of Ni_{39} has 22 surface atoms of coordination 6 that will bind N_2 molecules strongly and can make this "covered" cluster competitive with the structures of Wetzel and De Pristo.

After completing the Ni_{55} icosahedron, the experiments are consistent with TIC covering up to the formation of a 16-atom umbrella for Ni_{71}, although the structures of Ni_{66} and Ni_{67} remain yet unidentified. The binding of water molecules[174] shows minima at $N = 58$, 61, and 64 that are highly stable clusters because of the filling of faces of a TIC umbrella. But the growth model cannot explain the lack of a minimum at $N = 67$ and the existence of a minimum for $N = 69$. There are measurements of ammonia uptake and of the binding of water molecules[174] that show size oscillations correlating with the formation of MIC umbrellas for $N > 71$. For example, the ammonia uptake is a minimum for $N = 83$, 92, 101, 116, 125, and 131, all of them predicted by the model to have completed umbrellas. Also, the water binding is maximum for $N = 72$, 93, and 102, which are clusters with filled umbrellas plus a single atom, and for $N = 87$, 96, and 105. For all those clusters the relative stability, measured by the function $S(N) = E_b(N - 1) + E_b(N + 1) - 2E_b(N)$, shows minima.[160] There are maxima in the water binding at $N = 66$ and 81 that the model does not explain.

The reactivity of Ni_N^+ clusters with CO has been studied by another group.[176] Analysis of the saturation limits and comparison with predictions of the polyhedral skeletal electron-pair theory[177] indicate that the growth can be explained by the icosahedral model, forming a pentagonal bipyramid in the case of Ni_7^+, and by capping this structure to build up an icosahedron at Ni_{13}^+ and a double icosahedron at Ni_{19}^+.

Several other calculations have been performed for Ni clusters. Molecular dynamics simulations with a many-body potential based on the tight-binding method have been performed by Rey et al.[166] and Garzón and Jellinek[169] for small clusters. Stave and De Pristo[175,171] used the corrected effective medium theory for Ni_N with $N \leq 23$. EAM calculations for small,[166,168,170,178] medium,[179,180] and large[165,167] clusters give support for the icosahedral growth for clusters with more than 13 atoms, at least for sizes not far from shell closing. A semiempirical tight-binding method has been applied by Lathiotakis[181,182] to compare the relative stabilities of Ni_N clusters with icosahedral and fcc-like structures for $N = 13$, 55, and a few sizes in between. The picture arising from the tight-binding calculations is that the icosahedral structures are preferred near the closed-shell sizes $N = 13$ and 55 and that a strong competition is established for open-shell clusters in between, with some predominance of the fcc structures. The excess binding energies favoring the fcc structure for $N = 19$, 23, 24, and 38 are 0.08, 0.07, 0.05, and 0.017 eV/atom, respectively. One should recall that the reactivity experiments discussed above support, instead, the double icosahedron for Ni_{19} and the triple icosahedron for Ni_{23}.

It is fair to conclude that uncertainties still exist about the structure of Ni clusters for sizes in the region midway between closed shells. Doye and Wales[183] have proposed that the reason for the difficulties in analyzing the reactivity experiments in this size range is that a number of those clusters may have ground-state structures that do not belong to any of the usual morphologies (icosahedral, decahedral, close packed). They arrived at this conclusion by a careful Monte Carlo minimization of the energy for clusters modeled by the Finnis-Sinclair family of many-atom potentials[184,77] given in eqs 9 and 10. The corrected effective medium theory[173] and the embedded-atom calculations of Vlachos[180] lead to the same conclusion. However, the exponents n and m in the Finnis−Sinclair potential are usually fitted to solid state data and the values chosen for Ni, namely $n = 9$, $m = 6$, seem to underestimate the stability of icosahedral structures. Besides, since the icosahedral clusters Ni_{13} and Ni_{55} turn out to be very stable, a metastable growth of icosahedral clusters in some experiments may be conceivable.

VIII. Magnetism. Experiments and Simple Models

A. Introduction

Clusters in a molecular beam are free from any interaction with a matrix. It is then possible to determine their intrinsic magnetic properties in a clean way by using an appropriate experimental technique. The dependence of the magnetic properties on the cluster size can be determined in a Stern−Gerlach experiment in which the free magnetic clusters interact with an applied inhomogeneous magnetic field and are deflected from the original beam trajectory. The deflection of a cluster travelling with a velocity v transversely to the field gradient direction (defined as the z direction) is given by[185,186]

$$d = K\frac{M(B)}{mv^2}\frac{\partial B}{\partial z} \tag{32}$$

where m is the cluster mass, $\partial B/\partial z$ is the magnetic field gradient in the z direction, and K is a constant which depends on the geometry of the apparatus. This equation shows that the deflection is proportional to the cluster magnetization $M(B)$. The deflection experiments[185−191,76] are normally analyzed as-

suming that the free ferromagnetic clusters are single-domain particles following the superparamagnetic behavior,[192] which is true under certain experimental conditions,[193] namely, when the thermal relaxation time of the clusters is much lower than the time required by the clusters to pass through the poles of the Stern−Gerlach magnet. In this case the N atomic moments of a particle with N atoms are coupled by the exchange interaction giving rise to a large total magnetic moment μ_N that is essentially free of the cluster's lattice. This orientational freedom allows the magnetic moment to align with an external magnetic field. For an ensemble of particles in thermodynamic equilibrium in an external field $\boldsymbol{B}$, the magnetization (that is, the average projection of the magnetic moment of the particles along the field direction) reduces, in the low-field limit ($\mu_N B \ll k_B T$) and for large particles, to

$$M(B) = \frac{{\mu_N}^2 B}{3k_B T} \tag{33}$$

Equations 32 and 33 allow for an experimental determination of μ_N. The average magnetic moment $\bar{\mu} = \mu_N/N$ of the monodomain particle is analogous to the saturation magnetization of the bulk, but in zero field a monodomain particle has a magnetic moment different from zero.

The magnetism is sensitive to the symmetry, local coordination, and interatomic distances in the cluster. These three characteristics are interrelated. Take first the free atoms as an extreme case. Fe, Co, and Ni atoms have 8, 9, and 10 outer electrons, respectively, to be distributed in the outer 3d and 4s shells. Hund's rules require the spin to be a maximum, and this leads to electronic configurations $3d^{\uparrow 5}\,3d^{\downarrow 1}4s^2$ for Fe, $3d^{\uparrow 5}\,3d^{\downarrow 2}4s^2$ for Co, and $3d^{\uparrow 5}\,3d^{\downarrow 3}4s^2$ for Ni. The $3d^{\uparrow}$ and $3d^{\downarrow}$ subshells are separated by the exchange interaction. Hence, these atoms have nonzero spins, and since the spin magnetic moment of an electron is 1 μ_B, the atoms have substantial magnetic moments. When the atoms come together in a cluster or in the solid metal, the overlap between the atomic orbitals of neighbor atoms gives rise to energy bands. The levels corresponding to 4s electrons produce a very broad free-electron-like band of delocalized orbitals, with a large width in the solid of $W = 20-30$ eV, while the d electrons still stay fairly well localized on the atomic sites, and the width of the d band is much smaller, typically $W = 5-10$ eV in the bulk. The crystal potential stabilizes the d and s states by a different amount. This, plus spd hybridization, leads to a charge transfer from s to d states and the number of s electrons for systems other than the atom is close to 1. Assuming that the 3d orbitals are atomic-like, Hund's rule requires the majority $3d^{\uparrow}$ subband to be fully occupied with 5 electrons per atom while the minority $3d^{\downarrow}$ subband has 2, 3, and 4 electrons per atom in Fe, Co, and Ni, respectively. The difference in the number of spin ↑ and spin ↓ 3d electrons per atom $n_d(\uparrow) - n_d(\downarrow)$ is 3, 2, and 1 for Fe, Co, and Ni, respectively, and the magnetic moments per atom are $\bar{\mu}(\mathrm{Fe}) = 3\mu_B$, $\bar{\mu}(\mathrm{Co}) = 2\mu_B$, $\bar{\mu}(\mathrm{Ni}) = \mu_B$. These values are quite close to the magnetic moments per atom of very small clusters. The bulk values, $\bar{\mu}(\mathrm{Fe}) = 2.2\mu_B$, $\bar{\mu}(\mathrm{Co}) = 1.7\mu_B$, $\bar{\mu}(\mathrm{Ni}) = 0.64\mu_B$, are smaller and their noninteger values originate from the partial delocalization of the 3d electrons, which also contributes to the mutual alignment of the magnetic moments. This is known as itinerant exchange. By comparing the photoelectron spectra of negatively charged Ni_N^- and Pd_N^- clusters to those of Cu_N^-, Gantefor and Eberhardt[194] have studied the onset of delocalization of the d electrons. In small Cu clusters, the orbitals of the closed $(3d)^{10}$ shell are well localized, the interaction between the d cores can be neglected,[195] and the bonding is caused by the 4s electrons mainly. The photoelectron spectra of Ni_N^- with $N \leq 6$ is closely similar to the corresponding one of Cu_N^-. This was analyzed, and the conclusion of Gantefor and Eberhardt is that the 3d orbitals of very small Ni_N^- clusters ($N < 7$) are also almost totally localized and that the interaction between the $3d^9$ cores is negligible. Ho et al.[66] made the same observation earlier for Cu_2^- and Ni_2^- from the analysis of the similarity of their spectra. The spectra of larger clusters (Ni_N^-, $N \geq 7$) reflects the onset of delocalization of the 3d electrons. The data for small Pd_N^- clusters has some similarities to Ni_N^-.

The variation of the average magnetic moment as a function of the number of atoms in the cluster, from the atom on one extreme to the bulk on the other, is in general not smooth. The overall decay is due to the increasing average number of nearest neighbors, which enhances the itinerant character of the d electrons. On the surface of the clusters, this number is still low compared to the bulk, so only when the number of surface atoms becomes small compared to the total number of atoms in the cluster $\bar{\mu}_N$ converges to $\bar{\mu}$(bulk). Also, small or medium size clusters normally have structures that are not a simple fragment of the crystal. These ingredients affect the detailed broadening of the electronic levels to form the d bands. So the exchange splitting between ↑ and ↓ spin d subbands, the charge transfer from the s to the d band, and the *sd* hybridization depend on N and control the evolution of $\bar{\mu}$.

B. Size Dependence of the Magnetic Moments

Under conditions where the clusters follow superparamagnetic behavior, the magnetic moments of Fe, Co, and Ni clusters with sizes ranging from about 25 to 700 atoms have been measured by Billas et al.[185,186,191] for low cluster temperatures (vibrational temperature $T_{vib} = 78$ K for Ni and Co and $T_{vib} = 120$ K for Fe clusters). The results are given in Figure 7. The largest magnetic moments occur for the smallest clusters. Roughly speaking, the magnetic moment per atom decreases for increasing cluster size and converges to the bulk value for a few hundred atoms, although this convergence is faster for the Ni clusters. However, in the three cases, weak oscillations are superimposed to the global decrease of $\bar{\mu}$, and the maxima and minima of the oscillations occur at different cluster sizes for the different metals. Bloomfield and co-workers[76] have recently measured the magnetic moments of size-selected nickel clusters between $N = 5$ and 740 with high

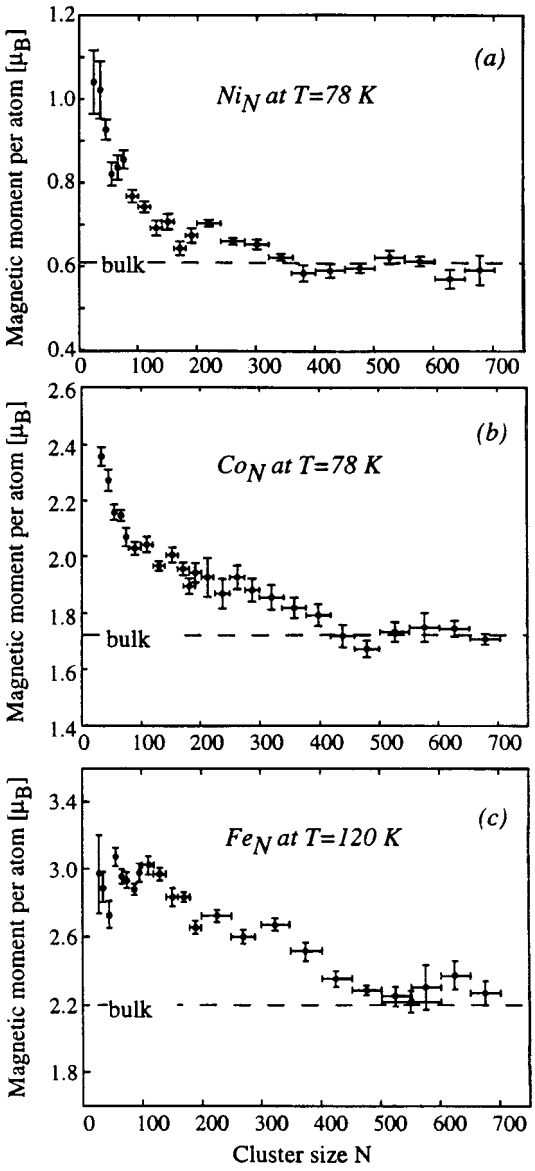

Figure 7. Magnetic moments per atom as a function of cluster size N for (a) Ni_N at $T = 78$ K, (b) Co_N at $T = 78$ K, (c) Fe_N at $T = 120$ K. (Reprinted with permission from ref 186. Copyright 1997 Elsevier Science.)

precision. These results will be discussed in detail in section IX.

Experiments have also been performed for clusters of 4d and 5d metals, which are nonmagnetic in the bulk.[196] Rhodium is an intriguing case. The measurements of Cox et al.[196] give nonzero magnetic moments for Rh clusters with less than 60 atoms, although larger clusters are nonmagnetic. Clusters with about 10 atoms have magnetic moments $\simeq 0.8\ \mu_B$, and $\bar{\mu}$ decays fast between $N = 10$ and 20 showing, however, some oscillations that produce large moments for Rh_{15}, Rh_{16}, and Rh_{19}. The magnetic moment for Rh_{20} has already been reduced to a small value of $\bar{\mu} = 0.2\ \mu_B$ and $\bar{\mu}(Rh_{60}) = 0.05 \pm 0.1\mu_B$. The case of Rh was the first one where magnetism is observed in clusters of a nonmagnetic solid metal. This behavior is different from that observed in clusters of 3d elements (Fe_N, Co_N, Ni_N) where the variation of $\bar{\mu}$ extends over a much wider range of cluster sizes. In contrast to Rh, ruthenium and palladium clusters with 12 to more than 100 atoms are reported to be nonmagnetic.[196]

The decay of $\bar{\mu}$ with cluster size can be easily explained from simple models.[197] Neglecting the contribution of the sp electrons and using Friedel's model of a rectangular d band,[139] the local density of electronic states (LDOS) with spin σ at site i is expressed[140]

$$D_i^{\sigma}(\epsilon) = \begin{cases} \dfrac{5}{W_i} & \text{for } -\dfrac{W_i}{2} < \epsilon - \epsilon_d^{\sigma} < \dfrac{W_i}{2} \\ 0 & \text{otherwise} \end{cases} \qquad (34)$$

Here ϵ_d^{σ} is the energy of the center of the σ spin subband and W_i is the local bandwidth (assumed equal for $\uparrow$ and $\downarrow$ spins). The second moment approximation in tight-binding theory[140] gives W_i proportional to the square root of the effective local coordination number Z_i

$$W_i = W_b(Z_i/Z_b)^{1/2} \qquad (35)$$

where W_b and Z_b are the bandwidth and the coordination number of the bulk solid, respectively. If the d-band splitting $\Delta = |\epsilon_d^{\uparrow} - \epsilon_d^{\downarrow}|$ caused by the exchange interaction is assumed independent of cluster size and equal to the bulk value, the local magnetic moment

$$\mu_i = \int_{-\infty}^{\epsilon_F} [D_i^{\uparrow}(\epsilon) - D_i^{\downarrow}(\epsilon)]d\epsilon \qquad (36)$$

becomes

$$\mu_i = \begin{cases} \left(\dfrac{Z_b}{Z_i}\right)^{1/2} \mu_b & \text{if } Z_i \geq Z_c \\ \mu_{dim} & \text{otherwise} \end{cases} \qquad (37)$$

where Z_c is the limiting coordination below which the magnetic moment of that atom adopts the value μ_{dim} of the dimer (magnetic moments for dimers are larger than for bulk solids). For instance, for Ni one can choose $Z_c = 5$.[198] The average magnetic moment $\bar{\mu}_N = 1/N\sum_{i=1}^{N} \mu_i$ strongly depends on the ratio of the number of surface atoms and bulklike atoms in the cluster. The former ones have small Z_i and large μ_i, while the internal atoms have $Z_i = Z_b$ and $\mu_i = \mu_b$. For small clusters, almost all atoms are surface atoms and $\bar{\mu}$ is large. However, as N increases, the fraction of surface atoms decreases and with it $\bar{\mu}$. A very simple expression was also proposed by Jensen and Bennemann,[199] who wrote

$$\bar{\mu}_N = \mu_b + (\mu_s - \mu_b)N^{-1/3} \qquad (38)$$

where μ_s is the magnetic moment of surface atoms. Strictly speaking, the formula is valid for large N but it clearly displays the decrease of $\bar{\mu}$ toward μ_b with increasing N. However, the experiments indicate that $\bar{\mu}$ varies with N in an oscillatory way and its explanation requires detailed consideration of both the geometry and the electronic structure.

C. Magnetic Shell Models

Transition-metal clusters do not display the striking magic number effects associated to the closing of

electronic shells characteristic of sp metal clusters.[3] For this reason it would be reasonable to expect the oscillations of $\bar{\mu}$ to be associated to the development of *atomic shells*, and several magnetic shell models of increasing degree of realism have been developed. The first shell model was developed by Billas et al.[185,186,191] The clusters were assumed to be formed by several atomic shells, and the magnetic moment of an atom was taken as depending only on how far the atom is located below the surface of the cluster, such that values μ_1, μ_2, μ_3, ... are assigned to atoms in layers 1, 2, 3, ...; here layer 1 indicates the most external (surface) layer. These values μ_i were taken independent of the cluster size. Then the observed trend of a decrease of $\bar{\mu}$ with N is reproduced by assigning the following empirical values for μ_1, μ_2, μ_3, μ_4, ...: (1.2, −0.4, 0.6, 0.8, 0.67, 0.65, 0.62, 0.6) for Ni, (2.7, 0.4, 1.6, 1.45, 1.9, 1.9, 1.9, 1.7) for Co, and (3, 3.2, 0, 0, 3.2, 3, 2.8, 2.5) for Fe, in units of μ_B. These numbers show that the moments of the atoms in the surface layer are enhanced with respect to those of inner layers. However, the model is oversimplified and although it reproduces the decay of $\bar{\mu}$, it does not reproduce the intriguing oscillations superimposed to its global decrease.

Jensen and Bennemann[199] presented another shell model in which the clusters are assumed to grow shell-by-shell, occupying sites of an underlying body-centered-cubic (bcc) or a face-centered-cubic (fcc) lattice, and having global regular shapes (which minimize the surface energy): cube, octahedron, and cuboctahedron. In addition to those global cluster shapes, another model of growth was considered assuming the successive occupation of coordination shells around the cluster center. Each coordination shell is formed by those atoms at a common distance from the cluster center, and this yields clusters with spherical shape. To assign magnetic moments to the different atoms in the cluster, the general rule holds that the moments are different for different atomic shells and even more these may vary within the most external shells. The average coordination number Z is largest for almost filled atomic shells. Then maxima of Z should correspond to minima of $\bar{\mu}$, and oscillations of $\bar{\mu}(N)$ as a function of N are expected as a consequence of the formation of successive atomic shells. This oscillatory behavior modulates the monotonic decay of $\bar{\mu}$ given by eq 38. Using these growth models, Jensen and Bennemann calculated the number of atoms N corresponding to clusters with closed atomic shells. These numbers are given in Table 2 for fcc clusters with cube, octahedron, and cuboctahedron shapes and for bcc clusters with cube and octahedron shapes. For cubes and octahedrons, the table also includes results for clusters with rounded edges, obtained by removing all edge atoms from the closed-shell clusters, yielding intermediate values of N. The numbers obtained are compared in the table with the measured sizes[185,186,191] for which minima of $\bar{\mu}$ are obtained for Fe, Co, and Ni clusters in the size range $30 < N < 700$. The comparison is suggestive: the experimental minima $\bar{\mu}_{min}$ seem to roughly correspond to the growth of bcc cubes for Fe clusters, fcc cubes for Ni clusters, and fcc octahedrons for Co clusters. Although the correlation is not quantitative enough to allow for a definite conclusion about the cluster structure, it provides some support for the idea that the oscillations of $\bar{\mu}(N)$ are related to the formation of atomic shells.

Table 2. Cluster Size N for Various Cluster Structures with Closed Atomic Shells.[199] The Structures Are Face-Centered-Cubic and Body-Centered-Cubic, and the Cluster Shape Is That of a Cube, Octahedron (oct), or Cuboctahedron (c-o)[a]

shell	closed-shell cluster size					N ($\bar{\mu}_{min}$)		
n	fcc cube	fcc oct	fcc c-o	bcc cube	bcc oct	Fe	Co	Ni
2*	43	43	-	15	27		50	
2	63	85	55	35	57	45	85	72
							129	
3*	140	165		59	89		173	131
3	172	231	147	91	143	85	232	175
4*	321	399		145	203	(150)	355	(260)
4	365	489	309	189	289	191	483	381
5*	610	777	-	285	385	273		625
5	666	891	561	341	511			
6*	1031	1331		491	651			
6	1099	1469	923	559	825	551		

[a] Asterisks refer to rounded clusters with edge atoms removed. Calculated N are compared with experimental sizes for which the average magnetic moment is found to yield minima.

To make the comparison more quantitative, proposals were made by the same authors for the local moments by taking into account the atomic environment. A statistical model was first proposed in which the average magnetic moment per atom of the outermost shell (1) is assumed to be

$$\bar{\mu}_1 = (1 - X_1)\mu_{at} + X_1\mu_s \tag{39}$$

where X_1 is the concentration of statistically occupied sites in this shell. μ_{at} is the magnetic moment of an atom without nearest neighbors in the topmost shell, and μ_s is that for a surface atom surrounded by other atoms in the topmost shell, taken to be similar to μ for a surface atom in the bulk material. Next, the average magnetic moment of shell 2 below shell 1 was taken to depend on the concentration X_1 of occupied sites on shell 1

$$\bar{\mu}_2 = (1 - X_1)\mu_s + X_1\mu_b \tag{40}$$

This means that the magnetic moment of an atom in shell 2 is equal to μ_s if it has no nearest neighbors in shell 1 and is equal to the bulk value μ_b if it is covered by atoms of shell 1. For shells 3, etc., magnetic moments are taken equal to μ_b. From the last two equations

$$\bar{\mu}_N = \frac{X_1N_1\bar{\mu}_1 + N_2\bar{\mu}_2 + N_b\bar{\mu}_b}{X_1N_1 + N_2 + N_b} \tag{41}$$

where N_1 and N_2 are the number of sites in shells 1 and 2, respectively, N_b is the total number of atoms in the inner shells, and $N = X_1N_1 + N_2 + N_b$. The average magnetic moment obtained from eq 41 yields oscillations with minima near closed shells ($X_1 = 1$) and maxima for half-filled shells. The results are given by the solid curves of Figure 8, with the following parameters: for Fe, $\mu_{at} = 4.0\ \mu_B$, $\mu_s = 3.0$

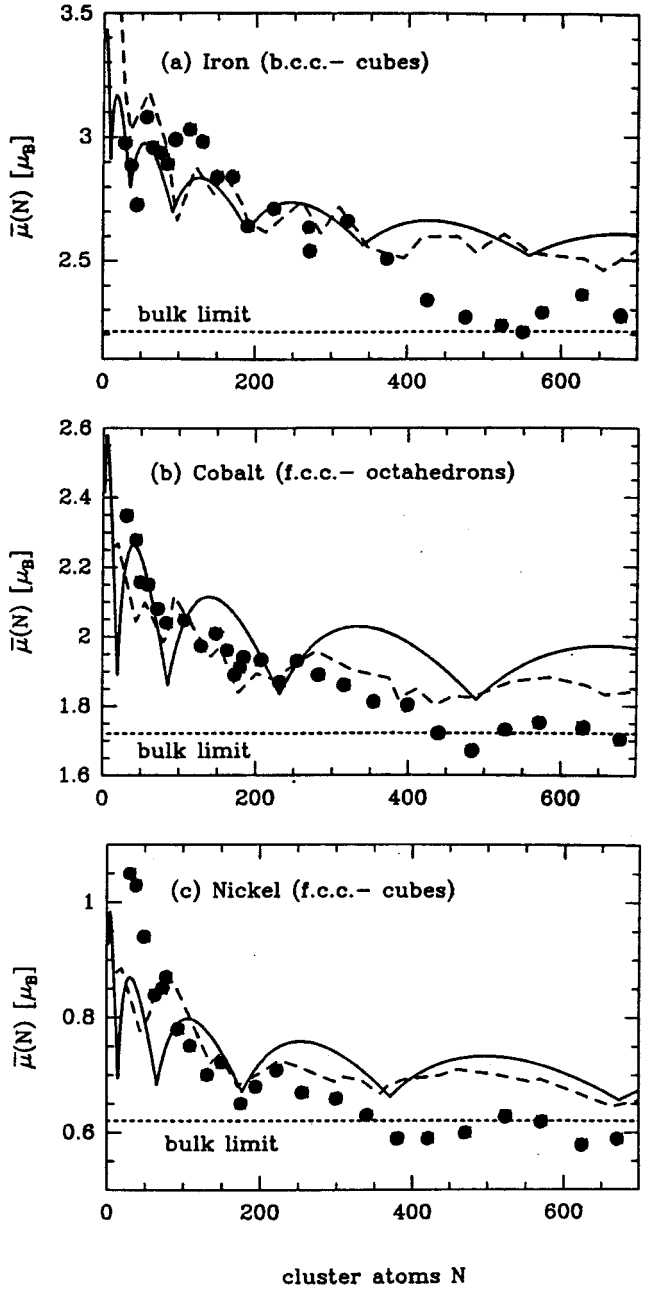

Figure 8. Calculated average magnetic moments of Fe (a), Co (b), and Ni (c) clusters as a function of N; bbc cubes are assumed for Fe, fcc cubes for Ni, and fcc octahedra for Co. The solid curves are calculated from the model of eq 41. Dashed curves are from the model of eq 42, and the dots represent the experimental results. (Adapted and reprinted with permission from ref 199. Copyright 1995 Springer.)

μ_B, $\mu_b = 2.21\ \mu_B$; for Co, $\mu_{at} = 3.0\ \mu_B$, $\mu_s = 1.9\ \mu_B$, $\mu_b = 1.72\ \mu_B$; for Ni, $\mu_{at} = 1.2\ \mu_B$, $\mu_s = 0.7\ \mu_B$, $\mu_b = 0.62\ \mu_B$. Consistent with Table 2, bcc cubes are assumed for Fe, fcc octahedrons for Co, and fcc cubes for Ni.

Another model[199] for μ_i assumes that the magnetic moment at site i is determined by its actual number of nearest neighbors, that is

$$\mu_i = \mu_i(Z_i) \tag{42}$$

The smooth dependence on Z_i can be obtained from the magnetic moments for surfaces and thin films.[200] For a bcc lattice, the local atomic properties are affected by the second neighbors, so μ_i in particular has to depended also on $Z_i^{(2)}$. These can be taken into account by defining an effective coordination number $Z_i = Z_i^{(1)} + \beta Z_i^{(2)}$, where the coefficient β describes the effective contribution from second neighbors. A reasonable value for fcc clusters is $\beta = 0.25$.[197] The results for the models of eqs 41 and 42 with parameters $\mu = \mu(Z)$ given in ref 199 are compared to experiment in Figure 8. The statistical model of eq 41 yields the minima, and the more realistic model of eq 42 improves the magnitude of $\bar{\mu}$. The agreement with experiment is encouraging in view of the simple theoretical models used, but clear evidence for a distinct cluster structure cannot be claimed. Using similar models, Zhao et al.[197] proposed for the case of Fe clusters the existence of prolate and oblate deformations from the more spherical structures, and Aguilera-Granja et al.[201] have studied this possibility for Fe clusters cut out from a simple cubic lattice with cuboid shapes (n_1, n_2, n_3): these indicate the linear dimensions of the cubic cluster along the three perpendicular axes. For simplicity they assumed $n_1 = n_2$, and then an asymmetry parameter can be defined as $f = n_3/n_1$, and $f < 1$ ($f > 1$) correspond to oblate (prolate) shapes. From a simple Friedel's model they obtain

$$\frac{\bar{\mu}_N}{\bar{\mu}_b} - 1 = 6\left(\frac{\mu_s}{\mu_b} - 1\right)\left[\frac{2f^{1/3}}{3} + \frac{1}{3f^{2/3}}\right]\frac{1}{N^{1/3}} \tag{43}$$

where μ_s is the moment of the surface atoms. By performing an expansion of the term in brackets around the symmetric case

$$\left[\frac{2f^{1/3}}{3} + \frac{1}{3f^{2/3}}\right] \simeq 1 + \frac{1}{9}(f-1)^2 - \frac{10}{81}(f-1)^3 \tag{44}$$

This indicates that for a given N, $\bar{\mu}_N$(oblate) > $\bar{\mu}_N$(prolate) > $\bar{\mu}_N$(symmetric). One also notices that for slightly asymmetric clusters the correction is second order, and in their opinion this result suggests that asymmetry may not be responsible for the behavior of the magnetic moment of Fe clusters since a large asymmetry is necessary to get a significant change in $\bar{\mu}_N$. Although this analysis holds for simple cubic clusters, the results are qualitatively similar for cubic bcc clusters.

Jensen and Bennemann[199] have also studied small Rh clusters $N \leq 40$ because these clusters order ferromagnetically,[196] although the bulk is nonmagnetic. They found that growth of an fcc cuboctahedron by caps yields better agreement with experiment than a symmetrical occupation of sites in the topmost shell. The growth by caps is expected to give larger cohesive energies because it enhances the number of nearest-neighbor contacts in the topmost shell.

D. Temperature Dependence of the Magnetic Moments

In the ferromagnetic ground state, the spins are mutually aligned. Rising T introduces disorder so that the net magnetic moment decreases. For the bulk it vanishes at the Curie temperature T_c. The behavior of $\bar{\mu}$ with temperature can give information

about the strength of the ferromagnetic order and about the stability of the magnetic ordering against thermal excitation. Billas et al.[185,186,191] have studied the variations of $\bar{\mu}$ for Ni, Co, and Fe clusters. Ni and Co clusters behave in a expected way: for a given size, $\bar{\mu}$ decreases with increasing T except for an initial plateau in Ni clusters or an initial rise of a magnitude no larger than ~5% in Co clusters. As the cluster size increases, the curve $\bar{\mu}(T)$ approaches the saturation magnetization curve of the bulk metal. However, this convergence has to be qualified. Phase transitions are sharp only for very large systems, and in a finite system, the transition becomes smeared out in temperature. The $\bar{\mu}(T)$ curve for Ni clusters of sizes $N = 500-600$ already closely follows the bulk curve at low T, but at higher T the behavior of $\bar{\mu}(T)$ is less sharp and $\bar{\mu}$ appears to approach zero much more slowly due to the finite size effects. This smearing out (which, of course, also occurs for smaller clusters) agrees with predictions using a finite Heisenberg model.[202] At temperatures around the bulk Curie temperature, the measured magnetic moment of the cluster is still substantial, suggesting that magnetic ordering is still present at these elevated temperatures. In fact, neutron scattering experiments for bulk ferromagnets indicate that ferromagnetic correlations persist at temperatures higher than T_c, leading to a short-range magnetic order with a correlation radius on the order of 10 Å,[203,204] which is a size similar to that of the free clusters in the experiments of Billas et al.

The behavior of $\bar{\mu}(T)$ for Fe clusters is clearly different. First, the temperatures where the magnetic phase transition occurs lie below T_c (bulk), although again $\bar{\mu}$ does not go to zero, and more important, the thermal behavior of $\bar{\mu}$ differs a lot for different cluster sizes and there is no obvious convergence toward bulk behavior. Billas et al. have suggested this to be a consequence of a structural transition interfering with the purely magnetic transition, as in bulk Fe. Pastor et al.[205] have analyzed the effect that short-range magnetic order (SRMO) within the cluster has on the average magnetic moment at high temperature. They first notice that in the experiments of Billas, $\bar{\mu}_N(T)$ decreases with increasing T, reaching a finite, approximately constant value above a temperature $T_c(N)$. This is expected for a magnetically disordered state.[202] The magnetization was, however, significantly larger than the value corresponding to N randomly oriented atomic magnetic moments, which is $\bar{\mu}_N(T = 0)/\sqrt{N}$. If one assumes some SRMO in the cluster and that this is characterized by the average number of atoms ν in a SRMO domain, then the magnetization per atom of an N-atom cluster at $T > T_c(N)$ is approximately given by

$$\bar{\mu}_N(T > T_c) \simeq \bar{\mu}_N(T = 0)\sqrt{\frac{\nu}{N}} \qquad (45)$$

which represents the average $\sqrt{<\mu^2>}$ of N/ν randomly oriented SRMO domains, each carrying a magnetic moment $\nu\bar{\mu}_N(T = 0)$. The disordered local moment picture, that is without SRMO, corresponds to $\nu = 1$. The actual value of ν for 3d transition-metal clusters can be estimated from known surface and bulk results.[205] $\nu = 15$ (which includes up to next-nearest neighbors in a bcc lattice) seems a reasonable estimate for Fe clusters, whereas for Ni the SRMO is expected to be stronger and values $\nu = 19-43$ are reasonable. With formula 45 and the values of ν given above, Pastor et al. obtained good agreement with experiment, providing clear evidence for the existence of SRMO in these clusters above $T_c(N)$.

Heat capacities of the clusters in the beam have been measured by Hirt et al.[206] For the Ni clusters the heat capacity C_v attains a maximum at 350 K and then decreases to the classical value. This feature is associated with the decrease in magnetic moment and indicates that the effect is due to the phase transition from the ferromagnetic to the paramagnetic state of the clusters. The heat associated with the transition is 0.022 eV/atom, which is comparable to the bulk counterpart, 0.018 eV/atom. The shape of the peak corresponds to what may be expected for a magnetic transition in a mean-field model.[207] In the same way, the mean-field approximation accounts well for the peak of C_v observed in Co clusters. The results for Fe are again more difficult to interpret. Both for low and high T, the heat capacity falls below the bulk value. And, although the position of the peak coincides with a strong decrease of $\bar{\mu}$, the shape of the mean-field peak does not reproduce the experiment.

IX. Accurate Measurements for the Magnetic Moments of Nickel Clusters and Their Interpretation

The precise experiments of Apsel et al.[76] correspond to size-selected clusters. A number of tight-binding (TB) calculations have been performed for Ni clusters with sizes lower than 100 atoms, and comparison between theory and experiment can help to elucidate the atomic and electronic structure of those clusters. The experimental moments show an overall decrease with increasing cluster size, but oscillations are superimposed on this behavior. $\bar{\mu}$ shows a pronounced minimum for Ni_{13}, and another minimum occurs at Ni_{56}, which is so close to Ni_{55} that one would guess that the clusters grow following an icosahedral pattern as stressed in section VII. A third important minimum occurs around Ni_{34}. Between Ni_{13} and Ni_{34}, as well as between Ni_{34} and Ni_{56}, the magnetic moment goes through broad maxima also displaying fine oscillations. Finally, in the small size limit, $N < 10$, where $\bar{\mu}$ decreases most rapidly, there is a local minimum at Ni_6 and a local maximum at Ni_8. The experimental results for $N \leq 60$ are reproduced in Figure 9.

A. Tight-Binding Calculations

Most studies attempting to understand these experimental results have used the TB method. For this reason we present the main features of this theoretical formalism here. A full account of the TB method and of its use for the modeling of materials has been presented by Goringe et al.[208] For a given geometrical arrangement of the atoms in the cluster (or in

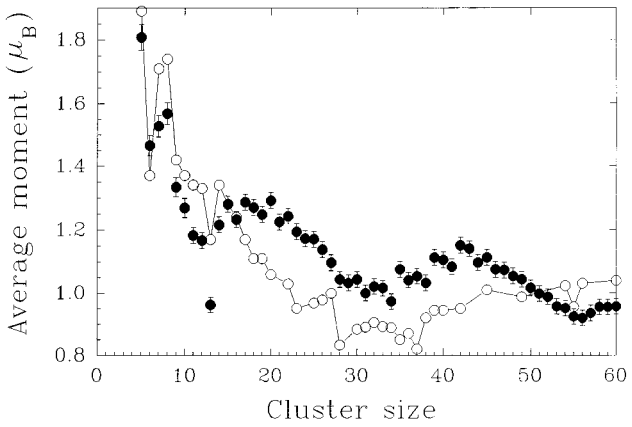

Figure 9. Calculated averaged magnetic moment of nickel clusters[218,219] (empty circles) compared with the experimental results of Apsel et al[76] (filled circles).

transition-metal slabs), the spin-polarized electronic structure can be determined by self-consistently solving a TB Hamiltonian for the 3d, 4s, and 4p valence electrons in a mean-field approximation.[209−211] In the unrestricted Hartree−Fock approximation, this Hamiltonian has the expression (using second quantization notation)

$$H = \sum_{i\alpha\sigma} \epsilon_{i\alpha\sigma}\, \hat{n}_{i\alpha\sigma} + \sum_{ij}\sum_{\alpha\beta\sigma} t_{ij}^{\alpha\beta} c_{i\alpha\sigma}^{+} c_{j\beta\sigma} \qquad (46)$$

where $c_{i\alpha\sigma}^{+}$ is the operator for the creation of an electron with spin σ and orbital state α ($\alpha = s, p_x, p_y, p_z, d_{xy}, d_{yz}, d_{xz}, d_{x^2-y^2}, d_{3z^2-r^2}$) at the atomic site i, $c_{j\alpha\sigma}$ is the annihilation operator, and $\hat{n}_{i\alpha\sigma} = c_{i\alpha\sigma}^{+} c_{i\alpha\sigma}$ is the number operator. Concerning the nondiagonal elements of H, the Slater−Koster interatomic hopping integrals $t_{ij}^{\alpha\beta}$ between orbitals α and β at neighboring atomic sites i and j are assumed to be spin independent and are usually fitted to reproduce the first-principles band structure of the bulk metal at the observed lattice constant. The variation of the hopping integrals with the interatomic distance r_{ij} is often assumed to follow a power law $(r_o/r_{ij})^{l+l'+1}$, where r_o is the bulk equilibrium distance and l, l' are the orbital angular momenta of the two orbitals involved in the hopping.[212] An exponential decay is sometimes used instead of the power law.

The spin-dependent diagonal terms contain all the many-body contributions and can be written in a mean-field approximation as

$$\epsilon_{i\alpha\sigma} = \epsilon_{i\alpha}^{0} + \sum_{\beta\sigma'} U_{\alpha\beta}^{\sigma\sigma'} \Delta\nu_{i\beta\sigma'} + \sum_{j\neq i} \frac{e^2}{r_{ij}} \Delta\nu_j + Z_i \Omega_\alpha \qquad (47)$$

Here, $\epsilon_{i\alpha}^{0}$ are the bare orbital energies of the paramagnetic bulk metal. The second term gives the shifts of the energies due to screened intra-atomic Coulomb interactions. $\Delta\nu_{i\beta\sigma} = \nu_{i\beta\sigma} - \nu_{i\beta\sigma}^{0}$, where $\nu_{i\beta\sigma} = <\hat{n}_{i\beta\sigma}>$ is the average electronic occupation of the spin−orbital $i\beta\sigma$, and $\nu_{i\beta\sigma}^{0}$ the corresponding occupation in the paramagnetic solution of the bulk. The intra-atomic Coulomb integrals $U_{\alpha\beta}^{\sigma\sigma'}$ can be equivalently expressed in terms of two more convenient quantities, the exchange and direct integrals, $J_{\alpha\beta} = U_{\alpha\beta}^{\uparrow\downarrow} - U_{\alpha\beta}^{\uparrow\uparrow}$ and $U_{\alpha\beta} = (U_{\alpha\beta}^{\uparrow\downarrow} + U_{\alpha\beta}^{\uparrow\uparrow})/2$, respectively, and then the intra-atomic term of eq 47 becomes split in two contributions

$$\sum_{\beta\sigma'} U_{\alpha\beta}^{\sigma\sigma'} \Delta\nu_{i\beta\sigma'} = \sum_{\beta} U_{\alpha\beta} \Delta\nu_{i\beta} + z_\sigma \sum_{\beta} \frac{J_{\alpha\beta}}{2} \mu_{i\beta} \qquad (48)$$

where $\Delta\nu_{i\beta} = \Delta\nu_{i\beta\uparrow} + \Delta\nu_{i\beta\downarrow}$, $\mu_{i\beta} = \Delta\nu_{i\beta\uparrow} - \Delta\nu_{i\beta\downarrow}$, and z_σ is the sign function ($z^{\uparrow} = -1$, $z^{\downarrow} = 1$). The first contribution in eq 48 arises from the change in electronic occupation of orbital $i\beta$ and the second from the change of the magnetization (spin polarization). $U_{\alpha\beta}$ and $J_{\alpha\beta}$ are usually parametrized. The difference between s and p direct Coulomb integrals is often neglected by writing $U_{ss} = U_{sp} = U_{pp}$, and it is also assumed that $U_{sd} = U_{pd}$. The ratio between the magnitudes of U_{ss}:U_{sd}:U_{dd} can be taken from atomic Hartree−Fock calculations and the absolute value of one of them, U_{dd} for instance, estimated by some means.[213,214] Typical values for these ratios are 0.32:0.42:1 for Fe and $U_{dd} = 5.40$ eV.[209] All the exchange integrals involving s and p electrons are also usually neglected, and J_{dd} is determined in order to reproduce the bulk magnetic moment. Typical values for Ni, Co, and Fe are not far from $J_{dd} = 1$ eV.

The third term in eq 47 represents the Coulomb shifts resulting from interatomic charge transfer. $\Delta\nu_j = \nu_j - \nu_j^{0}$, where $\nu_j = \sum_{\beta\sigma} <\hat{n}_{j\beta\sigma}> = \sum_{\beta} <\hat{n}_{j\beta\uparrow}> + <\hat{n}_{j\beta\downarrow}>$ is the total electronic charge at atom j and ν_j^{0} the corresponding reference bulk value. In eq 47 the interatomic Coulomb interaction integrals V_{ij} have been approximated by $V_{ij} = e^2/r_{ij}$ although other approximations have been used.[210,211,215] Finally, the last term in eq 47 takes into account the energy-level corrections due to nonorthogonality effects[10] and the crystal-field potential of the neighboring atoms,[140] which are approximately proportional to the local coordination number Z_i. The orbital-dependent constants Ω_α can be obtained from the difference between the bare energy levels (i.e., excluding Coulomb shifts) of the isolated atom and the bulk. Through this term one can also model effects on the energy levels due to bond length changes associated with the reduction of coordination number.[10,140] The spin-dependent local electronic occupations and the local magnetic moments $\mu_i = \sum_\alpha (<\hat{n}_{i\alpha\uparrow}> - <\hat{n}_{i\alpha\downarrow}>)$ are self-consistently determined from the local densities of states $\rho_{i\alpha\sigma}(\epsilon)$

$$<\hat{n}_{i\alpha\sigma}> = \int_{-\infty}^{\epsilon_F} \rho_{i\alpha\sigma}(\epsilon)\, d\epsilon \qquad (49)$$

which can be calculated at each iteration by using the recursion method.[216] The energy of the highest occupied state (Fermi energy) ϵ_F is determined from the condition of global charge neutrality. In this way, the local magnetic moments $\mu_i = \sum_\alpha \mu_{i\alpha}$ and the average magnetic moment $\bar{\mu} = 1/N \sum_i \mu_i$, are obtained at the end of the self-consistent cycle.

The theoretical framework just presented is general, although some of the calculations performed by different authors incorporate slight differences with respect to the basic method. For instance, the variation of the hopping integrals with interatomic distance is sometimes assumed to decay in an exponential way. In many works only the d electrons are considered explicitly.[213,217] However, although the

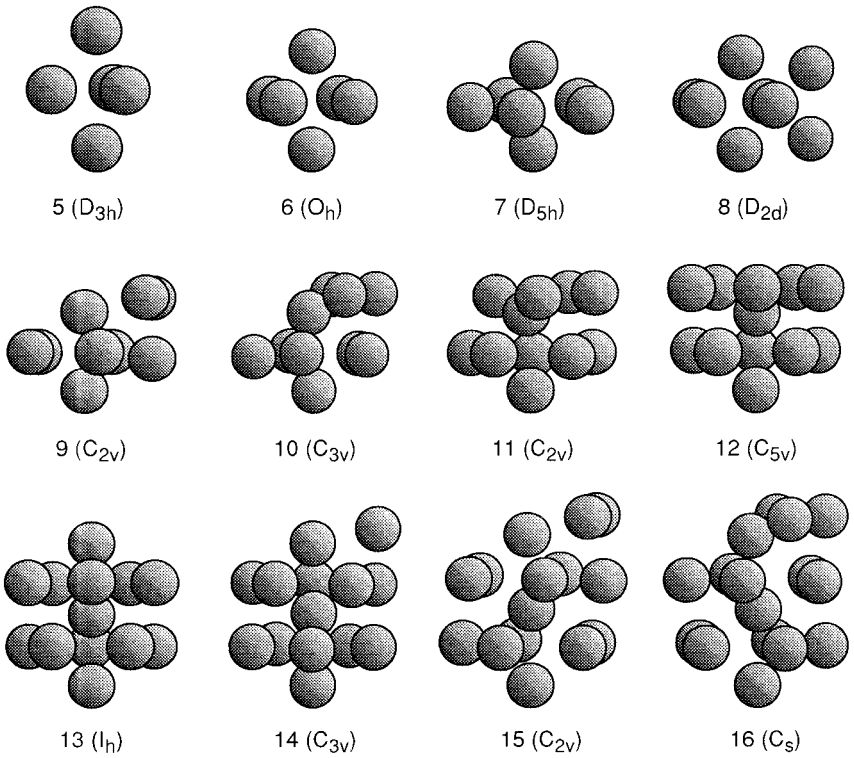

Figure 10. Ground-state geometries of Ni_N ($N = 5-16$) obtained with the Gupta potential. (Reprinted with permission from ref 218. Copyright 1997 AIP.)

spin polarization in the cluster is expected to be dominated by the d electrons, the sp electrons should have influence on the magnetic properties as a result of spd hybridization, spd charge transfer, and the resulting contributions to the many-body potential, *i.e.*, to the level shifts due to Coulomb interactions. Guevara et al.[215] have pointed out the importance of electron spillover through the cluster surface, and they took this effect into account by adding extra orbitals with s symmetry (s′ orbitals) outside the surface, as it had been done earlier by the same authors for the surface of transition metals.[211]

In Figure 9 we give the results of TB calculations for the average magnetic moments of Ni_n clusters up to Ni_{60}.[218,219] Those results are compared with the experimental values of Apsel el al.[76] Two key ideas will be used to interpret the results. The first one is that the local magnetic moments decrease with increasing local coordination around an atom. This idea, which becomes confirmed by the calculations,[142] has also been used to understand the magnetic moments at planar surfaces and surfaces with defects.[220] The second idea is that the average magnetic moment decreases when the interatomic distances decrease (the d band becomes wider). In metallic clusters, the average coordination generally increases with increasing size N and also the average nearest-neighbor distances d increase with N, from the value for the molecule (d_{mol}) to the value for the bulk (d_{bulk}), that is $d_{bulk} > d_{mol}$. This means that in a growing cluster the two effects oppose each other and the resulting behavior of $\bar{\mu}(N)$ can be very rich. For $N \leq 20$, the geometrical structures used to perform the electronic structure calculations have been obtained from classical molecular dynamics (MD) simulations using a semiempirical many-atom potential[146,221] based on TB theory, with parameters fitted to properties of Ni_2 and bulk Ni.[222] This potential energy has the form

$$V = \frac{1}{2}\sum_i [\sum_j A e^{-p(l_{ij}-1)} - (\sum_j \xi e^{-2q(l_{ij}-1)})^{1/2}] \quad (50)$$

Here $l_{ij} = r_{ij}/r_0$ is the distance between atoms i and j divided by the equilibrium nearest-neighbor distance in the bulk metal and ξ, A, p, q, and r_o are adjustable parameters. The first term gives a pairwise repulsion energy of the Born−Mayer type. The second is a many-body attractive contribution giving the band energy calculated in the second moment approximation to the TB model. The potential of eq 50 is often called the Gupta potential.[146]

In the small cluster size range, the qualitative agreement between calculated magnetic moments and experiment is very good. The theory predicts pronounced local minima at $N = 6$ and 13 and a local maximum at $N = 8$. The atomic structures for $N = 5-16$ are plotted in Figure 10. Ni_{13} is an icosahedron with an atom inside. The coordination of the surface atoms is $Z = 6$. Either by removing or adding an atom, the resulting clusters, Ni_{12} and Ni_{14}, respectively, contain some atoms with coordination smaller than 6 (the average coordination is given for all the clusters in Figure 11(a)). This leads to an increase of the local magnetic moment of those atoms. Consequently, the minimum of $\bar{\mu}$ at Ni_{13} is explained by its compact structure. Ni_6 is an octahedron with four-coordinated atoms. In Ni_7, which has the structure of a pentagonal bipyramid, the coordination of two atoms increases to $Z = 6$, remaining equal to $Z = 4$ for the rest. Ni_8 has four atoms with coordination Z

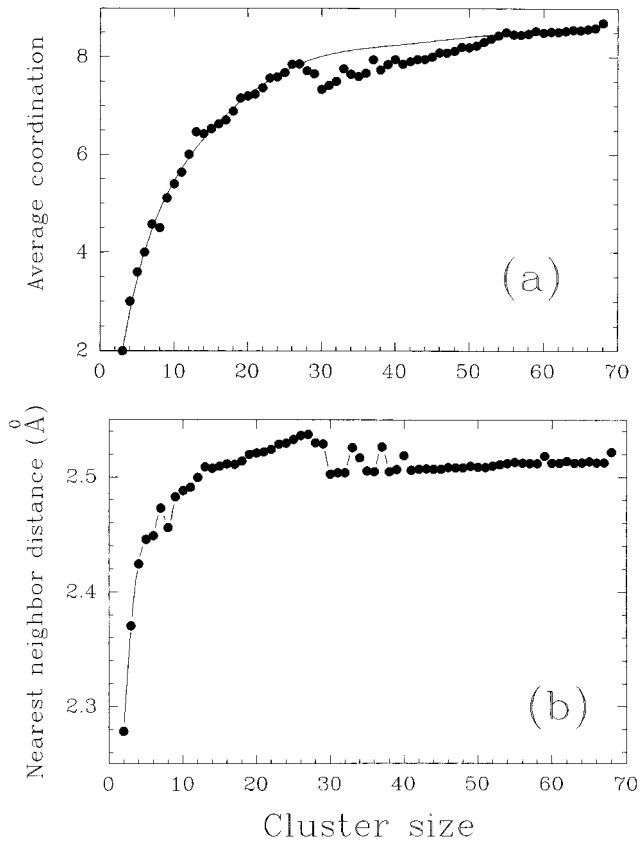

Figure 11. Calculated average coordination number (a) and average nearest-neighbor distances (b) as a function of cluster size. The line in a is an extrapolation from small sizes to sizes larger than $N = 27$. (Reprinted with permission from ref 219. Copyright 1998 AIP.)

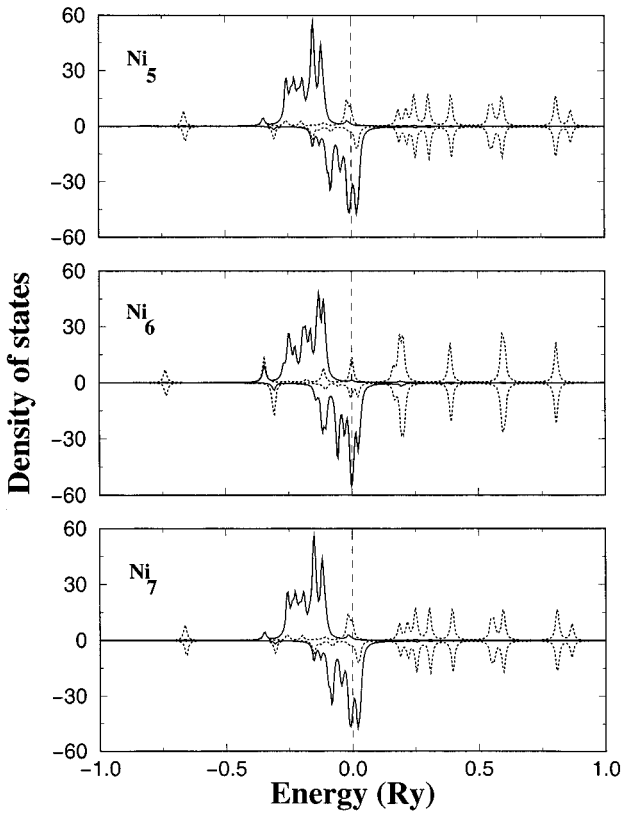

Figure 12. Density of electronic states, decomposed in sp (dashed line) and d (thick line) contributions. Positive and negative values refer to up and down spins, respectively. The Fermi level is at $\epsilon = 0$. (Adapted with permission from ref 218.)

$= 5$ and four atoms with coordination $Z = 4$, which leads to a mean coordination slightly lower than in Ni_7, and then the coordination increases again for Ni_9. This would lead us to expect a maximum of $\bar{\mu}$ for Ni_8, which is indeed observed in the experiment, and a minimum for Ni_7. Instead, the observed and calculated minimum occurs at Ni_6, and the reason is that the average first-neighbor distance d (plotted in Figure 11b) has a local maximum at Ni_7, that is, $d(Ni_7)$ is larger than $d(Ni_6)$ and $d(Ni_8)$. The larger value of d works against the increase of the coordination number from Ni_6 to Ni_7 and produces the minimum of $\bar{\mu}$ at Ni_6. In summary, the full details of the oscillations of $\bar{\mu}$ for small N can be explained by purely geometrical arguments: compact clusters have small $\bar{\mu}$ and clusters with large interatomic distances have large $\bar{\mu}$.

In Figure 12 the orbital-projected densities of states of Ni_5, Ni_6, and Ni_7 are compared. The occupied states of the majority-spin subband have mainly d character with the exception of the peak at the Fermi energy, which has sp character. d holes are present in the minority-spin subband, with a large d contribution at the Fermi level. Integration of the density of states gives d magnetic moments of 1.6, 1.52, and 1.50 μ_B for Ni_5, Ni_6, and Ni_7, respectively, which does not explain the behavior of Figure 9, so the sp electrons make an important contribution. The three clusters show some sp splitting: at the Fermi level for Ni_5 and Ni_7 and below ϵ_F for Ni_6. The sp moments for Ni_5 (0.29 μ_B) and Ni_7 (0.21 μ_B) reinforce the d moment, while for Ni_6 the sp moment ($-0.15\ \mu_B$) points in the opposite direction. The sp contribution to μ appears to decay quickly with cluster size, and for sizes $N = 12-14$ this contribution is already very small.[218,219]

A conclusion of the molecular dynamics study leading to the geometries plotted in Figure 10 is a pattern of icosahedral growth. This is present as early as Ni_7, since its pentagonal bipyramid structure already displays the 5-fold symmetry (supported also by ab initio calculations[79]). The icosahedral growth for Ni clusters is consistent with a large body of experimental information of reactivity with light molecules already discussed in section VII. Since icosahedral growth appears to be consistent with the reactivity experiments, Aguilera-Granja et al.[219] assumed icosahedral clusters also for $N > 20$. The structures obtained previously with the EAM[160] were reoptimized, this time using the Gupta potential of eq 50 to have consistency with the case of $N \leq 20$. The topology of the clusters remains the same as in the EAM calculation, although the interatomic distances become shorter. In addition, extensive MD simulations were done for a few selected sizes, and an investigation of isomers was performed. In all cases the icosahedral structures were recovered as the ground state (Ni_{38} is an exceptional case to be discussed later).

Returning to Figure 9, the TB calculations reveal a broad trend that can be roughly characterized as an initial decrease of $\bar{\mu}$ for sizes up to $N \approx 28$, followed by a weak increase between $N \approx 28$ and 60. This

behavior is mainly related to the variation of the average coordination number $\bar{Z}$, which is plotted in Figure 11. $\bar{Z}$ grows smoothly with N up to $N = 27$, and this explains the overall decrease of $\bar{\mu}(N)$ in this region. The change of $\bar{Z}$ is faster for small N, which correlates with the fast decrease of $\bar{\mu}(N)$. A continuous line has also been drawn in Figure 11a that extrapolates $\bar{Z}$ to sizes larger than $N = 27$. The actual calculated values of $\bar{Z}$ between $N = 27$ and 54 fall below that extrapolated curve, and the same argument now explains the behavior of $\bar{\mu}$ in that size region: the break in $\bar{Z}$ at $N = 27$ gives a reduced average coordination number that interferes with the tendency of $\bar{\mu}(N)$ to decrease, suggesting a flattening of $\bar{\mu}$ or even a weak increase, as confirmed by the calculations. The break in the behavior of $\bar{Z}$ is due to the TIC−MIC transition occurring precisely at $N = 28$ (see section VII).

The calculated minimum at $N = 55$ (as before for Ni_{13}) has a clear correspondence with a minimum in the measured moment. Also the minimum in the region Ni_{27}−Ni_{37}, associated to the TIC−MIC transition, seems to have a correspondence with the broad experimental minimum of $\bar{\mu}$ in that region. The experiments also show a weak minimum at Ni_{19} that can tentatively be associated to the double icosahedron structure of this cluster. Surprisingly, this local minimum does not show up in the TB calculations despite the change in slope of $\bar{Z}(N)$ at Ni_{19} (see Figure 11a). The reason seems to be the slight jump up in average nearest-neighbor distance, visible in Figure 11b. Another weak feature, a visible drop of $\bar{\mu}$ between Ni_{22} and Ni_{23} has a counterpart in the calculation, a clear minimum this time (the last cluster in a triple icosahedron). We then may conclude with some confidence that the minima displayed by the measured moments give additional support to a pattern of icosahedral growth, which is also consistent with reactivity experiments.

It was stated earlier that Ni_{38} is an exceptional case. The results of a recent experiment[223] measuring the saturation coverage of Ni_{38} with different molecules (N_2, H_2, CO) indicate that the structure of this cluster is a truncated octahedron cut from an fcc lattice. Motivated by this experimental result, a detailed comparison was made by Aguilera-Granja et al.[219] between fcc and icosahedral structures for a number of clusters. $N = 36$, 37, 38, 39 were selected to cover sizes in the neighborhood of Ni_{38}. For $N = 13$, 19, 43, 55, one can construct fcc clusters with filled coordination shells around a central atom, and for $N = 14$, 38, 68, one can construct clusters with filled coordination shells around an empty octahedral site of the fcc lattice. Finally, $N = 23$, 24, 44 are of interest for comparison with other works. For all these clusters one or several initial fcc arrangements were relaxed by the steepest-descent method. In some cases, the lowest energy structure obtained was distorted but the fcc structure was still recognizable. In all the cases studied, the difference in binding energy $\Delta E_b = E_b(ico) - E_b(\text{fcc})$ was positive, that is, the ico structure was more stable, except precisely for Ni_{38}, where ΔE_b is negative. ΔE_b was nearly zero for Ni_{36} and lower than 0.2 eV (although positive) between Ni_{24} and Ni_{39}. ΔE_b increases as N departs from this region. The fcc geometry of Ni_{38} is a compact structure formed by three complete coordination shells around an empty octahedral site. The six atoms of the internal octahedron are fully coordinated ($Z = 12$). For Ni_{38}, $\bar{\mu}_{fcc} = 0.99\ \mu_B$, which cuts the difference between the experimental and theoretical results to one-third of the value in Figure 9 ($\bar{\mu}_{exp} - \bar{\mu}_{fcc} = 0.04\ \mu_B$ and $\bar{\mu}_{exp} - \bar{\mu}_{ico} = 0.11\ \mu_B$). This moderate increase of $\bar{\mu}$ with respect to the icosahedral structure can be explained by the lower average coordination of the fcc structure ($\bar{Z}$(fcc) = 7.58 while $\bar{Z}$(ico) = 7.74). For Ni_{36}, $\bar{\mu}$ is very similar for the ico and fcc structures (0.87 and 0.86 μ_B, respectively). Since energy differences between isomers in the region $N = 24$−40 are small (within 0.4 eV), the possibility of different isomers contributing to the measured values of $\bar{\mu}(N)$ should not be excluded.

Explaining the maxima observed by Apsel et al. seems to be a more difficult task. Those maxima are not seen in the TB results, and this also affects the shape of the minimum at Ni_{55}. One possibility, suggested by calculation of the magnetic moments of small fcc clusters by Guevara et al.[215] and by MD simulations using a TB Hamiltonian[182] (see section IX.B below), is that the structures are fcc instead of icosahedral in the regions corresponding to those maxima. Guevara et al. predict sharp maxima at Ni_{19} and Ni_{43} and minima at Ni_{28} and Ni_{55} (the last two are fcc cuboctahedrons). But the arguments given above suggest that Ni_{19} is a double icosahedron. The minimum at Ni_{28} is also given by the icosahedral model. So the only clear prediction in favor of fcc structure may be the maximum at Ni_{43}.

To investigate further the effect of the geometrical structure, Rodríguez-López et al.[224] have performed additional calculations for geometries proposed by other authors, obtained from different semiempirical potentials. Atomic structures have been determined by Nayak et al.[225] by performing MD simulations with the Finnis−Sinclair potential,[77,184] which is also based on the TB method and contains many−body interactions (see eqs 9 and 10), and by Hu et al.[226] using both Leonard−Jones and Morse potentials. The results were compared to experiment and to the icosahedral growth model. The main conclusion is that the differences in $\bar{\mu}$ produced by the structures corresponding to the different interatomic potentials are not large and the results for the different sets of potentials are roughly consistent with each other. For all potentials $\bar{\mu}(N)$ shows an overall decrease with N and the oscillations at small N are reproduced reasonably well. All the calculations, however, give a faster decrease of $\bar{\mu}(N)$ and predict a faster approach to μ(bulk). Concerning the differences for different potentials, these are driven mainly by the differences in interatomic distances which affect, first of all, the hopping integrals and consequently the electronic structure. As expected, lower interatomic distances result in smaller magnetic moments. Another source of differences arises from intrinsic structural changes associated with the different potentials. The average coordination number reflects, to some extent, structural differences, although it is not a very precise indicator.

These new results do not resolve the discrepancies between TB calculations and experiment: namely, the near constancy of $\bar{\mu}$ between Ni_{14} and Ni_{20}, etc. This suggests that a possible misrepresentation of the exact geometry is not the only missing ingredient. We think that the treatment of the sp electrons in the TB model may not be accurate enough. A simple alternative model of the magnetic moments, which is described in section IX.C, gives a hint for the reasons.

B. Tight-Binding Molecular Dynamics

TB calculations of the magnetic moments have also been performed by Andriotis and co-workers[227,228] for Ni, Fe, and Co clusters. Two main differences can be noticed with respect to the calculations of Alonso and co-workers.[218,219] The geometrical structures are obtained by Andriotis et al. using a MD method in which the forces on the atoms are calculated within the TB scheme.[181,182,229] For this purpose, the cluster energy was written

$$E = E_{\mathrm{el}} + U_{\mathrm{rep}} + U_{\mathrm{bond}} \tag{51}$$

where $E_{\mathrm{el}} = \sum_{i\sigma}\epsilon_{i\sigma}$ is the usual sum of one-electron energy eigenvalues over the occupied states. The second term

$$U_{rep} = \sum_{i>j}\phi(r_{ij}) \tag{52}$$

accounts for the repulsive ion−ion interactions and is also intended to correct for the double-counting terms in E_{el} arising from Coulomb and exchange interactions. This repulsive term was assumed to scale exponentially with the interatomic distance r_{ij}

$$\phi(r_{ij}) = \phi_{\mathrm{o}} \exp[-4\alpha(r_{ij} - d)] \tag{53}$$

where d is the bond length in the bulk material. The value of ϕ_{o} was chosen to reproduce the correct bond length of the dimer at its correct magnetic state.[227] The third term is a coordination-dependent correction, originally introduced by Tomanek and Schluter[230]

$$U_{\mathrm{bond}} = N[a(N_{\mathrm{B}}/N) + b] \tag{54}$$

where N_{B} is the number of bonds per atom of the cluster and N is the number of atoms. This term does not contribute to the forces on the atoms but is necessary to reproduce cohesive energies of dimers through bulk. The parameters a and b are obtained by fitting U_{bond} to ab initio results for the total energy of small clusters ($N \leq 5$) according to the equation

$$U_{\mathrm{bond}} = E_{\mathrm{ab\ initio}} - E_{\mathrm{el}} - U_{\mathrm{rep}} \tag{55}$$

A form for U_{bond}, quadratic in (N_{B}/N), instead of linear, has also been used.[229] However, these TB calculations are not self-consistent and contain several approximations. In a first set of calculations, dealing with cluster structure only, Andriotis et al.[181,182,229] assumed the diagonal matrix elements of the TB Hamiltonian to be simply the atomic term values, independent of the local environment and equal to the values given by Harrison.[10] They set $\epsilon_{\mathrm{s}} = \epsilon_{\mathrm{d}}$, and ϵ_{p} was taken to be large enough to prevent p-orbital mixing. The off-diagonal terms also made use of universal parameters given by Harrison.[10] The study of Menon et al.[229] for small Ni_N clusters and the comparison they made with ab initio methods serves to illustrate the difficulties in predicting the ground-state structure. Some details of that comparison are now provided, although it has to be stressed that the majority of the ab initio calculations for Ni clusters with $N > 3$ refer to symmetry-restricted optimized geometries. For Ni_3, the TB calculation gives the D_{3h} symmetry (triangular) as the ground state, 1.7 eV more favorable than the linear ($D_{\infty h}$) isomer. In contrast, Basch et al.[231] found the linear cluster to be slightly more stable. For Ni_4, the TB ground state is a perfect square (D_{4h}), in agreement with Basch et al.[231] For this cluster, Mlynarsky and Salahub[232] found a tetrahedral (T_{d}) ground state. The T_{d} structure was unstable in the TBMD simulations, distorting to the planar D_{4h} geometry. The TB ground state of Ni_5 is a distorted tetragonal pyramid. Up to Ni_4 there is agreement with the ab initio DFT geometries of Reuse and Khanna,[63] but the prediction of these authors for Ni_5 is a trigonal bipyramid. The TB ground state of Ni_6 is a tetragonal bipyramid with a rhombic base. This distortion is in qualitative agreement with Yu and Almlof,[233] who considered Jahn−Teller distortions in octahedral Ni_6. A pentagonal bipyramid is the ground state of Ni_7, in agreement with Nygren et al.[75] Bicapped, tricapped, and tetracapped octahedra were predicted to be the ground state of Ni_8, Ni_9, and Ni_{10}, respectively. These structures were found to be distorted: the base of the octahedron is a rhombus in Ni_8 and Ni_{10} and is not even planar in Ni_9. In comparison with the results of Bouarab et al.,[218] we notice discrepancies for the structures of Ni_5, Ni_9, and Ni_{10} and a minor discrepancy for Ni_8. The TBMD method was also used for a number of selected larger clusters: Ni_{13}, Ni_{14}, Ni_{15}, Ni_{19}, Ni_{23}, Ni_{24}, Ni_{26}, Ni_{33}, Ni_{38}, Ni_{43}, Ni_{44}, and Ni_{55}. For some of those, $N = 13$, 19, 23, 24, 38, 55, icosahedral and crystalline-like fcc arrangements were relaxed and their binding energies compared. The icosahedral structure was found to be substantially more stable for Ni_{13} and Ni_{55} (by 0.43 eV/atom in the first case and by 0.17 eV/atom in the second), while for Ni_{19}, Ni_{23}, Ni_{24}, and Ni_{38} the ground state was fcc. Only for Ni_{38} was the difference in binding energy substantial (0.17 eV/atom, in reasonable agreement with ref 219), whereas for Ni_{19}, Ni_{23}, and Ni_{24} it is about one-third of this value or less. For the other sizes a direct comparison is not possible because only one structure was relaxed. One can enlarge the comparison by performing linear interpolations between studied sizes (either fcc or *Ico*). Accepting the values from those interpolations as approximate (see Figure 11 of ref 182), one arrives at the conclusion that the *Ico* structures are more stable from $N = 13$ to 18, from $N = 46$ to 55, and in a narrow region around $N = 33$. For other sizes, fcc structures appear to be more stable in the TBMD

calculations. The main message here is the strong competition between fcc and *Ico* structures.

The approximations made prevented the study of magnetism, so in a second set of improved TBMD calculations, Andriotis and workers[227,228] used a spin-unrestricted TB Hamiltonian in which the necessary spin dependence of the diagonal matrix elements is introduced using the Hubbard (H) approximation,[139] like in eq 47. For this reason the method was called the H-TBMD method. The use of the full correction to $\epsilon_{i\alpha}{}^0$ given in eq 47 is still cumbersome in a MD simulation, and Andriotis et al. made drastic simplifications, by setting

$$\epsilon_{i\alpha\sigma} = \epsilon_{i\alpha}{}^0 - \sigma s^0 \tag{56}$$

with the adjustable parameter s^0 having the meaning of an effective exchange interaction, independent of the type of orbitals and lattice sites. s^0 was determined to reproduce the correct spacing of the higher-spin states of small clusters ($N \leq 5$) available from accurate ab initio calculations.[232] The approximation $\epsilon_s{}^0 = \epsilon_d{}^0$, with values from Harrison,[10] was retained in the calculations. In summary, the H-TBMD method introduces just a single extra adjustable parameter compared to TBMD. The use of the effective Hubbard term induces qualitative changes in the ground-state geometries of very small clusters, like Ni_3, Ni_4, and Ni_5 (the last one is now a trigonal bipyramid, although very close in energy to the square pyramid[227]) but not for Ni_6.

A salient effect for larger clusters is that the icosahedral structure of Ni_{13} relaxes to a more stable very distorted prism-like structure, only 0.02 eV/atom less stable than the structure obtained by relaxing fcc structures. Without magnetic effects, icosahedral Ni_{19} was 0.135 eV/atom less stable than the fcc structure; then for magnetic Ni_{19}, the fcc structure (with $\bar{\mu} = 0.842\ \mu_B$) is only 0.013 eV/atom more stable than the icosahedral one (with $\bar{\mu} = 1.158\ \mu_B$). For Ni_{13}, magnetism does not alter the difference in binding energy between fcc and *Ico*: 0.131 eV/atom. The calculated magnetic moments show that the results are sensitive to the parameters of the TB method: Andriotis et al.[227] obtained a maximum of $\bar{\mu}$ at Ni_{13} (in contrast with the experimental minimum) and a minimum at Ni_7 (while the experimental minimum occurs at Ni_6). With a different parametrization,[228] they recover the correct minima of $\bar{\mu}$ at Ni_6 and Ni_{13} with a maximum at Ni_7 instead of Ni_8.

TBMD calculations of the magnetic moments have been performed for Fe and Co clusters.[228] In these cases a detailed comparison with experiment is very difficult and only some trends are available. The calculations for Fe reveal the expected strong dependence of $\bar{\mu}$ with cluster size and geometry, especially for small clusters, and the decrease of $\bar{\mu}$ with increasing average number of bonds per atom. Another message from the calculations is the negligible importance of s−d interactions, already noticed by Pastor and co-workers,[213,234] in contrast to Ni clusters. For Co, the limited availability of experimental data and ab initio results makes the fitting of the TB parameters difficult. For Co_{43}, the calculated magnetic moment was a 10% lower than the experimental value,[185,186,191] and for Co_{141}, the TB result is consistent with experiment.

C. Influence of s Electrons

An alternative model has been proposed by Fujima and Yamaguchi[235] for explaining the structure of $\bar{\mu}(N)$ for Ni clusters. In our opinion,[219] the model is not adequate to explain the minima of $\bar{\mu}(N)$ but it may well contain the additional ingredients required to explain the maxima. It is intriguing that the observed maxima are located at $N = 8$ and 71 and near $N = 20$ and 40.[76] These numbers remind us of some of the electronic shell closing numbers of alkali- and noble-metal clusters ($N = 8$, 20, 40, 58, 72), which are explained by the spherical jellium model. The model of Fujima and Yamaguchi distinguishes between localized 3d-derived levels and delocalized molecular orbitals derived from the atomic 4s electrons and neglects any hybridization between d and delocalized electrons. The delocalized electrons are treated as moving in an effective harmonic potential, and the corresponding levels initially lie above the Fermi energy in very small Ni clusters. But as N grows, the binding energy of these delocalized states increases and the levels become successively buried below the 3d band. The model assumes that this occurs abruptly when the number of delocalized electrons is just enough to fill a shell in that harmonic potential. Associated with this stepwise effect, there is a sudden increase of the number of holes at the top of the minority spin d band, since the total number of valence electrons per Ni atom is 10: the number of holes is equal to the number of unpaired electrons in the cluster, so an abrupt increase of $\bar{\mu}$ occurs. The stepwise mechanism of transfer of 4s-derived levels from above the Fermi energy to below the d band is supported by density functional calculations.[236] Then the maxima of $\bar{\mu}$ observed in the experiments for $N \leq 100$ could be related to this effect. However, in the model the maxima and the minima of $\bar{\mu}$ are too close due to the drastic assumption of the transfer of a whole shell at once when the conditions of shell closing are met. This is in contrast to the experimental observation, where the maxima and minima are well separated and, furthermore, the minima appear to be due, as discussed in previous sections, to structural effects.

The TB model distinguishes between sp and d electrons, and the analysis of the density of states indicates that groups of levels with non-d character progressively appear below the d band as N increases.[219] However, this transfer is smooth (not sharp) and there is, in addition, sizable sp−d hybridization. In short, the TB calculations do not produce the sharp shell-closing effects assumed in the model of Fujima and Yamaguchi. It is not evident if this is a failure of the TB method or if this behavior may be reproduced with a different fit of the TB parameters. This immediately suggests that one perform density functional (DFT) calculations that in principle include the required ingredients for a full explanation of the behavior of $\bar{\mu}$.

X. Density Functional Studies of the Magnetism of Clusters of 3d Elements

These calculations become difficult for large clusters, especially if one wishes to determine the equilibrium lowest energy geometrical structure. For this reason, only very small Ni clusters have been studied by DFT. Reuse and Khanna[63] have calculated $\bar{\mu}$ for Ni_N with $N = 2-6$, 8, 13. The trend of decreasing $\bar{\mu}$ between Ni_5 and Ni_6 and between Ni_8 and Ni_{13} was obtained, but the magnetic moments of Ni_6 and Ni_8 were predicted to be nearly equal, while the experiment gives a larger moment for Ni_8 (see Figure 9). The geometries employed for Ni_5, Ni_6, and Ni_{13} are similar to those of Bouarab et al.,[218] i.e., bipyramids for Ni_5 and Ni_6 and the icosahedron for Ni_{13}, although with smaller interatomic distances (the smaller interatomic distances may account for the lower moments). The geometry of Ni_8 was a regular cube. Bouarab et al.[218] have performed additional TB calculations with the same interatomic distances and structures of Reuse and Khanna, and the magnetic moments differed by no more than 0.06 μ_B from the TB values of Figure 9, so the differences between the TB results of Bouarab et al. and the DFT results of Reuse and Khanna have to be ascribed to the different treatment of the electronic interactions and not to differences in geometry or interatomic distances. Desmarais et al.[78] have studied Ni_7 and Ni_8 with the same technique as Reuse and Khanna.[63] The magnetic moment in the ground state of Ni_7 (capped octahedron) is $\bar{\mu} = 1.14\ \mu_B$/atom, and the same value was obtained for all the low-lying isomers (pentagonal bipyramid, tricapped tetrahedron, and capped trigonal prism). The same effect was found for Ni_8. In this case a moment $\bar{\mu} = 1.0\ \mu_B$/atom was obtained for the ground state (bisdisphenoid) and all its low-lying isomers. This insensitivity of the magnetic moment to atomic structure in Ni_7 and Ni_8, also found in calculations for Ni_4,[63] is striking.

Reddy et al.[70] have used DFT to calculate the magnetic moments of Ni_N up to $N = 21$. For N less than or equal to 6, they employed ab initio geometries (discussed above). For N larger than 6, the geometries were those optimized by Nayak et al.[225] with the Finnis−Sinclair potential.[77] Compared to the experimental moments of Figure 9, the calculation of Reddy et al. predicts substantially smaller moments and important discrepancies occur in the detailed variation of $\bar{\mu}$ with N: for instance, Ni_6 and Ni_{13} are not local minima in the calculation. Those strong discrepancies are surprising. Reddy et al. discussed the possible sources and concluded that the cluster temperature may be at the heart of the problem, as the validity of the superparamagnetic model used to fit the experiment depends on the cluster temperature. This may not be the only reason for the discrepancies between experiment and DFT calculations as the TB results in Figure 9 accurately reproduce the qualitative behavior of $\bar{\mu}$ for N up to 16.

The "local" magnetic moments at different cluster sites were studied by Fujima and Yamaguchi[238] using the spin-polarized discrete variational $X\alpha$ method (in an LCAO framework). In this method the exchange-correlation energy is given by (in Hartree atomic units)

$$E_{xc} = -3\alpha\left(\frac{3}{4\pi}\right)^{4/3}\int[\rho_\uparrow(\mathbf{r})^{4/3} + \rho_\downarrow(\mathbf{r})^{4/3}]d\mathbf{r} \quad (57)$$

where $\rho_\sigma(\mathbf{r})$ denotes the spin ($\uparrow$ or $\downarrow$) density at $\mathbf{r}$ and $\alpha = 0.7$ for Ni. fcc structures and bulk interatomic distances were assumed, with an octahedron and a cuboctahedron for the shapes of Ni_{19} and Ni_{55}, respectively. The local magnetic moments were estimated by the unpaired 3d electron component at each atomic site, calculated by the Mulliken population analysis. There are no significant differences between the moments of atoms at different surface sites, and the moments of atoms of the layer immediately below the surface are smaller by $\sim$0.2 μ_B. The average magnetic moments $\bar{\mu}(Ni_{19}) = 0.58\ \mu_B$ and $\bar{\mu}(Ni_{55}) = 0.73\ \mu_B$ are significantly lower than the measured ones. A similar approach was followed by Pacchioni et al.,[237] who calculated the electronic structure of Ni_6, Ni_{13}, Ni_{19}, Ni_{38}, Ni_{44}, Ni_{55}, Ni_{79}, and Ni_{147} by an all-electron linear combination of Gaussian orbitals (LCGO) method with the exchange-correlation effects described by the $X\alpha$ method ($\alpha = 0.7$). The structures were assumed icosahedral (Ni_{13}, Ni_{55}, Ni_{147}) or with O_h symmetry (Ni_6, Ni_{13}, Ni_{19}, Ni_{38}, Ni_{44}, Ni_{55}, Ni_{79}; in most cases fragments of an fcc lattice). The first-neighbors distances were fixed at the bulk Ni−Ni separation of 2.49 Å, which is mandatory for large clusters. Even for the largest cluster, convergence of the binding energy and average magnetic moment to the bulk limit was not observed: the atoms of the two most internal shells in Ni_{147} have local magnetic moments still well below the bulk value. On the other hand, the width of the 3d band is almost converged for $N = 40-50$. The DFT calculations performed up to now for Ni clusters are few and mostly for small clusters. One hopes to see more studies in the future, especially for large clusters. In the meantime the detailed variation of $\bar{\mu}$ with N for Ni clusters is still an open problem that can only be solved with a careful and consistent treatment of both the geometrical structure (which requires a full minimization of the total energy) and the "self-consistent" electronic structure.

Fujima and Yamaguchi[238] also studied Fe and Cr clusters with $N = 15$ and 35 assuming a bcc structure: a rhombic dodecahedron. A low value of μ at layer 2 is obtained for Fe. The empirical magnetic shell model of Billas et al.[185,186] also gives a decrease at layer 2 for Ni and Fe clusters (see section VIII.C above). For Cr, an alternation of the signs of the local moments as a function of the distance to the cluster center is obtained; the absolute values $|\mu|$ of the local moments decrease with increasing local coordination and also decrease for decreasing interatomic distance. This sensitivity was also predicted earlier by Lee et al.[239] For Fe clusters, in contrast, the local moments are less sensitive to local atomic coordination. The DFT calculations of Cheng and Wang[113] also show that the Cr clusters are antiferromagnetic, and the dimer growth route discovered by these authors (see section IV.E) leads to the prediction of an odd−even alternation of the average moment: small magnetic

moments for the even-N clusters and large moments for the odd ones. The large moments arise from the quasiatomic character of the capping atoms; the dimer-paired even-N clusters have low $\bar{\mu}$ because of the strong intradimer 3d−3d interaction. In most cases, the calculated moments are within the experimental limit of 0.77 μ_B imposed by the experiments of Douglass et al.[240] But for Cr_{12} and Cr_{13}, the predicted $\bar{\mu}$ is larger than this limit, especially for C_{12} ($\bar{\mu}$ = 1.67 μ_B). This discrepancy waits to be resolved.

The properties of Mn are peculiar. In the bulk it has the smallest bulk modulus and cohesive energy of the 3d metals and the most complex lattice structure, with several allotropic forms. Some of its bulk phases are antiferromagnetic, while monolayers[241] and supported Mn clusters[242] exhibit nearly degenerate ferromagnetic and antiferromagnetic states. The bond length of the dimer, 6.43 au,[243] is larger than the nearest-neighbor distance in the bulk, in contrast to all other transition metals. Mn_2 is considered close to a van der Waals molecule,[243] with an estimated very small binding energy between 0.1 and 0.6 eV.[244] This character arises from the electronic configuration of the atom, $3d^5 4s^2$, in which the electrons of the half-filled 3d shell are more localized compared to other 3d atoms and do not interact with those of the other atom, and consequently the binding in Mn_2 arises from the weak interaction between the filled 4s shells. A nonmetal to metal transition is expected for clusters of a certain critical size. From an analysis of the reactivity of Mn_N clusters with hydrogen, Parks et al.[245] have suggested that this transition occurs at $N = 16$, although the ionization potential does not display any special feature (such as an abrupt change) at that size.[246]

The most interesting expectations arise from the large magnetic moment (5 μ_B) of the free atom. Since the interaction between the atoms in Mn_2 and in other small clusters is believed to be weak, one can expect that the magnetic moments would retain their free atomic character. If these moments would couple ferromagnetically, a Mn_N cluster would carry a "large" moment of 5 $N\mu_B$, which is remarkable. The only experiments measuring the magnetic moments are for small Mn clusters embedded in matrices. Electron spin paramagnetic resonance (ESR) studies of Mn_2 in inert-gas matrices yield an antiferromagnetic configuration but charged Mn_2^+ is ferromagnetic with a total magnetic moment of 11 μ_B.[247] Mn_5 also embedded in inert-gas matrices has a moment of 25 μ_B,[243] although the cluster could be larger. Mn_4 in a silicon matrix appears to have a moment of 20 μ_B.[248] Why Mn_2 is antiferromagnetic while the other clusters are ferromagnetic is not yet explained.

An early approximate Hartree−Fock calculation by Nesbet[249] obtained for Mn_2 a $^1\Sigma_g^+$ ground-state resulting from antiferromagnetic coupling of the localized spins. The predicted value of the Heisenberg exchange energy parameter was small and negative, $J = -4.1$ cm^{-1}. The ESR measurements for Mn_2 isolated in inert gas matrices performed several years later,[243,250] as well as optical absorption and magnetic circular dichroism experiments,[251] gave values of J in the range of -8 to -10 cm^{-1}, consistent with the prediction of Nesbet. Fujima and Yamaguchi[252] studied Mn_N with $N = 2-7$ using the discrete variational− $X\alpha$−LCAO method. The interatomic distances were optimized within constrained geometries. All the clusters were reported to show antiparallel spin ordering. Nayak and Jena[253] have optimized the equilibrium geometries for $N \leq 5$ at two levels of approximation: LSDA and the generalized gradient approximation (GGA). The calculated bond length and binding energy of Mn_2 are very sensitive to the treatment of exchange and correlation, and only the GGA calculations at the B3LYP level[254,255] are able to explain some of the experimental results (the calculated bond length is 6.67 au and the binding energy 0.06 eV). The B3LYP is a hybrid method that includes a part of the Hartree−Fock exchange calculated via the Kohn−Sham orbitals. The use of diffuse functions in the basis was found to be crucial to yield a weakly bonded molecule. However, Mn_2 is predicted to be ferromagnetic with a magnetic moment of 10 μ_B. After ionization to yield Mn_2^+, the binding energy increases and the bond length decreases, since the electron is removed from an antibonding orbital. The results for Mn_2^+ are less sensitive to the level of exchange and correlation. Its total magnetic moment is 11 μ_B, in agreement with the estimation from experiments for clusters in rare-gas matrices.[247] The predicted geometries of Mn_N, N = 3, 4, and 5 are compact: equilateral triangle, Jahn−Teller-distorted tetrahedron, and trigonal bipyramid, respectively. The strength of the bonding increases significantly with respect to the dimer (0.25, 0.50, and 0.55 eV/atom for N = 3, 4, and 5, respectively) due to s−d hybridization, although it remains small compared to other transition-metal clusters. The ground-state geometries are consistent with experiments in matrices. Ludwig et al.[248] have studied Mn_4 embedded in a solid silicon matrix and observed a hyperfine pattern of 21 lines, indicating that the four atoms are equivalent, consistent with a tetrahedral structure with the Mn atoms probably in interstitial sites. The triangular bipyramid is one of the possible structures of Mn_5 consistent with the ESR experiments of Baumann et al.[243] The calculated interatomic distances decrease substantially from Mn_2 to Mn_3, which indicates the onset of delocalization and hybridization between atomic orbitals at various sites. The calculated ionization potentials have values within 0.5 eV of the measured ones.[246] But the most striking property of these clusters in their ability to retain their atomic moments. Mn_3, Mn_4, and Mn_5 in their ground state are ferromagnetic, with moments per atom $\bar{\mu} = 5$ μ_B in the three cases (low-lying isomers are also ferromagnetic and with large magnetic moments). These large magnetic moments put small Mn clusters in a special place within the transition-metal series and give expectations for using those molecular magnets in future high-density information storage technology. Experiments should be welcome to confirm this extraordinary behavior. Calculations for monolayers[241] and supported clusters[242] lead to the same conclusion, and recent experiments seem to bear out the possibility of large

moments.[256,257] Experiments on free Mn_2 may clarify the discrepancy between experiment (on matrices) and theory concerning the magnetic character of this cluster.

Recent DFT calculations by Pederson et al.[258] give further insight on this discrepancy. They used LDA and GGA functionals[259] and performed a detailed study of Mn_2. Their conclusion is that this dimer is ferromagnetic with a total moment $\mu = 10\ \mu_B$ (equilibrium separation of 4.93 au and binding energy of 0.99 eV). An antiferromagnetic state was also found with lower binding energy (0.54 eV) and larger bond length (5.13 au). Evidently, the characteristics of this isomer are closer to those of Mn_2 in matrices. One could blame the discrepancy on some misrepresentation of correlation effects by the GGA. Pederson and co-workers have argued that self-interaction corrections (SIC) will not change matters, and then one is led to trust the DFT result. A plausible explanation of the discrepancy is, according to these workers, that the ferromagnetic state is the true ground state of free Mn_2 but that the van der Waals interactions between this cluster and the matrix may stretch the bond, leading to the appearance of the antiferromagnetic state in the embedded cluster. Apart from the two states discussed, other metastable states were found with different magnetic moments and cohesive energies: for these the bond length decreases monotonically as the net moment decreases. Larger clusters were also studied. Mn_3 also has close magnetic states. The ground state is a isosceles triangle in a ferromagnetic state (total moment of 15 μ_B), and a frustrated antiferromagnetic solution also exits with the atomic d spins of the shorter side of the triangle ferromagnetically coupled while the third atom is antiferromagnetically coupled to the other two. This state, with a net moment of 5 μ_B, is only 0.014 eV less stable than the ground state. In addition, the triangle is very close to equilateral. Mn_4 was found to be a tetrahedron with total moment 20 μ_B, that is 5 μ_B/atom. For the intriguing case of Mn_5, the calculation predicts a trigonal bipyramid with a net spin of 23 μ_B, lower than the measured moment of 25 μ_B. Trigonal bipyramid and square pyramid states with a moment of 25 μ_B are high in energy: 0.62 and 1.20 eV above the ground state, respectively. This led Pederson to conclude that either the matrix influences the ground-state multiplicity of Mn_5 or the cluster formed in the experiment is one other than Mn_5; this later possibility had also been admitted by Bauman et al.[243] A square bipyramid and a pentagonal pyramid were investigated for Mn_6. The total moments are 26 and 28 μ_B, respectively, and the second structure is less stable by 1.6 eV. The electron affinity of the square bipyramid is large (1.36 eV), and Mn_6^- was proposed as a possible candidate for the 25 μ_B cluster observed in the ESR experiments. The structure of Mn_7 is formed by two eclipsed triangles with a single atom cap (C_{3v} symmetry). The ionization energy $I = 5.51$ eV is in good agreement with the recent measurement of Koretsky and Knickelbein,[246] who found $I = 5.44$ eV. The geometry of Mn_8 is complex. To summarize the results, Table 3 gives the average bond distance, number of bonds per atom, average magnetic moment per atom and binding energy for Mn_2−Mn_8. Also given are the two spin gaps $\Delta_1 = \epsilon_{HOMO}^{majority} - \epsilon_{LUMO}^{minority}$ and $\Delta_2 = \epsilon_{HOMO}^{minority} - \epsilon_{LUMO}^{majority}$. These represent the energy required to move an infinitesimal amount of charge from the HOMO of one spin to the LUMO of the other. The two spin gaps have to be positive for the system to be magnetically stable.

Table 3. Average Bond Distance *d*, Number of Bonds per Atom N_B, Magnetic Moment per Atom $\bar{\mu}$, and Binding Energy per Atom E_b for Mn_N as a Function of *N*, in addition to Spin Gaps $\Delta_1 = \epsilon_{HOMO}^{majority} - \epsilon_{LUMO}^{minority}$ and $\Delta_2 = \epsilon_{HOMO}^{minority} - \epsilon_{LUMO}^{majority}$

N	*d* (au)	N_B	$\bar{\mu}$ (μ_B)	E_b (eV/atom)	Δ_1 (eV)	Δ_2 (eV)
2	4.927	0.5	5.0	0.50	0.65	1.30
3	5.093	1.0	5.0	0.81	0.46	1.38
4	5.162	1.5	5.0	1.19	0.62	2.31
5	5.053	1.8	4.6	1.39	0.50	0.79
6	5.002	2.0	4.3	1.56	0.90	1.13
7	4.970	2.1	4.2	1.57	0.70	0.47
8	4.957	2.2	4.0	1.67	0.93	0.37

An interesting topic deserving to be mentioned here is the change in the electronic structure of a transition-metal cluster when a ligand shell is added. The ligand molecules induce perturbations on the electronic structure of the atoms on the surface of the cluster.[260] A striking effect is the almost complete quenching of the magnetic moments of the surface atoms in large Ni clusters by CO ligands, demonstrated by experimental magnetization studies and DFT calculations.[261] The explanation is that ligands with σ-lone pairs, like CO, interact repulsively with the diffuse 4sp electrons of the Ni atoms inducing a configurational transition $3d^9 4s^1 \rightarrow 3d^{10}$ that fills the 3d shell. The calculations show that this repulsive destabilization is produced even by a shell of He atoms.[237] DFT studies of NH_3 adsorption by Ni_N ($N = 1-4$) also indicate a significant effect on the magnetism of the Ni_N clusters.[262] Adsorption of NH_3 leads to a decrease of the Ni moments, which are completely quenched when the number of NH_3 units equals the number of Ni atoms. The nitrogen atom binds directly to a Ni atom, and the quenching of the magnetic moment of Ni occurs because the Ni−nitrogen bond distance is short. When the number of NH_3 molecules is larger than the number of Ni atoms, the Ni−nitrogen bonds are stretched due to steric hindrance, the Ni−nitrogen distances exceed the critical distance of 1.9 Å, and magnetism reappears.

XI. Magnetism in Clusters of 4d Elements

All the 4d metals are nonmagnetic in the equilibrium bulk phase. But, since the free atoms are magnetic due to Hund's rules, it should not be surprising that small clusters of some of the 4d elements are magnetic. Experiments[196] show that small Rh_N clusters with less than 60 atoms are magnetic, and Ru_N and Pd_N clusters with less than 12 atoms appear to be magnetic also. No experimental data are available for the other elements. Several calculations have investigated the magnetic properties of these clusters. Since the atomic structure is unknown, most of the calculations assumed model

structures. Zhang et al.[62] performed LCAO−molecular orbital calculations within the frame of the DFT formalism. The clusters had six atoms in octahedral symmetry, and the most interesting feature of this work is that a systematic study of trends was done across the whole 4d period: namely, for Y_6, Zr_6, Nb_6, Mo_6, Tc_6, Ru_6, Rh_6, Pd_6, Ag_6, and Cd_6. The clusters were allowed to relax radially. The general binding trends have been discussed in section III. The calculated magnetic moments per atom are given in Table 1. Each cluster, except Y_6, Pd_6, and Cd_6, has a finite magnetic moment, and the largest moments occur for Ru_6 and Rh_6 (1.00 and 0.99 μ_B, respectively). The picture is different compared to the bulk metals. To understand the large moments of Ru_6 and Rh_6, Zhang et al. plotted the total density of states, which is characterized by having a large peak in the energy region of the Fermi level. This high DOS contributes strongly to the large moments because a small shift between up and down spin subbands (exchange splitting) results in a sizable difference between the population of up and down spin electrons. In fact Ru_6, Rh_6, and Nb_6 have the largest exchange splittings across the 4d period (splittings of the order of 0.5 eV for the sp band and 0.7 eV for the d band). In contrast, the Fermi levels of the bulk metals lie in a dip of DOS. The main contribution to the DOS of the occupied valence band of the clusters is from d electrons. This gives support to some models in which the sp electrons are altogether neglected. There are two factors which contribute to the large DOS near ϵ_F. First, the valence bandwidth of the cluster is narrower than in the solid due to the reduced atomic coordination. The narrower band results in a higher DOS. Second, the high symmetry (octahedral) assumed in the model enhances the degeneracies. The last effect, however, suggests that some of the magnetic moments of Table 1 may be overestimated.

The experiments for Rh clusters reveal an interesting oscillatory pattern of $\bar{\mu}$(N), with large values for $N = 15-16$ and 19 and drops for $N = 13-14$, 17−18, and 20, and for this reason a number of calculations have been performed, some of them using the LSDA. In those studies only a few cluster sizes were considered and highly symmetric structures were assumed, except for the very small ones. Galicia,[263] Reddy et al.,[264] and Piveteau et al.[265] have studied Rh_{13}, concluding that it is magnetic. Jinlong et al.[266,267] studied clusters with $N = 2-8$, 10, 12, 13, 19 and Li et al.[268] clusters with $N = 6$, 9, 13, 19, 43. The clusters are magnetic at $T = 0$ K, in qualitative agreement with experiment. However, the results for $\bar{\mu}$ show a lot of dispersion. Taking Rh_{13} as an example, the predicted magnetic moments are 0.69,[268] 1.00,[263] 1.15,[266] 1.62,[264] and 1.69 μ_B.[265] This is not surprising for a system showing weak, non saturated itinerant magnetism for which it is known that the magnetic behavior is very sensitive to the details of the local atomic environment and of the electronic structure.[140,234,269]

The self-consistent TB method has been employed by Villaseñor-González et al.[270] to study several Rh_N clusters in the range $9 \leq N \leq 55$, namely, $N = 9$, 11, 13, 15, 17, 19, 20, 23, 27, 43, 51, and 55. Only the 4d electrons were included in the calculations and model structures (fcc-, bcc-, or icosahedral-like) were considered, although atomic relaxations preserving the cluster symmetry were allowed in order to optimize the cohesive energy (the necessary repulsive Born−Mayer pair potential was, of course, included). A twisted double-square pyramid was also studied for Rh_9. Important bond length contractions were obtained (2−9% contraction with respect to the bulk bond length). These contractions strongly affect the magnetic moments: for instance, for fcc Rh_{13} with bulk bond distances, $\bar{\mu} = 1.56\ \mu_B$ while the value for the optimized bond length (3% contraction) is $\bar{\mu} = 0.78\ \mu_B$. The last value is in much better agreement with experiment. A strong sensitivity of the magnetic state with bond distance was also obtained by Minemoto[105] for V_4^+ using DFT. The calculated $\bar{\mu}$(N) of Rh_N oscillates as a function of N and tends to decrease with increasing N. The twisted double-square pyramid yields the largest cohesive energy for Rh_9 (2.38 eV/atom), and its moment $\bar{\mu} = 0.66\ \mu_B$ is in good agreement with experiment ($\bar{\mu} = 0.8 \pm 0.2\ \mu_B$). For Rh_{11} the icosahedral structure and a fcc structure are degenerate ($E_b = 2.43$ eV/atom), although only the magnetic moment of the former isomer ($\bar{\mu} = 0.73\ \mu_B$) is consistent with experiment ($\bar{\mu} = 0.8 \pm 0.2\ \mu_B$). The most stable structure for Rh_{13} is bcc, with $\bar{\mu} = 0.62\ \mu_B$, in better agreement with experiment ($\mu = 0.48 \pm 0.13\ \mu_B$) than the other alternative structures considered. In the range $15 \leq N \leq 43$ the structures are predicted fcc, and although the magnetic moments are systematically larger than the measured ones, the trends in the size dependence are correctly reproduced: local minima at $N = 13$ and 17 and maxima at $N = 15$ and 19. This suggest that the underlying structure in the range $15 \leq N \leq 20$ could be fcc-like. Furthermore, the other structures fail to reproduce those oscillations. Finally, the icosahedral structure is more stable for $N = 55$, and its non magnetic nature is also in better agreement with experiment. In summary, the structures predicted to be more stable by the TB calculation give a consistent agreement with the measured magnetic moments.

Villaseñor-González et al. also studied the distribution of local magnetic moments in the clusters. The bcc isomers order ferromagnetically and the local atomic moments tend to increase from the cluster center to the surface. Compact structures (fcc and icosahedral) are more complex, and the magnetic order is sometimes antiferromagnetic-like, with $\bar{\mu}$ changing sign between adjacent shells. A similar behavior has been predicted for fcc Rh surfaces and thin films.[271] Finally, the effect of the sp electrons was analyzed for Rh_{13}. The main conclusion was that the sp electrons provide a sizable contribution to the binding energy (≃3.2 eV/atom for Rh_{13}). However, the bond length contractions and the relative stabilities between isomers were not significantly changed, neither was the total magnetic moment, although the local moments are more sensitive to sp−d hybridization. Similar results were obtained by Guirado-López et al.[272] in their TB study of Rh_N ($N = 13$, 19, 43, 55, and 79) with fcc structure. Ferromagnetic order was found for Rh_{13}, Rh_{19}, and Rh_{43} and antiferromagnetic

configurations for Rh_{55} and Rh_{79}, in agreement with Villaseñor-González et al..[270] The magnetic moments for the larger clusters are very close to experiment, and this was interpreted as an indication that fcc structures could be preferred for $N > 40$. The high sensitivity of the results to atomic relaxation was also noticed. The magnetic−nonmagnetic transition was estimated to be located at $N_c \approx 80$.

The relationship between the magnetism, topology, and reactivity of Rh clusters has been studied by Nayak et al.[273] These authors have found that different isomers can have different magnetic structures, and these isomers can lead to different chemical reactivities. The studied case, using DFT techniques (at the nonlocal GGA level), was Rh_4. This cluster has two isomers: the ground state is a tetrahedron with a binding energy of 2.41 eV/atom. The second isomer, a square, is only 0.60 eV/atom less stable. Despite these two being close in energy, the tetrahedron is nonmagnetic and the square is magnetic with a moment of 1 μ_B/atom. In contrast, Ni_4 also has two nearly degenerate isomers (again the tetrahedron and the square) but the average magnetic moments per atom are the same. As already discussed, the two effects that tend to control the magnetic moment are coordination and interatomic distance: increasing interatomic distance and decreasing coordination leads to an enhancement of the magnetic moments since both factors tend to reduce the electron wave function overlap. The coordination in the tetrahedron (3) is larger than in the square (2). On the other hand, nearest-neighbor interatomic distances are only 0.1 Å larger, so the vanishing of the magnetic moment seems to be associated to the enhanced coordination. More insight is obtained from the analysis of the distribution of orbital energy levels. The square geometry of Rh_4 has a larger number of states near the HOMO, and it is known from extended systems that a large density of states near the Fermi energy usually leads to magnetic structures. By allowing the two Rh_4 isomers to react with H_2, the following conclusions were noted: (1) H_2 dissociates and binds atomically to both isomers; (2) the binding energy of H_2 to the nonmagnetic isomer is larger by a factor of 2; (3) the spin multiplicity of both isomers changes. This indicates that the reactivity of transition-metal clusters may depend sensitively of their magnetic structure and topology. In fact, the existence of isomers has been detected in reactivity experiments.[74,172,274] Only one of the forms of pure Rh_4, the magnetic one, can be deflected in a Stern−Gerlach magnet. On the other hand, the two reacted forms of Rh_4H_2 are magnetic with different spin multiplicities. Consequently, the two reacted clusters will be deflected differently in a Stern−Gerlach field. This provides a possible way to test the theoretical predictions.

TB[270,275] and DFT calculations[264,276] have been performed for Ru clusters. The TB method predits lower average magnetic moments, in better agreement with the experimental upper limits,[196] but one has to bear in mind that the sp electrons were not included in the TB calculations. The magnetic−nonmagnetic transition is estimated at $N_c \approx 19$, a value in satisfactory agreement with the experimental result ($N_c \geq 13$).[196] Antiferromagnetic alignment of the local moments is preferred for most of the structures studied. Similar arrangements have been found for Fe clusters; Fe is above Ru in the periodic table, so a correlation seems to exist between the magnetic properties of isoelectronic elements.

The magnetism of small palladium clusters is still controversial. It has not been confirmed in the experiments of Cox et al.,[196] but these authors did not exclude the possibility of magnetism and set upper limits of 0.40 μ_B/atom for Pd_{13} and 0.13 μ_B/atom for Pd_{105}. Lee[277] has performed DFT calculations, using a linear combination of Gaussian orbitals, to study the possible magnetism of Pd clusters with restricted symmetrical fcc and bcc structures. Pd_{19} was modeled as a central atom surrounded by its 12 first nearest neighbors and 6 second nearest neighbors in an fcc configuration (the structure of bulk Pd). By varying the lattice constant and the magnetic moment, Lee found a lowest energy state with lattice constant of 7.42 au (identical to that found in DFT calculations of bulk Pd)[61] and a magnetic moment $\bar{\mu} = 0.32$ μ_B/atom. A nonmagnetic state, with lower binding energy was also found. To confirm the possibility of magnetism, Pd_{15} with a bcc structure (central atom with its 8 first nearest neighbors and 6 second nearest neighbors) was also studied. For a lattice constant of 5.83 au, such that the volume per atom is the same as for bulk fcc palladium, only one state, magnetic in fact, was found. The calculated moment was 0.53 μ_B/atom. A previous calculation for fcc Pd_{13} by the same author[278] gave two states with magnetic moments $\bar{\mu} = 0.0$ and 0.46 μ_B/atom. In summary, Lee's calculations support the possibility of small magnetic moments in palladium clusters.

XII. Noncollinear Magnetism in Iron Clusters

The γ phase of bulk iron exhibits a spin−spiral structure.[279,280] Noncollinear magnetic configurations occur easily in low-symmetry systems and in disordered ones.[281,282] One can then expect noncollinear spin configurations in clusters of transition metals. However, the usual DFT(LSDA) calculations described in previous sections assume spin alignment through the system. Generalized LSDA calculations allowing for noncollinear magnetic structures have been performed for solids,[280,283−286] and Car and coworkers[287] have extended this idea to Fe clusters. They have combined a LSDA scheme in which the direction of the magnetization is fully unconstrained as a function of position with the ab initio molecular dynamics method.[35] In the LSDA,[288] the one-electron states are described by two-component spinors $\Psi(\mathbf{r}) = (\phi_1(\mathbf{r}), \phi_2(\mathbf{r}))$. The density matrix is defined

$$\Gamma_{\alpha\beta}(\mathbf{r}) = \sum_i f_i \phi_{\alpha i}(\mathbf{r}) \phi^*_{\beta i}(\mathbf{r}) \qquad (58)$$

where α and β are spin indices and f_i is the occupation number of the ith single-particle state. The density

matrix can be written as

$$\Gamma(\mathbf{r}) = \frac{1}{2}\rho(\mathbf{r})\sigma_0 + \frac{1}{2}\sum_k m_k(\mathbf{r})\sigma_k \qquad (59)$$

where $\rho(\mathbf{r})$ is the charge density, σ_0 is the unit matrix, σ_k ($k = x, y, z$) are the Pauli spin matrices, and $m_k(\mathbf{r})$ are the Cartesian components of the spin-density vector $\boldsymbol{m}(\mathbf{r})$. In this scheme the spin quantization axis of each state can vary with position.

Following the ab initio MD scheme,[35] the electronic wave functions $\{\Psi_i\}$ and the atomic positions $\{\boldsymbol{R}_i\}$ are simultaneously optimized by minimizing the total energy for noncollinear spin structures.[288,289] Ultrasoft pseudopotentials[290] were used including the 3s and 3p states of Fe into the valence group. The ultrasoft pseudopotentials make the calculations as accurate as the all-electron calculations.[291] The magnetic moment of each atom in the clusters was estimated by integrating the spin density within spheres of radius 1.7 au centered on the atoms. The ground state of Fe_5 is a D_{3h} structure (trigonal bipyramid) with a noncollinear spin arrangement. The three atoms of the basal plane (*xy*-plane) have atomic moments of 2.72 μ_B pointing in the same direction (*taken* as the *z* direction; spin−orbit effects are not included) and the two apical atoms have moments of magnitude 2.71 μ_B, tilted in opposite directions by approximately 30° with respect to the moments of the basal atoms. The binding energy of this cluster is E_b = 3.46 eV/atom, and its total moment is 14.57 μ_B. An isomer with the D_{3h} structure was found having a collinear arrangement, with atomic moments of 2.58 μ_B and 2.55 μ_B for the basal and apical atoms, respectively. The binding energy is E_b = 3.45 eV/atom, only 0.01 eV/atom above the ground state. For Fe_3, a linear structure with a noncollinear arrangement was found: the central atom has a moment 1.27 μ_B oriented perpendicularly to the linear axis and the two edge atoms have moments of magnitude 2.89 μ_B, tilted by ±10° with respect to the cluster axis. The total moment of this cluster is 2.04 μ_B, and its binding energy is E_b = 2.17 eV/atom. However, this is not the ground state of Fe_3. The ground state is an equilateral triangle with collinear arrangement. Its total moment is 8.00 μ_B and its binding energy E_b = 2.64 eV/atom. Linear ($D_{\infty h}$) isomers were also found with collinear antiferromagnetic (AF) and ferromagnetic (AF) spin configurations. The total moments of these two isomers are 0.00 μ_B and 6.00 μ_B and their binding energies 2.15 eV/atom and 1.80 eV/atom, respectively. One can notice that collinear states exist both in Fe_3 and Fe_5 with the same geometries of the noncollinear states, although with slightly smaller binding energies. Those collinear states also have lower magnetic moments and, on average, slightly shortened bonds. The magnetic energy associated with larger magnetic moments appears to favor noncollinear spin configurations. It should be stressed, nevertheless, that the ground state of Fe_3 is collinear. Calculations for Fe_2 and Fe_4 also gave collinear ground states. A comparison of the atomic and magnetic structures, binding energies, and magnetic moments is given in Table 4.

Table 4. Atomic and Magnetic Structure, Binding Energy, and Total Magnetic Moment of Different Isomers of Fe Clusters[287]

	atomic structure	magnetic structure	E_b (eV/at)	μ (μ_B)
Fe_2	$D_{\infty h}$	collinear(F)	2.06	6.00
Fe_3	D_{3v}	collinear(F)	2.64	8.00
	$D_{\infty h}$	noncollinear	2.17	2.04
	$D_{\infty h}$	collinear(AF)	2.15	0.00
	$D_{\infty h}$	collinear(F)	1.80	6.00
Fe_4	D_{2d}	collinear(F)	3.13	12.00
	T_d	collinear(F)	3.12	12.00
Fe_5	D_{3h}	noncollinear	3.46	14.57
	D_{3h}	collinear(F)	3.45	14.00

XIII. Summary

The recent literature investigating the relation between electronic structure, atomic structure, and magnetism of clusters of transition elements (with d electrons) has been reviewed. Theoretical work is mainly described as a tool to provide a microscopic explanation of the results of experiments.

The most interesting characteristic of clusters is that the values of their properties vary with the cluster size *N* in an unsmooth way, sometimes having oscillations whose amplitude decays for increasing *N*. Those oscillations can have an electronic origin, as is the case for the noble-metal elements Cu, Ag, and Au, which have the d shells filled, and the oscillations reveal the formation, by the outermost s electrons of the atoms, of electronic orbitals extended over the whole cluster volume. Abrupt jumps in the values of many properties are associated to the filling of those delocalized electronic shells. A second type of oscillation is linked to purely geometrical effects. Experiments measuring the adsorption of weakly reactive molecules on the surface of the clusters, as well as Stern−Gerlach-type measurements of the magnetic moments, suggest a growth mode by the formation of successive atomic layers. In one of the best studied systems, Ni_N, the growth appears to occur by forming layered icosahedral structures. Again, clusters forming perfect icosahedra are special. The icosahedral growth model is supported by theoretical calculations for small clusters. However, only for small clusters can one use the full power of ab initio methods, especially DFT theory, to determine the geometrical structure. For others, medium and large size clusters, effective many-atom potentials are used instead. The icosahedral growth can follow two different routes, labeled as TIC and MIC routes (see section VII), that correspond to two different ways of covering the surface of a perfect icosahedron, and the theoretical calculations employing a semiempirical many-atom potential predict a TIC−MIC transition at Ni_{27}−Ni_{28} (during the icosahedral growth from Ni_{13} to Ni_{55}) and at Ni_{74} (during the growth from Ni_{55} to Ni_{147}). These transitions explain a number of detailed observations concerning the absorption of N_2 molecules. Icosahedral growth is consistent with the positions of the minima of the average magnetic moment per atom (as a function of *N*) measured in Stern−Gerlach

experiments for Ni_N. However, the positions of the maxima are difficult to explain and remain as an open question.

The main trends in the behavior of the magnetic moment of the transition-metal clusters can be understood as a consequence of two main factors. The first is the atomic coordination, which affects the local moments and consequently the average cluster moment. A larger local atomic coordination widens the local density of electronic states, decreasing the local magnetic moments. The second factor is the nearest-neighbor separation. Large nearest-neighbor distances decrease wave function overlap and maintain the local magnetic moments closer to the values in the free atoms. Due to the interplay of these two factors, some clusters have been found (or predicted) to be magnetic even if the same element is nonmagnetic in the bulk metallic phase.

XIV. Acknowledgments

This work has been supported by DGES (Grant PB95-0720-C02-01) and Junta de Castilla y León (Grant VA 28-99). I acknowledge the hospitality and support by the Physics Department of Queen's University, Canada, where part of this work was done.

XV. References

(1) Alonso, J. A.; March, N. H. *Electrons in Metals and Alloys*; Academic: London, 1989.
(2) Alonso, J. A.; Balbás, L. C. In *Topics in Current Chemistry*; Nalewajski, R. F., Ed.; Springer, Berlin 1996; Vol. 182 (Density Functional Theory III), p 119.
(3) de Heer, W. A.; Knight, W. D.; Chou, M. Y.; Cohen, M. L. *Solid State Phys.* **1987**, *40*, 93.
(4) Walch S.; Bauschlicher, C. W. In *Comparison of Ab initio Quantum Chemistry with Experiment for Small Molecules*, The State of the Art; Bartlett, R., Ed.; Reidel: Dordrecht, 1985; p 17.
(5) Shim, I. In *Sixteen Research Reports by the Niels Bohr Fellows of the Royal Danish Academy of Sciences and Letters on the Centenial of Niels Bohr*; The Royal Danish Academy of Sciences and Letters: Copenhagen, 1985; p 147.
(6) Jarrold, M. F. *J. Phys. Chem.* **1995**, *99*, 11. Bowers, M. T. *Acc. Chem. Res.* **1994**, *27*, 324.
(7) Berkowitz, A. E. *IEEE Trans. Magn.* **1986**, *22*, 466.
(8) Schmid, A. E. *Chem. Rev.* **1991**, *92*, 1709.
(9) Freeman, A. J.; Li, C.; Wu, R. Q. In *Science and Technology of Nanostructured Magnetic Materials*; Hadjipanayis, G. C., Prinz, G. A., Eds.; NATO Advanced Study Institutes Series B; Plenum: New York, 1991; Vol. 259, p 1.
(10) Harrison, W. A. *Electronic Structure and the Properties of Solids*; Freeman: San Francisco, 1980.
(11) Knight, W. D.; Clemenger, K.; de Heer, W. A.; Saunders, W. A.; Chow, M. Y.; Cohen, M. L. *Phys. Rev. Lett.* **1984**, *52*, 2141.
(12) Schmidt, M.; Kusche, R.; von Issendorff, B.; Haberland, H. *Nature* **1998**, *393*, 238.
(13) Kohn, W.; Sham, L. J. *Phys. Rev.* **1965**, *140*, A1133. Hohenberg, P.; Kohn, W. *Phys Rev.* **1964**, *136*, B864.
(14) *Theory of the Inhomogeneous Electron Gas*; Lundqvist, S., March, N. H., Eds.; Plenum: New York, 1983.
(15) Ekardt, W.; Penzar, Z. *Phys. Rev. B* **1988**, *38*, 4273.
(16) Penzar, Z.; Ekardt, W. *Z. Phys. D* **1990**, *17*, 69.
(17) Kohl, C.; Montag, B.; Reinhard, P. G. *Z. Phys. D* **1995**, *35*, 37.
(18) Koskinen, M.; Lipas, P. O.; Manninen, M. *Europhys. Lett.* **1995**, *30*, 519.
(19) Katakuse, I.; Ichihara, T.; Fujita, Y.; Matsuo, T.; Sakurai, T.; Matsuda, H. *Int. J. Mass Spectrom. Ion Processes* **1985**, *67*, 229.
(20) Katakuse, I.; Ichihara, T.; Fujita, Y.; Matsuo, T.; Sakurai, T.; Matsuda, H. *Int. J. Mass Spectrom. Ion Processes* **1986**, *74*, 33.
(21) Knickelbein, M. B. *Chem. Phys. Lett.* **1992**, *192*, 129.
(22) Ganteför, G.; Gausa, M.; Meiwes-Broer, K. H.; Lutz, H. O. *J. Chem. Soc., Faraday Trans.* **1990**, *86*, 2483.
(23) Leopold, D. G.; Ho, J.; Lineberger, W. C. *J. Chem. Phys.* **1987**, *86*, 1715.
(24) Pettiette, C. L.; Yang, S. H.; Craycraft, M. J.; Conceicao, J.; Laaksonen, R. T.; Chesnovsky, O.; Smalley, R. E. *J. Chem. Phys.* **1988**, *88*, 5377.
(25) Cha, C. Y.; Ganteför, G.; Eberhardt, W. *J. Chem. Phys.* **1993**, *99*, 6308.
(26) Winter, B. J.; Parks, E. K.; Riley, S. J. *J. Chem. Phys.* **1991**, *94*, 8618.
(27) Balbás, L. C.; Rubio, A.; Alonso, J. A.; Borstel, G. *Chem. Phys.* **1988**, *120*, 239.
(28) Hoareau, A.; Melinon, P.; Cabaud, B. *J. Phys. D* **1985**, *18*, 173.
(29) Schulze, W.; Winter, B.; Urban, J.; Goldenfeld, I. *Z. Phys. D* **1985**, *4*, 379.
(30) Pettifor, D. *J. Phys. F* **1977**, *7*, 613.
(31) Williams, A. R.; Gelatt, C. D.; Janak, J. F. In *Theory of Alloy Phase Formation*; Bennet, L. H., Ed.; The Metallurgical Society of AIME: Warrendale 1980; p 40.
(32) Chesnovsky, O.; Taylor, K. J.; Conceicao, J.; Smalley, R. E. *Phys. Rev. Lett.* **1990**, *64*, 1786.
(33) Fujima, N.; Yamaguchi, T. *J. Phys. Soc. Jpn.* **1989**, *58*, 1334.
(34) Massobrio, C.; Pasquarello, A.; Car, R. *Chem. Phys. Lett.* **1995**, *238*, 215.
(35) Car, R.; Parrinello, M. *Phys. Rev. Lett.* **1985**, *55*, 2471.
(36) Massobrio, C.; Pasquarello, A.; Car, R. *Phys. Rev. Lett.* **1995**, *75*, 2104.
(37) Massobrio, C.; Pasquarello, A.; Car, R. *Phys. Rev. B* **1996**, *54*, 8913.
(38) Bauschlicher, W.; Langhoff, S. R.; Taylor, P. R. *J. Chem. Phys.* **1988**, *88*, 1041.
(39) Bauschlicher, W. *Chem. Phys. Lett.* **1989**, *156*, 91.
(40) Bauschlicher, W.; Langhoff, S. R.; Partridge, H. *J. Chem. Phys.* **1989**, *91*, 2412.
(41) Bauschlicher, W.; Langhoff, S. R.; Partridge, H. *J. Chem. Phys.* **1990**, *93*, 8133.
(42) Hay, P. J.; Wadt, W. R. *J. Chem. Phys.* **1985**, *82*, 299.
(43) Chong, D. P.; Langhoff, S. R. *J. Chem. Phys.* **1986**, *84*, 5606.
(44) Ahlrichs, R.; Scharf, P.; Ehrhardt, C. *J. Chem. Phys.* **1985**, *82*, 890.
(45) Koutecky, J.; Fantucci, P. *Chem. Rev.* **1986**, *86*, 539.
(46) Howard, J. A.; Sutcliffe, R.; Tse, J. S.; Mile, B. *Chem. Phys. Lett.* **1983**, *94*, 561.
(47) Howard, J. A.; Sutcliffe, R.; Mile, B. *J. Chem. Phys.* **1983**, *87*, 2268.
(48) Howard, J. A.; Sutcliffe, R.; Mile, B. *Surf. Sci.* **1985**, *156*, 214.
(49) Akeby, H.; Panas, I.; Petterson, L. G. M.; Siegbahn, P.; Wahlgren, U. *J. Phys. Chem.* **1990**, *94*, 5471.
(50) Panas, I.; Siegbahn, P. E. M.; Wahlgren, U. *Chem. Phys.* **1987**, *112*, 325.
(51) Müller, W.; Flesch, J.; Meyer, W. *J. Chem. Phys.* **1984**, *80*, 3297.
(52) Boustani, I.; Koutecky, J. *J. Chem. Phys.* **1988**, *88*, 5657.
(53) Bonacic-Koutecky, V.; Cespiva, L.; Fantucci, P.; Koutecky, J. *J. Chem. Phys.* **1993**, *98*, 7981.
(54) Bonacic-Koutecky, V.; Cespiva, L.; Fantucci, P.; Pittner, J.; Koutecky, J. *J. Chem. Phys.* **1994**, *100*, 490.
(55) Ho, J.; Ervin, K. M.; Lineberger, W. C. *J. Chem. Phys.* **1990**, *93*, 6986.
(56) Cleveland, C. L.; Landman, U.; Schaaff, T. G.; Shafigullin, M. N.; Stephens, P. W.; Whetten, R. L. *Phys. Rev. Lett.* **1997**, *79*, 1873.
(57) Michaelian, K.; Rendon, N.; Garzon, I. L. *Phys. Rev. B* **1999**, *60*, 2000.
(58) Garzon, I. L.; Michaelian, K.; Beltran, M. R.; Posada-Amarillas, A.; Ordejon, P.; Artacho, E.; Sanchez-Portal, D.; Soler, J. M. *Phys. Rev. Lett.* **1998**, *81*, 1600.
(59) Painter, G. S. *Phys. Rev. Lett.* **1993**, *70*, 3959.
(60) Kittel, C. *Introduction to Solid State Physics*; Wiley: New York, 1976.
(61) Moruzzi, V. L.; Janak, J. F.; Williams, A. R. *Calculated Electronic Properties of Metals*; Pergamon: New York, 1978.
(62) Zhang, G. W.; Feng, Y. P.; Ong, C. K. *Phys. Rev. B* **1996**, *54*, 17208.
(63) Reuse, F. A.; Khanna, S. N. *Chem. Phys. Lett.* **1995**, *234*, 77.
(64) Moskovits, M.; Hulse, J. E. *J. Chem. Phys.* **1977**, *66*, 3988.
(65) Morse, M. O.; Hansen, G. P.; Langridge-Smith, P. R. R.; Zheng, L. S.; Geusic, M. E.; Michalopoulos, D. L.; Smalley, R. E. *J. Chem. Phys.* **1984**, *80*, 5400.
(66) Ho, J.; Polak, M. L.; Ervin, K. M.; Lineberger, W. C. *J. Chem. Phys.* **1986**, *99*, 8542.
(67) Moskovits, M.; Dilella, D. P. *J. Chem. Phys.* **1980**, *72*, 2267.
(68) Walch, S. P. *J. Chem. Phys.* **1987**, *86*, 5082.
(69) Castro, M.; Jamorski, C.; Salahub, D. R. *Chem. Phys. Lett.* **1997**, *271*, 133.
(70) Reddy, B. V.; Nayak, S. K.; Khanna, S. N.; Rao, B. K.; Jena, P. *J. Phys. Chem. A* **1998**, *102*, 1748.
(71) Michelini, M. C.; Pis Diez, R.; Jubert, A. H. *Int. J. Quantum Chem.* **1998**, *70*, 693.
(72) Lian, L.; Su, C. X.; Armentrout, P. B. *J. Chem. Phys.* **1992**, *96*, 7542.
(73) Nayak, S. K.; Reddy, B.; Rao, B. K.; Khanna, S. N.; Jena, P. *Chem. Phys. Lett.* **1996**, *253*, 390.

(74) Parks, E. K.; Zhu, L.; Ho, J.; Riley, S. J. *J. Chem. Phys.* **1995**, *102*, 7377.
(75) Nygren, M. A.; Siegbahn, P. E. M.; Wahlgren, U.; Akeby, H. *J. Chem. Phys.* **1992**, *96*, 3633.
(76) Apsel, S. E.; Emmert, J. W.; Deng, J.; Bloomfield, L. A. *Phys. Rev. Lett.* **1996**, *76*, 1441.
(77) Finnis, M. W.; Sinclair, J. E. *Philos. Mag.* **1984**, *50*, 45.
(78) Desmarais, N.; Jamorski, C.; Reuse, F. A.; Khanna, S. N.; *Chem. Phys. Lett.* **1998**, *294*, 480.
(79) Reuse, F. A.; Khanna, S. N.; Bernel, S. *Phys. Rev. B* **1995**, *52*, R11650.
(80) Weber, S. E.; Jena, P. *Chem. Phys. Lett.* **1997**, *281*, 401.
(81) Ervin, K. M.; Ho, J.; Lineberger, W. C. *J. Chem. Phys.* **1993**, *99*, 8542.
(82) Reuse, F. A.; Khanna, S. N. *Eur. Phys. J* **1999**, *D6*, 77.
(83) Rubio, A.; Alonso, J. A.; Blase, X., Balbás, L. C.; Louie, S. G. *Phys. Rev. Lett.* **1995**, *75*, 2104.
(84) Ballone, P.; Jones, R. O. *Chem. Phys. Lett.* **1995**, *233*, 632.
(85) Chen, J. L.; Wang, C. S.; Jackson, K. A.; Pedersen, M. R. *Phys. Rev. B* **1991**, *44*, 6558.
(86) Castro, M.; Salahub, D. R. *Phys. Rev. B* **1994**, *49*, 11842.
(87) Goodwin, L.; Salahub, D. R. *Phys. Rev. A* **1993**, *47*, R774.
(88) Andzelm, J.; Radzio, E.; Salahub, D. R. *J. Chem. Phys.* **1985**, *83*, 9.
(89) Perdew, J. P. *Phys. Rev. B* **1986**, *33*, 8822.
(90) Kietzmann, H.; Morenzin, J.; Bechtold, P. S.; Ganteför, G.; Eberhardt, W.; Yang, D. S.; Hackett, P. A.; Fournier, R.; Pang, T.; Chen, C. *Phys. Rev. Lett.* **1996**, *77*, 4528.
(91) Williams, A. R.; de Groot, R. A.; Sommers, C. B. *J. Chem. Phys.* **1975**, *63*, 628.
(92) Fournier, R.; Pang, T.; Chen, C. *Phys. Rev. B* **1998**, *57*, 3683.
(93) Zhao, J.; Chen, X.; Wang, G. *Phys. Lett. A* **1996**, *214*, 211.
(94) Kietzmann, H.; Morenzin, J.; Bechthold, P. S.; Ganteför, G.; Eberhardt, W. *J. Chem. Phys.* **1998**, *109*, 2275.
(95) Holmgren, L.; Andersson, M.; Rosen, A. *Surf. Sci. 1995, 331*−*333*, 231.
(96) Parr, R. G.; Pearson, R. G. *J. Am. Chem. Soc.* **1983**, *105*, 7512.
(97) Alonso, J. A.; Balbás, L. C. *Structure and Bonding*; Sen, K. D., Ed.; Springer-Verlag: Berlin, 1993; Vol. 80 (Chemical Hardness), p 229.
(98) Wu, H.; Desai, S. R.; Wang, L. S.; *Phys. Rev. Lett.* **1996**, *76*, 212.
(99) Hanson, D. M.; Stockbauer, R.; Madey, T. E. *Phys. Rev. B.* **1981**, *24*, 5513.
(100) Feibelmann, P. J.; Himpsel, F. J. *Phys. Rev. B.* **1980**, *21*, 1394.
(101) Lian, L.; Su, C. X.; Armentrout, P. B. *J. Chem. Phys.* **1992**, *97*, 4084.
(102) Wu, H.; Desai, S. R.; Wang, L. S. *Phys. Rev. Lett.* **1996**, *77*, 2436.
(103) Pervan, P.; Valla, T.; Milum, M. *Solid State Commun.* **1994**, *89*, 917.
(104) Iseda, M.; Nishio, T.; Han, S. Y.; Yoshida, H.; Terasaki, A.; Kondow, T. *J. Chem. Phys.* **1997**, *106*, 2182.
(105) Minemoto, S.; Terasaki, A.; Imoto, H.; Kondow, T. *J. Chem. Phys.* **1998**, *109*, 9737.
(106) Knickelbein, M. *J. Chem. Phys.* **1993**, *98*, 1856.
(107) Collings, B. A.; Athanassenas, K.; Lacombe, D.; Rayner, D. M.; Hackett, P. A. *J. Chem. Phys.* **1994**, *101*, 3506.
(108) Slater, J. C. *The Calculation of Molecular Orbitals*; Wiley: New York, 1979.
(109) te Velde, G.; Baerends, E. J. *J. Comput. Phys.* **1992**, *99*, 84.
(110) Efremov, Y. M.; Samoilova, A. M.; Gurvich, L. V. *Opt. Spectrosc.* **1974**, *36*, 381.
(111) Michalopoulos, D. L.; Geusic, M. E.; Hansen, S. G.; Powers, D. E.; Smalley, R. E. *J. Phys. Chem.* **1982**, *86*, 3914.
(112) Andersson L. *Chem. Phys. Lett.* **1995**, *237*, 212.
(113) Cheng, H.; Wang, L. S. *Phys. Rev. Lett.* **1996**, *77*, 51.
(114) Su, C. X.; Armentrout, P. B. *J. Chem. Phys.* **1993**, *99*, 6506.
(115) Wang, L. S.; Wu, H.; Cheng, H. *Phys. Rev. B* **1997**, *55*, 12884.
(116) Casey, S. M.; Leopold, D. G. *J. Phys. Chem.* **1993**, *97*, 816.
(117) Klebanoff, L. E.; Robey, S. W.; Liu, G.; Shirley, D. E. *Phys. Rev. B* **1984**, *30*, 1048.
(118) Klebanoff, L. E.; Victora, R. H.; Falicov, L. M; Shirley, D. A. *Phys. Rev. B* **1985**, *32*, 1997.
(119) Dachsel, H.; Harrison, R. J.; Nixon, D. A. *J. Phys. Chem. A* **1999**, *103*, 152.
(120) Roos, B. *Acc. Chem. Res.* **1999**, *32*, 137.
(121) Herring, C.; Nichols, M. H. *Rev. Mod. Phys.* **1949**, *21*, 185.
(122) Leisner, T.; Athanassenas, K.; Echt, O.; Kandler, D.; Kreisle, D.; Recknagel, E. *Z. Physik D* **1991**, *20*, 127.
(123) Amrein, A.; Simpson, R.; Hackett, P. *J. Chem. Phys.* **1991**, *94*, 4663.
(124) Leisner, T.; Athanassenas, K.; Kreisle, D.; Recknagel, E.; Echt, O. *J. Chem. Phys.* **1993**, *99*, 9670.
(125) Weidele, H.; Kreisle, D.; Recknagel, E.; Schulze Icking-Konert, G.; Handschuh, H.; Eberhardt, W. *Chem. Phys. Lett.* **1995**, *237*, 425.
(126) Reiners, T.; Haberland, H. *Phys. Rev. Lett.* **1996**, *77*, 2440.
(127) Weidele, H.; Kreisle, D.; Recknagel, E.; Kluge, M. J.; Lindiger, M.; Schweikhard, L.; Walther, C.; Ziegler, J. *J. Chem. Phys.* **1999**, *110*, 8754.
(128) Klots, C. E. *Chem. Phys. Lett.* **1991**, *186*, 173.
(129) Nieman, G. C.; Parks, E. K.; Richtsmeier, S. C.; Liu, K.; Pobo, G.; Riley, S. J. *High Temp. Sci.* **1986**, *22*, 115.
(130) Athanassenas, K.; Leisner, T.; Frenkel, U.; Kreisle, D. *Ber. Bunsen-Ges. Phys. Chem.* **1992**, *96*, 1192.
(131) May, B. D.; Cartier, S. F.; Castleman, A. W. *Chem. Phys. Lett.* **1995**, *242*, 265.
(132) Cartier, S. F.; May, B. D.; Castleman, J. *Chem. Phys.* **1996**, *104*, 3423.
(133) Pettersson, L. G. M.; Faxen, T. *Theor. Chim. Acta* **1993**, *85*, 345.
(134) Benichou, E.; Antoine, R.; Rayane, D.; Vezin, B.; Dalby, F. W.; Dugourd, Ph.; Broyer, M.; Ristori, C.; Chandezon, F.; Huber, B. A.; Rocco, J. C.; Blundell, S. A.; Guet, C. *Phys. Rev. A* **1999**, *59*, 1.
(135) First, P. N.; Stroscio, J. A.; Dragoset, R. A.; Pierce, D. T.; Celotta, R. J. *Phys. Rev. Lett.* **1989**, *63*, 1416.
(136) Wawro, A.; Kasuya, A.; Czajka, R.; Nishina, Y. *Surf. Rev. Lett.* **1996**, *3*, 979.
(137) Vinod, C. P.; Kulkarni, G. U.; Rao, C. N. R. *Chem. Phys. Lett.* **1998**, *289*, 329.
(138) Kubo, R.; Kawabata, A.; Kobayashi, S. *Annu. Rev. Mater. Sci.* **1984**, *14*, 49.
(139) Friedel, J. In *The Physics of Metals*; Ziman, J. M., Ed.; Cambridge University Press: Cambridge, 1969; p 340.
(140) Pastor, G.; Dorantes-Dávila, J.; Bennemann, K. H. *Chem. Phys. Lett.* **1988**, *148*, 459.
(141) Zhao, J.; Chen, X.; Wang, G. *Phys. Rev. B* **1994**, *50*, 15424.
(142) Aguilera-Granja, F.; Alonso, J. A.; Montejano-Carrizales, J. M. In *Current Problems in Condensed Matter*; Morán-López, J. L., Ed.; Plenum: New York, 1998; p 109.
(143) Wertheim, G. K. *Z. Phys. D* **1983**, *12*, 319.
(144) Parks, E. K.; Klots, T. D.; Riley, S. J. *J. Chem. Phys.* **1990**, *92*, 3813.
(145) Aguilera-Granja, F.; Bouarab, S.; Vega, A.; Alonso, J. A.; Montejano-Carrizales, J. M. *Solid State Commun.* **1997**, *104*, 635.
(146) Gupta, R. P. *Phys. Rev. B* **1981**, *23*, 6265.
(147) Echt, O.; Sattler, K.; Recknagel, E. *Phys. Rev. Lett.* **1981**, *47*, 1121.
(148) Harris, I. A.; Kidwell, R. S.; Northby, J. A. *Phys. Rev. Lett.* **1984**, *53*, 2390.
(149) Martin, T. P.; Bergmann, T.; Göhlich, H.; Lange, T. *Z. Phys. D* **1991**, *19*, 25.
(150) Martin, T. P.; Bergmann, T. *J. Chem. Phys.* **1989**, *90*, 6664.
(151) Rayane, D.; Melinon, P.; Cabaud, B.; Hoareau, A.; Tribollet, B.; Broyer, M. *Phys. Rev. A* **1989**, *39*, 6059.
(152) Martin, T. P.; Bergmann, T.; Göhlich, H.; Lange, T. *Chem. Phys. Lett.* **1991**, *176*, 343.
(153) Pellarin, M.; Baguenard, B.; Vialle, J. L.; Lermé, J.; Broyer, M.; Miller, J.; Perez, A. *Chem. Phys. Lett.* **1994**, *217*, 349.
(154) Martin, T. P. *Phys. Rep.* **1996**, *273*, 199.
(155) Klots, T. D.; Winter, B. J.; Parks, E. K.; Riley, S. J. *J. Chem. Phys.* **1990**, *92*, 2110.
(156) Klots, T. D.; Winter, B. J.; Parks, E. K.; Riley, S. J. *J. Chem. Phys.* **1991**, *95*, 8919.
(157) Parks, E. K.; Riley, S. J. *Z. Phys. D* **1995**, *33*, 55.
(158) Parks, E. K.; Winter, B. J.; Klots, T. D.; Riley, S. J. *J. Chem. Phys.* **1992**, *96*, 8267.
(159) Parks, E. K.; Zhu, L.; Ho, J.; Riley, S. J. *J. Chem. Phys.* **1994**, *100*, 7206.
(160) Montejano-Carrizales, J. M.; Iñiguez, M. P.; Alonso, J. A.; López, M. J. *Phys. Rev. B* **1996**, *54*, 5961.
(161) Sung, M. W.; Kawai, R.; Weare, J. H. *Phys. Rev. Lett.* **1994**, *73*, 3552.
(162) Foiles, S. M., Baskes, M. I.; Daw, M. S. *Phys. Rev. B* **1986**, *53*, 7983.
(163) Daw, M. S.; Baskes, M. I. *Phys. Rev. B* **1984**, *29*, 6443.
(164) Rose, J. H.; Smith, J. R.; Guinea, F.; Ferrante, J. *Phys. Rev. B* **1985**, *29*, 2963.
(165) Cleveland, C. L.; Landman, U. *J. Chem. Phys.* **1991**, *94*, 7376.
(166) Rey, C.; Gallego, L. J.; García-Rodeja, J.; Alonso, J. A.; Iñiguez, M. P. *Phys. Rev. B* **1993**, *48*, 8253.
(167) Montejano-Carrizales, J. M.; Iñiguez, M. P.; Alonso, J. A. *J. Cluster Sci.* **1994**, *5*, 287.
(168) García-Rodeja, J.; Rey, C.; Gallego, L. J.; Alonso, J. A. *Phys. Rev. B* **1994**, *49*, 8495 1994.
(169) Garzón, I. L.; Jellinek, J. In *Physics and Chemistry of Finite Systems: From Clusters to Crystals*; Jena, P., Khanna, S. N., Rao, B. K., Eds.; Kluwer: Dordrecht, 1992; Vol. I, p 405.
(170) Güvenc, Z. B.; Jellinek, J.; Voter, A. F. In *Physics and Chemistry of Finite Systems: From Clusters to Crystals*; Jena, P., Khanna, S. N., Rao, B. K., Eds.; Kluwer: Dordrecht, 1992; Vol. I, p 411.
(171) Stave, M. S.; De Pristo, A. E. *J. Chem. Phys.* **1992**, *97*, 3386.
(172) Parks, E. K.; Kerns, K. P.; Riley, S. J. *J. Chem. Phys.* **1998**, *109*, 10207.
(173) Wetzel, T. L.; De Pristo, A. E. *J. Chem. Phys.* **1996**, *105*, 573.
(174) Parks, E. K.; Winter, B. J.; Klots, T. D.; Riley, S. J. *J. Chem. Phys.* **1991**, *94*, 1882.

(175) Stave, M. S.; Sanders, D. E.; Raeker, T. J.; De Pristo, A. E. *J. Chem. Phys.* **1990**, *93*, 4413.
(176) Vajda, S.; Wolf, S.; Leisner, T.; Busolt, U.; Wöste, L. H.; Wales, D. J. *J. Chem. Phys.* **1997**, *107*, 3492.
(177) Mingos, D. M. P. *Adv. Chem. Res.* **1984**, *17*, 311.
(178) Jellinek, J.; Güvenc, Z. B. In *The Synergy between Dynamics and Reactivity at Clusters and Surfaces*; Farrugia, L. J., Ed.; Kluwer: Dordrecht, 1995; p 217.
(179) Rey, C.; García-Rodeja, J.; Gallego, L. J. *Phys. Rev. B* **1996**, *54*, 2942.
(180) Vlachos, D. G.; Schmidt, L. D.; Aris, R. *Z. Phys. D* **1993**, *26*, S156.
(181) Lathiotakis, N. N.; Andriotis, A. N.; Menon, M.; Connolly, J. *Europhys. Lett.* **1995**, *29*, 135.
(182) Lathiotakis, N. N.; Andriotis, A. N.; Menon, M.; Connolly, J. *J. Chem. Phys.* **1996**, *104*, 992.
(183) Doye, J. P. K.; Wales, D. J. *New J. Chem.* **1998**, *22*, 733.
(184) Sutton, A. P.; Chen, J. *Philos. Mag. Lett.* **1990**, *61*, 139.
(185) Billas, I. M. L.; Chatelain, A.; de Heer, W. A. *Science* **1994**, *265*, 1682.
(186) Billas, I. M. L.; Chatelain, A.; de Heer, W. A. *J. Magn. Magn. Mater.* **1997**, *168*, 64.
(187) Cox, D. M.; Trevor, D. J.; Whetten, R. L.; Rohlfing, E. A.; Kaldor, A. *Phys. Rev. B* **1985**, *32*, 7290.
(188) de Heer, W. A.; Milani, P.; Chatelain, A. *Phys. Rev. Lett.* **1990**, *65*, 488.
(189) Bucher, J. P.; Douglass, D. C.; Bloomfield, L. A. *Phys. Rev. Lett.* **1991**, *66*, 3052.
(190) Douglass, D. C.; Cox, A.; Bucher, J. P.; Bloomfield, L. A. *Phys. Rev. B* **1993**, *47*, 12874.
(191) Billas, I. M. L.; Becker, J. A.; Chatelain, A.; de Heer, W. A. *Phys. Rev. Lett.* **1993**, *71*, 4067.
(192) Khanna, S. N.; Linderoth, S. *Phys. Rev. Lett.* **1991**, *67*, 742.
(193) Dattagupta, S.; Mahanti, S. D. *Phys. Rev. B* **1998**, *57*, 10244.
(194) Gantefor, G.; Eberhardt, W. *Phys. Rev. Lett.* **1996**, *76*, 4975.
(195) Handshuh, H.; Cha, C. Y.; Bechtold, P. S.; Gantefor, G.; Eberhardt, W. *J. Chem. Phys.* **1995**, *102*, 6404.
(196) Cox, A. J.; Lourderback, J. G.; Bloomfield, L. A. *Phys. Rev. Lett.* **1993**, *71*, 923. Cox, A. J.; Lourderback, J. G.; Apsel, S. E.; Bloomfield, L. A. *Phys. Rev. B* **1994**, *49*, 12295.
(197) Zhao, J.; Chen, X.; Sun, Q.; Liu, F.; Wang, G. *Phys. Lett. A* **1995**, *205*, 308.
(198) Aguilera-Granja, F.; Montejano-Carrizales, J. M.; Morán-López, J. L. *Solid State Commun.* **1998**, *107*, 25.
(199) Jensen, P.; Bennemann, K. H. *Z. Phys. D* **1995**, *35*, 273.
(200) Clogston, A. M.; Matthias, B. T.; Peter, M.; Williams, H. J.; Corenzwit, E.; Sherwood, R. C. *Phys. Rev.* **1962**, *125*, 541; Freeman, A. J.; Fu, R. *J. Magn. Magn. Mater.* **1991**, *100*, 497.
(201) Aguilera-Granja, F.; Montejano-Carrizales, J. M.; Morán-López, J. L. *Phys. Lett. A* **1998**, *242*, 255.
(202) Binder, K.; Rauch, H.; Wildpaner, V. *J. Phys. Chem. Solids* **1970**, *31*, 391.
(203) Brown, P. J.; Capellmann, H.; Déportes, J.; Givord, D.; Ziebeck, K. R. A. *J. Magn. Magn. Mater.* **1983**, *31*−*34*, 305.
(204) Mook, H. A. *J. Magn. Magn. Mater.* **1983**, *31*−*34*, 305.
(205) Pastor, G. M.;Dorantes-Dávila, J. *Phys. Rev. B* **1995**, *52*, 13799.
(206) Hirt, A.; Gerion, D.; Billas, I. M. L.; Châtelain, A.; de Heer, W. A. *Z. Phys. D* **1997**, *40*, 160.
(207) Stoner, E. C. *Magnetism of Matter*; Methuer and Co.: London, 1934.
(208) Goringe, C. M.; Bowler, D. R.; Hernández, E. *Rep. Prog. Phys.* **1997**, *60*, 1447.
(209) Vega, A.; Dorantes-Dávila, J.; Balbás, L. C.; Pastor, G. M. *Phys. Rev. B* **1993**, *47*, 4742.
(210) Fabricius, G.; Llois, A. M.; Weissmann, M. *Phys. Rev. B* **1991**, *44*, 6870.
(211) Fabricius, G.; Llois, A. M.; Weissmann, M.; Khan, M. A. *Phys. Rev. B* **1994**, *49*, 2121.
(212) Heine, V. *Phys. Rev.* **1967**, *153*, 673.
(213) Pastor, G. M.; Dorantes-Dávila, J.; Bennemann, K. H. *Physica B* **1988**, *149*, 22; *Phys. Rev. B* **1989**, *40*, 7642.
(214) Bandyopahyay, T.; Sarma, D. D. *Phys. Rev. B* **1989**, *39*, 35177.
(215) Guevara, J.; Parisi, F.; Llois, A. M.; Weissmann, M. *Phys. Rev. B* **1997**, *55*, 13283.
(216) Haydock, R. *Solid State Phys.* **1980**, *35*, 215.
(217) Dorantes-Dávila, J.; Dreyssé, H.; Pastor, G. M. *Phys. Rev. B* **1992**, *46*, 10432.
(218) Bouarab, S.; Vega, A.; López, M. J.; Iñiguez, M. P.; Alonso, J. A. *Phys. Rev. B* **1997**, *55*, 13279.
(219) Aguilera-Granja, F.; Bouarab, S.; López, M. J.; Vega, A.; Montejano-Carrizales, J. M.; Iñiguez, M. P.; Alonso, J. A. *Phys. Rev. B* **1998**, *57*, 12469.
(220) Vega, A.; Demangeat, C.; Dreyssé, H.; Chouairi, A. *Phys. Rev. B* **1995**, *51*, 11546.
(221) Ducastelle, F. *J. Phys. (Paris)* **1970**, *31*, 1055.
(222) López, M. J.; Jellinek, J. *Phys. Rev. A* **1994**, *50*, 1445.
(223) Parks,, E. K.; Nieman, G. C.; Kerns, K. P.; Riley, S. J. *J. Chem. Phys.* **1997**, *107*, 1861.
(224) Rodríguez-López, J. L.; Aguilera-Granja, F.; Vega, A.; Alonso, J. A. *Eur. Phys. J. D* **1999**, *6*, 235.
(225) Nayak, S. K.; Khanna, S. N.; Rao, B. K.; Jena, P. *J. Phys. Chem. A* **1997**, *101*, 1072.
(226) Hu, W.; Mei, L. M.; Li, H. *Solid State Commun.* **1996**, *100*, 129.
(227) Andriotis, A. N.; Lathiotakis, N. N.; Menon, M. *Europhys. Lett.* **1996**, *36*, 37.
(228) Andriotis, A. N.; Menon, M. *Phys. Rev. B* **1998**, *57*, 10069.
(229) Menon, M.; Connolly, J.; Lathiotakis, N.; Andriotis, A. N. *Phys. Rev. B* **1994**, *50*, 8903.
(230) Tomanek, D.; Schluter, M. A. *Phys. Rev. B* **1987**, *36*, 1208.
(231) Basch, H.; Newton, M. D.; Moskowitz, J. W. *J. Chem. Phys.* **1980**, *73*, 4492.
(232) Mlynarski, P.; Salahub, D. R. *J. Chem. Phys.* **1991**, *73*, 4492.
(233) Yu, Z.; Almlof, J. *J. Phys. Chem.* **1991**, *95*, 9167.
(234) Pastor, G.; Hirsch, R.; Muhlschlegel, B. *Phys. Rev. B* **1996**, *53*, 10382.
(235) Fujima, N.; Yamaguchi, T. *Phys. Rev. B* **1996**, *54*, 26.
(236) Fujima, N.; Yamaguchi, T. *J. Phys. Soc. Jpn.* **1989**, *58*, 3290.
(237) Pacchioni, G.; Chung, S. C.; Krüger, S.; Rösch, N. *Chem. Phys.* **1994**, *184*, 125.
(238) Fujima, N.; Yamaguchi, T. *Mater. Sci. Eng. A* **1996**, *217*, 295.
(239) Lee, K.; Callaway, J.; Dhar, S. *Phys. Rev. B* **1984**, *30*, 1724. Lee, K.; Callaway, J.; Kwong, K.; Tang, R.; Ziegler, A. *Phys. Rev. B* **1985**, *31*, 1796.
(240) Douglass, D. C.; Bucher, J. P.; Bloomfield, L. A. *Phys. Rev. B* **1992**, *45*, 6341.
(241) Blügel, S.; Drittler, B.; Zeller, R.; Dederichs, P. H. *Appl. Phys. A* **1989**, *49*, 547.
(242) Stepanyuk, V. S.; Hergert, W.; Wildberger, K.; Nayak, S. K.; Jena, P. *Surf. Sci. Lett.* **1997**, *384*, L892.
(243) Baumann, C. A.; Van Zee, R. J.; Bhat, S.; Weltner, W. *J. Chem. Phys.* **1983**, *78*, 190.
(244) Morse, M. D. *Chem. Rev.* **1986**, *86*, 1049.
(245) Parks, E. K.; Nieman, G. C.; Riley, S. J. *J. Chem. Phys.* **1996**, *104*, 3531.
(246) Koretsky, G. M.; Knickelbein, M. B. *J. Chem. Phys.* **1997**, *106*, 9810.
(247) Van Zee, R. J.; Weltner, W. *J. Chem. Phys.* **1988**, *89*, 4444.
(248) Ludwig, G. W.; Woodbury, H. H.; Carlson, R. O. *J. Phys. Chem. Solids* **1959**, *8*, 490.
(249) Nesbet, R. K. *Phys. Rev.* **1964**, *135*, A460.
(250) Van Zee, R. J.; Baumann, C. A.; Weltner, W. *J. Chem. Phys.* **1981**, *74*, 6977.
(251) Rivoal, J. C.; Emampour, J. H.; Zeringe, K. J.; Vala, M. *Chem. Phys. Lett.* **1982**, *92*, 313.
(252) Fujima, N.; Yamaguchi, T. *J. Phys. Soc. Jpn.* **1995**, *64*, 1251.
(253) Nayak, S. K.; Jena, P. *Chem. Phys. Lett.* **1998**, *289*, 473.
(254) Becke, A. D. *J. Chem. Phys.* **1993**, *98*, 5648.
(255) Lee, C.; Yang, W.; Parr, R. G. *Phys. Rev. B* **1988**, *37*, 785.
(256) Schieffer, P.; Krembel, C.; Hanf, M. C.; Bolmont, D.; Gewinner, G. *J. Magn. Magn. Mater.* **1997**, *165*, 180
(257) Rader, O.; Gudat, W. *Phys. Rev. B* **1997**, *56*, 5053.
(258) Pederson, M. R.; Reuse, F.; Khanna, S. N. *Phys. Rev. B* **1998**, *58*, 5632.
(259) Perdew, J. P.; Burke, K.; Ernzerhof, M. *Phys. Rev. Lett.* **1996**, *77*, 3865.
(260) van Steveren, M. P. J.; Brom, H. B.; de Jongh, L. J. *Phys. Rep.* **1999**, *208*, 1.
(261) van Leeuwen, D. A.; van Ruitenbeek, J. M.; de Jongh, L. J.; Ceriotti, A.; Pacchioni, G.; Häberlen, O. D.; Rösch, N. *Phys. Rev. Lett.* **1994**, *73*, 1432.
(262) Chen, B.; Castleman, A. W.; Khanna, S. N. *Chem. Phys. Lett.* **1999**, *304*, 423.
(263) Galicia, R. *Rev. Mex. Fis.* **1985**, *32*, 51.
(264) Reddy, B. V.; Khanna, S. N.; Dunlap, B. *Phys. Rev. Lett.* **1993**, *70*, 3323.
(265) Piveteau, B.; Desjonquéres, M. C.; Olés, A. M.; Spanjard, D. *Phys. Rev. B* **1996**, *53*, 9251.
(266) Jinlong, Y.; Toigo, F.; Kelin, W.; Manhong, Z. *Phys. Rev. B* **1994**, *50*, 7173.
(267) Jinlong, Y.; Toigo, F.; Klein, W.; Manhong, Z. *Phys. Rev. B* **1994**, *50*, 7915.
(268) Li, Z. Q.; Yu, J. Z.; Ohno, K.; Kawazoe, Y. *J. Phys.: Condens. Matter* **1995**, *7*, 47.
(269) Pastor, G.; Hirsch, R.; Mühlschlegel, B. *Phys. Rev. Lett.* **1994**, *53*, 72.
(270) Villaseñor-González, P.; Dorantes-Dávila, J.; Dreyssé, H.; Pastor, G. *Phys. Rev. B* **1997**, *55*, 15084.
(271) Chouairi, A.; Dreyssé, H.; Nait-Laziz, H.; Demangeat, C. *Phys. Rev. B* **1993**, *48*, 7735. Mokrani, A.; Dreyssé, H. *Solid State Commun.* **1994**, *90*, 31.
(272) Guirado-López, R.; Spanjaard, D.; Desjonquéres, M. C. *Phys. Rev. B* **1998**, *57*, 6305.
(273) Nayak, S. K.; Weber, S. E.; Jena, P.; Wildberger, K.; Zeller, R.; Dederichs, P. H.; Stepanyuk, V. S.; Hergert, W. *Phys. Rev. B* **1997**, *56*, 8849.
(274) Geusic, M. E.; Morse, M. D.; Smalley, R. E. *J. Chem. Phys.* **1985**, *82*, 590.

(275) Guirado-López, R.; Spanjaard, D.; Desjonquéres, M. S.; Aguilera-Granja, F. *J. Magn. Magn. Mater.* **1998**, *186*, 214.
(276) Kaiming, D.; Jinlong, Y.; Chuamyun, X.; Kelin, W. *Phys. Rev. B* **1996**, *54*, 2191.
(277) Lee, K. *Phys. Rev. B* **1998**, *58*, 2391.
(278) Lee, K. *Z. Phys. D* **1977**, *164*.
(279) Tsunoda, Y. *J. Phys. Condens. Matter* **1988**, *1*, 10427.
(280) Mryasov, O. N.; Liechtenstein, A. I.; Sandratskii, L. M.; Gubanov, V. A. *J. Phys. Condens. Matter* **1991**, *3*, 7683.
(281) Lorenz, R.; Hafner, J.; Jaswal, S. S.; Sellmyer, D. J. *Phys. Rev. Lett.* **1995**, *74*, 3688.
(282) Liebs, M.; Hummler, K.; Fähnle, M. *Phys. Rev. B* **1995**, *51*, 8664.
(283) Sandratskii, L. M.; Gulekskii, P. G. *J. Magn. Magn. Matter.* **1989**, *79*, 306.
(284) Antropov, V. P.; Katsnelson, M. I.; van Schilfgaarde, M.; Harmon, B. N. *Phys. Rev. Lett.* **1995**, *75*, 29.
(285) Uhl, M.; Kübler, J. *Phys. Rev. Lett.* **1996**, *77*, 334.
(286) Sandratskii, L. M.; Kübler, J. *Phys. Rev. Lett.* **1996**, *76*, 4963.
(287) Oda, T.; Pasquarello, A.; Car, R. *Phys. Rev. Lett.* **1998**, *80*, 3622.
(288) van Barth, U.; Hedin, L. *J. Phys. C* **1972**, *5*, 1629.
(289) Kübler, J.; Höck, K.; Sticht, J.; Williams, A. R. *J. Phys. F* **1988**, *18*, 469.
(290) Vanderbilt, D. *Phys. Rev. B* **1990**, *41*, 7892.
(291) Corso, A. D.; Pasquarello, A.; Baldereschi, A. *Phys. Rev. B* **1997**, *56*, R 11369.

CR980391O